University of Washington

2014

Department of Bioengineering

University of Washington

Graduate School

This is to certify that I have examined this copy of a doctoral dissertation by

Jonathan Cheng

and have found that it is complete and satisfactory in all respects,

and that any and all revisions required by the final

examination committee have been made.

Supervisory Committee:

_____	_____
Albert Folch (chair)	Deok-Ho Kim
_____	_____
Marvin Adams (GSR)	Michael Regnier
_____	_____
Stephen Hauschka	Nathan Sniadecki

Date:

_____

Microfluidic Platforms for Focal Stimulation of Muscle Cells and Large-scale Studies of Synaptogenesis

by

Jonathan Cheng

A doctoral dissertation

submitted in partial fulfillment of the

requirements for the degree of

Doctor of Philosophy

The University of Washington

2014

ACKNOWLEDGEMENTS

Support for this work was generously provided by the National Institutes of Health / National Institute of Biomedical Imaging and Bioengineering (Grant #R01 EB007526-01).

I would like to express my sincere gratitude to my advisor, Dr. Albert Folch for his guidance and support throughout my graduate career. I would like to thank my supervisory committee members: Dr. Marv Adams for encouraging and engaging discussions on NMJ biology, Dr. Stephen Hauschka for discussions on muscle biology and advice on cell culture, Dr. Deok-Ho Kim for discussions on muscle biology, Dr. Michael Regnier for help on defining a clear hypothesis, and Dr. Nathan Sniadecki for discussions on microfabrication and image processing. I would like to thank Dr. Nirveek Bhattacharjee for his patient mentorship and guidance. Also, I would like to acknowledge my labmates, past and present: Dr. Christopher Sip, Dr. Tim Chang, Dr. Anthony Au, and Dr. Lisa Folch, for their camaraderie and support. Finally, I would like to thank my undergraduate students, Philip Lindstedt and Ross Boitano for their time and dedication in helping with my research efforts.

Outside of the lab, my parents, Jackie Du and Peiwen Cheng, and extended family have always been there for me. I want to thank them. I would like to express my fondest gratitude to my girlfriend, Vega Shah, who has come into my life and kindly supported me in the final years of my graduate career. Finally, I would like to thank my friends in Seattle, a city that I have grown to call my home.

The University of Washington

Microfluidic Platforms for Focal Stimulation of Muscle Cells and Large-scale Studies of Synaptogenesis

Jonathan Cheng, Ph.D.
2014
Chair of the Supervisory Committee:
Albert Folch, Associate Professor, Department of Bioengineering

A central question in neurobiology is how the neuromuscular junction (NMJ) forms and maintains its high density of acetylcholine receptors (AChRs) in development. Although many of the molecules involved in NMJ synaptogenesis have been identified, the exact mechanisms by which the synaptogenic protein agrin induces and stabilizes AChR clusters remains unclear. While most *in vitro* experiments lack microscale control, microfluidics offers a high degree of control of the NMJ fluidic and substrate microenvironment. In this dissertation, we developed a model in which we effectively substituted the motor neuron with locally applied microfluidic agrin stimuli to subcellular regions of micropatterned myotubes. We explored two strategies for generating focal delivery: 1) a laminar flow-based hydrodynamic focusing device that operates in an open chamber, and 2) a modified Transwell that operates based on area-selective diffusion of soluble species to the basal side of myotubes. We further developed cell micropatterning methods coupled with the device designs that created well-defined arrays of muscle cultures, enabling automated microscopy and image processing protocols. Finally, we demonstrated, using the Transwell system, that focal agrin application: 1) induced localized AChR microclustering, and 2) had no effect on the stability of laminin-induced AChR pretzel clusters. Together, we present a suite of precise, user-friendly microscale tools that provide spatiotemporal control for the presentation of neuronal factors in NMJ synaptogenesis, and potentially for applications in single cell analysis and tissue engineering.

TABLE OF CONTENTS

LIST OF FIGURES

LIST OF TABLES

CHAPTER 1: INTRODUCTION

1.1 SIGNIFICANCE OF SYNAPSE BIOLOGY

A major goal in neuroscience is to understand the formation and development of synapses, the small membrane specializations that mediate communication between neurons and their target cells: other neurons, muscle cells, or gland cells [1]. The human brain is an amazingly complex organ consisting of hundreds of billions of neurons and up to quadrillions (~10^{15}) of synapses [2]. Every idea, emotion, and physical movement is carried out as a series of electrical and chemical signals conducted through a network of neurons and their target cells through synapses. Synapse development occurs starting in the embryo and extends well past postnatal stages into adulthood, where it contributes to learning and memory. Diseases related to synapse formation, or synaptogenesis, and its developmental pathways include autism, Down's syndrome, Alzheimer's disease, and schizophrenia. For example, large-scale genetic screening studies found mutations in the synaptic protein SHANK3, a scaffolding protein linking neurotransmitter receptors to the actin cytoskeleton, in autism and schizophrenia patients [3]. There are also diseases that affect the nerve-muscle synapses, the neuromuscular junctions, which result in symptoms such as muscle weakness and fatigability. These are divided in two classes: 1) congenital myasthenia, caused by mutations in agrin or acetylcholine, which are major players in synaptogenesis, and 2) myasthenia gravis, an autoimmune disorder in which the body's own antibodies block the acetylcholine receptors [4]. Therefore, understanding synaptogenic pathways is important in not only uncovering etiologies of neurological disorders, but to an overall understanding of neurobiology.

1.2 SYNAPSE BIOLOGY BACKGROUND

1.2.1 Synapse function and synaptogenesis

Synapses are asymmetric cellular junctions characterized by specialized zones on the presynaptic neuron and the postsynaptic cell, separated by a nanometer-scale synaptic cleft [1, 5]. Communication in synapses is carried out when a depolarizing action potential causes synaptic vesicles to fuse with the plasma membrane and to release neurotransmitters into the synaptic cleft. The neurotransmitters then diffuse across the synaptic cleft and bind with its receptors on the postsynaptic cell. The concentrated clustering of neurotransmitter receptors and signaling proteins at the postsynaptic cell is called the postsynaptic density. The process of synaptogenesis involves the differentiation of neurons and their target cells, the navigation of axons over long distances to their targets, and the induction of pre- and post-synaptic specializations [6]. Finally, synaptic activity itself determines whether these synapses will be retained or eliminated. These highly coordinated developmental events require spatiotemporally precise cell signaling.

1.2.2 The neuromuscular junction

Synaptogenesis has been most well studied in the neuromuscular junction (NMJ), the connection between motor neurons and skeletal muscle. Due to its relatively large size, simplicity, and accessibility, *in vivo* and *in vitro* experiments have largely elucidated the molecular players in NMJ synaptogenesis. Thus, the NMJ provides a model for understanding synaptogenesis in the central nervous system, which is much more complex and less accessible.

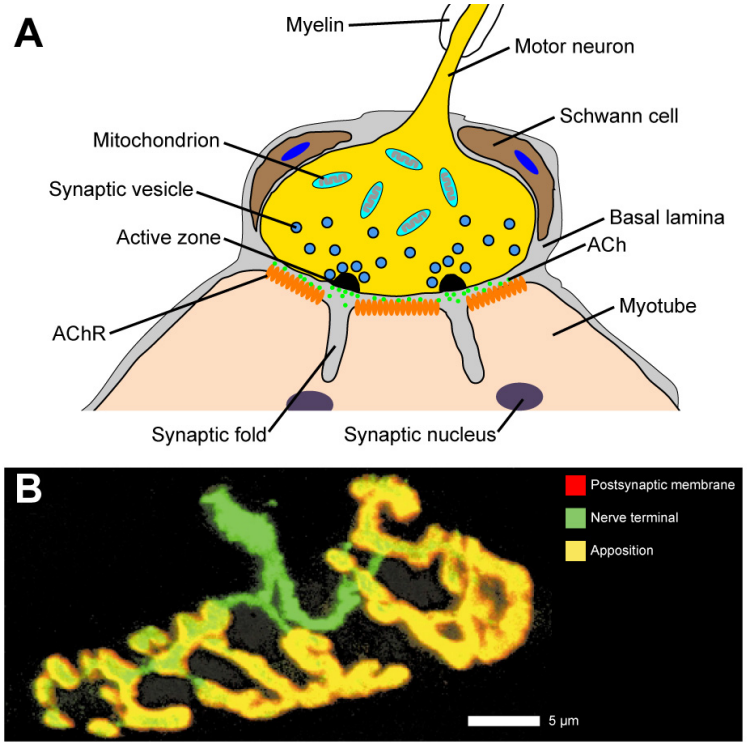

Figure 1.1: Overview of the neuromuscular junction.

(A) A schematic of the neuromuscular junction showing the major cells: the motor neuron, the muscle fiber (myotube), and the Schwann cell in close apposition. Synaptic vesicles containing neurotransmitters (ACh) are released from a specialized region on the neuron called the active zone into the synaptic cleft where they encounter a region of clustered AChRs on the muscle fiber. (B) *In vivo* image of the NMJ of an adult mouse showing the motor axon (green) and its apposition with AChRs (yellow and red) on the postsynaptic membrane of the myotube. Figure 1.1B adapted from [7].

The NMJ is a highly specialized, topologically complex structure with a high concentration of synapse-specific organelles and molecules on both the presynaptic motor neuron and postsynaptic muscle fiber (Figure 1.1). In addition, Schwann cells cap and support the nerve terminal. The development of this highly organized structure involves a complex series of developmental events [8]. In the initial stages of NMJ development, myoblasts migrate to a muscle site and fuse into multi-nucleated myotubes, whereby genes encoding for contractile and synaptic proteins are also expressed. Meanwhile,

motor axons emanate from the central nervous system and run long distances through peripheral nerves to encounter muscles. Motor axons innervate only a single muscle, but may form branches to innervate several muscle fibers. The group of cells including the single motor neuron and all the muscle fibers that it innervates is defined as a motor unit. Synaptic transmission commences once a motor axon growth cone comes into contact with a myotube, albeit initially at a low level of efficiency. Over a week, the pre- and post- synaptic regions of the neuron and muscle specialize to form a functional, highly efficient NMJ.

1.2.3 Molecular signaling in NMJ synaptogenesis: agrin and acetylcholine

The hallmark of the mature NMJ is the high surface concentration of acetylcholine receptors (AChRs) on the postsynaptic terminal, which allows fast and efficient communication via the diffusion of the neurotransmitter acetylcholine (ACh), between the motor neuron and muscle fiber [7]. The embryonic development of the NMJ synapse is a spatiotemporally dynamic event in which initially diffuse acetylcholine receptors (AChRs) (~1000 molecules per μm^2) on the muscle membrane organize into intricate, topologically complex AChR "pretzel"-like patterns. The differences in AChR density is remarkable: ~10,000 molecules per μm^2 within the synapse, but falls to ~10 molecules per μm^2 only micrometers away outside the synapse. A given synapse covers less than 0.1% of the muscle fiber surface, so the aggregation of AChRs is highly spatially specific [9]. The maintenance of this high synaptic AChR concentration is regulated by three mechanisms: 1) localized clustering of initially diffuse AChRs, 2) subsynaptic nuclei upregulation of AChR gene expression within the synapse, and 3) extrasynaptic nuclei suppression of AChR gene expression outside of the synapse (Figure 1.2). AChRs are highly dynamic: constantly being degraded, internalized, recycled, and

re-inserted back into the plasma membrane [7]. The rate of AChR turnover is much faster in developing embryonic NMJs (half-life ~17-24 hours) than in adult NMJs (half-life ~8-14 days). In comparison, AChR "pretzel" clusters in C2C12 myotube culture systems that resemble the *in vivo* NMJ are even shorter lived (half-life ~4.5 hours) [10].

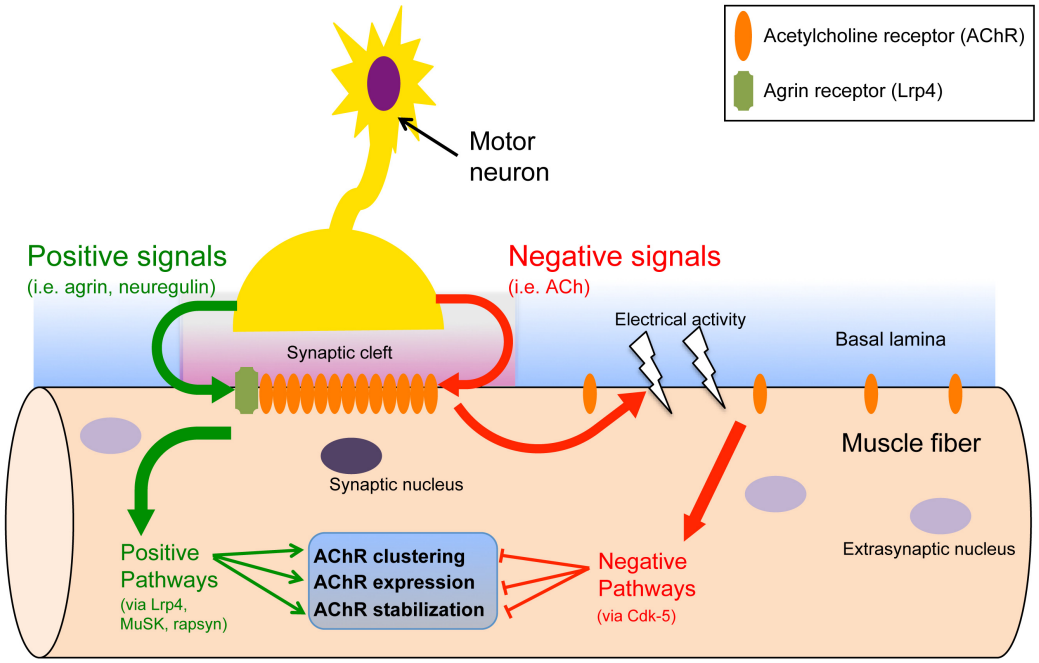

Figure 1.2: Molecular signaling in NMJ formation.

NMJ synaptogenesis occurs through coordinated positive signals and negative neuronal signals directed at the muscle. The positive signals, agrin and neuregulin, promote intracellular signaling pathways that induce localized AChR clustering, AChR gene expression by the subsynaptic nuclei, and AChR stabilization. The negative signals, notably acetylcholine, cause electrical activity (i.e. propagation of action potentials down the myotube length), which abolishes AChR clustering in extrasynaptic regions. Agrin binding to its receptor, Lrp4, causes the dimerization of the kinase, MuSK, which in turn affects pathways involved in AChR trafficking, insertion, and immobilization in association with the actin. The agrin pathway also affects rapsyn, which helps anchor AChRs to the actin cytoskeleton.

Proteins on both the motor neuron side and the muscle fiber side play key roles in organizing high AChR density in the synapse [11]. The critical molecules released by the motor neuron are thought to be agrin, a heparan sulfate proteoglycan of ~400 kDa from

the basal lamina, and neuregulin, an EGF family protein. We will refer to these pro-aggregating factors as "positive factors." Neuronal z-agrin, an alternatively spliced isoform, is 1000 times more potent in clustering AChRs than muscle-derived agrin [12]. The word "agrin" originates from the Greek word *agrein* – to assemble. Many of the postsynaptic components – agrin, MuSK, rapsyn, and AChRs – were initially isolated in the hypertrophied NMJ of the electric organ of the Pacific electric ray, *Torpedo californica* [7]. Agrin was initially found to induce clustering of AChRs along with other postsynaptic proteins in cultured myotubes [13], which led to the "agrin hypothesis," that stated that agrin is the main nerve-derived organizer of NMJ synaptogenesis. Subsequent gain-of-function and loss-of-function studies with agrin supported this theory. Specifically, injection of agrin-encoding cDNA into extrasynaptic regions of denervated soleus muscles caused ectopic formation of AChR clusters, showing agrin's function as a synaptic inducer [14, 15]. Agrin knockout mice showed severely impaired AChR clustering, resulting in paralyzed animals with reduced numbers, densities, and sizes of AChR aggregates that were mostly unconnected to axons. In these cases, AChR clusters did form in the endplate zone at E14.5, but failed to stabilize under the motor neuron innervation [16].

Agrin acts through its receptor, Lrp4, and the muscle receptor tyrosine kinase, MuSK [5]. Interestingly, myotubes without MuSK were unresponsive to agrin [17]. MuSK affects intracellular signaling molecules downstream such as GTPases, which affect actin dynamics, and are thought to drive the movement of AChRs [11]. Another key protein, rapsyn, was identified through knockout studies as also being essential to synaptogenesis [18]. Rapsyn functions in tethering AChRs in a protein complex to the actin cytoskeleton [19].

In addition to the agrin positive factor, neuregulin, a trophic factor secreted by the motor neuron into the synaptic cleft, is known to upregulate AChR gene expression in subsynaptic nuclei [7, 20]. Neuregulin signals by binding to a receptor tyrosine kinase, ErbB, which is thought to act in parallel with the agrin-MuSK pathway. However, the role of neuregulin is not as clear, as it may act on both muscle and Schwann cells. As shown in mutant mice lacking neuregulin, ErbB signaling is crucial for Schwann cell proliferation and survival, which in turn, provide axon guidance and trophic support for neurons. Due to the confounding nature of neuregulin signaling, which may act on multiple cell types, we focused on agrin as the positive AChR clustering factor in our experiments.

The agrin hypothesis supported a one-sided "neurocentric view," in which synaptogenesis occurs due to the motor neuron releasing pro-aggregating factors, agrin and neuregulin, which recruit postsynaptic proteins, and lead to the formation and clustering of AChRs. The neurocentric agrin hypothesis was challenged in the early 2000s when it was discovered that mice lacking motor neurons showed AChR clustering. Developmentally before the motor axon tip even encounters the muscle fiber, there are already "protosynapse" or "prepatterned" AChR clusters [16, 21, 22]. Moreover, mature, elaborate AChR clusters (pretzels) were found *in vitro* on cultured myotubes, independent of motor neuron signaling [23]. Together, these findings suggested agrin to have a stabilizing rather than (or perhaps in addition to) an inducing role in NMJ synaptogenesis.

In addition to the positive factors, agrin and neuregulin, which promote AChR clustering, there are "negative factors" that disperse AChRs in extrasynaptic zones, and help spatially define the synapse [24, 25]. Surprisingly, the neurotransmitter itself,

acetylcholine, is thought to be the primary negative factor. In mutant mice with knockouts of both choline acetyltransferase (ChAT), the enzyme that synthesizes acetylcholine, and of agrin, AChR clusters were surprisingly numerous. In contrast, in mice that only had an agrin knockout alone, AChR clusters were not formed, suggesting that ACh is a declustering factor. In other words, in the presence of ACh alone (in agrin knockouts), AChRs were declustered, while in the absence of both ACh and agrin (in double knockouts), AChRs were maintained. These findings added to the reinterpretation of agrin as an "anti-declustering factor" that counteracts the declustering effect of ACh.

Although many *in vivo* studies have implied agrin's synaptic stabilizing role [8, 26-28], Tourovskaia's finding that agrin locally stabilized AChR clusters was the first such direct evidence *in vitro* [29]. This result contradicts with experiments that applied agrin in bath and showed that it caused AChR *depletion* in pre-existing laminin-induced AChR clusters. We believed that these inconsistent results were due to the non-physiological bath agrin presentation. In this dissertation, we sought to explore the controversial question of whether agrin induces, stabilizes, or induces *and* stabilizes AChR receptor clusters in NMJ synaptogenesis. To achieve this goal, we focused on developing an *in vitro* system to answer this question.

1.2.4 *In vivo* versus *in vitro* approaches to studying NMJ biology

Advances in imaging techniques have enabled the *in vivo* tracking of NMJ development over time [30]. Lichtman and colleagues created transgenic mice whose motor axons were labeled with Green Fluorescent Protein (GFP) and its spectral variants (XFP). Multiple motor axons can be labeled with different spectral variants of XFP, allowing each of the competing axons to be followed in the synaptic competition process [30]. From these studies, it was revealed that the synaptic competition process did not

follow a predictable trajectory [31]. In some cases when it seemed like one axon was gaining ground to eliminate its competitor, the "losing" axon would come back and eventually "win." It is clear that synaptic competition is a dynamic event that needs to be actively watched. Although *in vivo* imaging of AChR clustering in embryonic NMJs has provided great insight, it is extremely challenging, expensive, and requires expertise limited to only a few laboratories in the world. Moreover, it is difficult in *in vivo* studies to directly and dynamically apply biochemical manipulation in hour-long experiments, i.e. have control of the timing, duration, and doses of neurochemicals and the microenvironment. In contrast, *in vitro* imaging of AChRs in muscle cultures is relatively straightforward. Fluorescently-labeled bungarotoxin (BTX), a commercially-available snake venom that binds to the α subunit of AChR, can be used as a marker of AChRs in both live and fixed muscle cultures.

One of the advantages of the NMJ model for synaptogenesis is that it can be studied in culture using either primary muscle cells or muscle cell lines, e.g. the C2C12 myoblast line, which requires minimal expertise and standard equipment. C2C12-derived myotubes are a good model for synaptogenesis as their fusion and myogenesis is accompanied by upregulation of genes involved in the formation of the postsynaptic apparatus including AChRs [23]. Myotube cultures can be monitored overnight using automated time-lapse imaging on a motorized microscope stage. In addition, laminin substrate, which mimics the chemical composition of the basal lamina surrounding muscle cells, has been shown to induce topologically complex AChR "pretzel" structures on the substrate interface of the myotube that mimic the branching pattern of the *in vivo* motor nerve terminal [23]. These AChR pretzels are elliptical, broken at one side, and about the same size as adult NMJs. The fact that aneural prepatterning occurs *in vivo*

suggests that this is likely not a cell culture artifact. The discovery of nerve-independent AChR patterning of the postsynaptic apparatus provides us with an *in vivo*-like model in which we can manipulate and easily observe in *in vitro* experiments.

1.2.5 *In vitro* models of NMJ synaptogenesis

Most *in vitro* NMJ synaptogenesis studies have applied neurochemicals of interest, e.g. agrin and acetylcholine, in a bath covering the entire surface of myotubes [10, 24, 25]. Although these cell culture systems have uncovered much of NMJ molecular biology, bath application is a poor mimic of the *in vivo* scenario, where the motor axon tip releases agrin to a select region of the myotube surface. Conventionally, micropipettes provided the most definitive approach for delivering soluble signals locally to cells or to subcellular regions of cells. However, micropipettes suffer from diffusive broadening of the focal signal, so are unsuitable for longer focal stimulation timescales on the order of hours to days. Furthermore, micropipettes suffer from low throughput, and poor adaptability to on-stage microscope incubators, making live-cell imaging experiments difficult.

Many groups have attempted to recapitulate the localized signaling between nerve and muscle using co-cultures of motor neurons with skeletal muscle cells [32-36]. These experiments successfully demonstrated formation of neuromuscular junctions, marked by co-localization of AChR clusters and presynaptic vesicle markers, synaptophysin, and electrochemical coupling using patch clamp recordings. More sophisticated systems, utilizing micro-scale adaptations of classical Campenot chambers were capable of compartmentalizing the co-cultured cells, enabling motor neurons and muscle to be cultured in separate microenvironments, addressing their disparate culture conditions [37]. Although motoneuron-muscle co-culture systems provided good physiological

mimics, they lacked fluidic isolation and control of the timing and dose of isolated stimuli. Our goal was to build a system where we could observe AChR clustering dynamics in response to single or multiple stimuli in fluidic isolation.

1.2.6 Focal delivery of neurochemicals for study of NMJ synaptogenesis

In parallel to co-culture models, many studies have attempted to mimic localized neuronal presentation of neurochemicals by direct focal stimulation of myotubes in culture. Studies were successful in inducing localized AChR clustering using growth factor-coated microbeads [38], microcontact printing of agrin [39], and co-culture of myotubes with agrin-expressing Chinese Hamster Ovary (CHO) cells [25]. However, these approaches had no control of the location, concentration, onset, or duration of agrin stimulation. The *in vivo* developing NMJ is a dynamic microenvironment, shaped by the spatially and temporally specific secretion of neuronal factors. The shortcomings of previous *in vitro* approaches motivated us to take a microfluidics-based approach to studying NMJ synaptogenesis. Microfluidics, the handling and manipulation of fluids constrained in micron-scale geometries, is a promising direction in the field of cellular neuroscience, offering a high degree of control of the cellular microenvironment [40, 41].

Table 1.1: Comparison of strategies for focal delivery of neurochemicals to muscle in NMJ studies

		Micropipettes	Microbeads	Microcontact printing	Cell co-cultures	Microfluidics
Control of stimulus:	Dose	Yes	No	No	No	Yes
	Timing	Yes	Yes	No	No	Yes
	Position	Yes	No	Yes	No	Yes
	Throughput	Low	High	High	High	High
	References	[14, 15, 42, 43]	[38, 44]	[39]	[25]	[29, 45, 46]

1.3 MICROFLUIDICS FOR FOCAL STIMULATION OF CELLULAR ASSAYS

In the past two decades, microfluidic devices have shown great potential in cell culture applications, with advantages in recapitulating physiological conditions, parallelizing experiments for high-throughput data acquisition, minimizing reagent consumption for reducing costs, and reducing human error due to their high reproducibility [47, 48]. Microfluidics offers a high degree of control of the cell microenvironment because transport phenomena such as diffusion and laminar flow can be mathematically modeled, allowing for computational simulations of local concentrations and flow velocities that can be used to optimize device design. Micropatterning and microfabrication allow single cells to be confined within well-defined geometries, allowing for precise interrogation [49, 50]. Together, microfluidic and micropatterning techniques provide a means to precisely control both the soluble and insoluble microenvironments of cells in *in vitro* platforms. Therefore, microfluidic devices provide key advantages over traditional cell culture platforms in their ability to recapitulate the physiological conditions at the microscale [48, 51]. Microfluidic manipulation has been utilized for the focal stimulation of microdomains of single cells, parts of cells, or tissues in a wide range of applications including: *in vitro* models for tissue development that necessitate spatiotemporal presentation of soluble and physical signals [52, 53], single cell analysis for multi-plexed drug testing [54, 55], localized chemical stimulation of tissue slices for neural electrophysiology [41, 56], and localized neurochemical stimulation of muscle cells [29, 46, 57].

1.3.1 Laminar flow-based focal delivery

Classical microfluidic approaches for localized stimulation in cellular assays have utilized pressure-driven laminar flow in enclosed channels. Laminar flow is the condition

where particles in liquid move in smooth layers, and do not mix except by diffusion [58]. In the large Peclet number regime, where advective transport dominates over diffusive transport, parallel streams can flow alongside each other for long distances without mixing [59]. Takayama et al. developed a microfluidic technique, PARTCELL, using multiple laminar streams to deliver reagents at subcellular resolution to study the phenomena of mitochondrial movement and cytoskeletal changes [60, 61]. Hydrodynamic focusing is an effective strategy of achieving focused flows used in microfluidic devices [62].

In NMJ studies, Tourovskaia et al. developed a device that used heterogeneous laminar flows to focally stimulate micropatterned muscle cells with neurochemicals in a model of neuromuscular junction synaptogenesis [29, 46, 63, 64]. They demonstrated focal microfluidic agrin stimulation of micropatterned myotubes, effectively replacing the motor neuron with a microfluidic stream of agrin delivered to subcellular regions of the myotube surface. These studies showed local agrin-induced clustering of spontaneous AChR clusters [46], as well as metabolic stabilization of AChR pretzels [29] from focal application of agrin.

1.3.2 Membrane-based methods for focal delivery

Some microfluidic focal delivery devices rely on a combination of convection and diffusion-based transport of stimulant through a microporous membrane. These devices are often described as gradient-generating microfluidic devices capable of producing steep gradients, but effectively serve the same purpose of localized chemical stimulation devices. Typically, in a membrane-based device, the stimulant source is transported via microchannels beneath the membrane by either one-time filling [65] or continuous flow [66, 67] and reaches the basal side of cells directly grown on the membrane via diffusion

through the pores. Microporous and nanoporous membranes made of polycarbonate (PC) [67], polyethylene terephthalate (PET) [68], and PDMS [69] have been integrated into microfluidic devices using various bonding techniques. The design of these membrane-based devices were largely motivated by the needs to: 1) compartmentalize cell and fluidic chambers for area-specific stimulation [65, 67, 70, 71], 2) minimize flow-induced shear stresses [66, 67], or 3) compartmentalize cell chambers for polarized cell-cell interactions between multiple cell types [69, 72]. Control of localized fluidic microenvironment via porous membranes enabled studies such as spatially controlled differentiation of pluripotent stem cells [71], gradients for Wnt/Beta-catenin signaling [65], localization of chemokines for circulating breast cancer cell adhesion in an microvasculature model [70], and control of embryoid body size [73]. In previous NMJ studies, Kosar et al. developed a planar nanoholes microdevice that featured myotubes cultured on a silicon nitride membrane with 2-8 μm diameter apertures that addressed the cells from the basal side [45]. When agrin was applied focally through the nanoholes, AChR clusters were observed on myotubes overlying the holes.

1.3.3 From closed to open-chamber microfluidics

Conventionally, both laminar flow-based and membrane-based microfluidic devices operated in a format where cells are cultured inside enclosed micro-chambers, leading to a number of drawbacks [54, 74]. First, the high surface area-to-volume ratio of microchannels makes the cells susceptible to nutrient shortage and buildup of metabolic waste [75]. Therefore, this susceptibility necessitates continuous media replenishment using perfusion to maintain nutrient levels, pH, and gas concentrations in microcultures [64, 75]. For example, C2C12 myotubes require long-term culture conditions: it takes ~ 4—6 days for single myoblasts to fuse into mature myotubes in low-serum medium.

Microfluidic systems that require constant perfusion on such long timescales often prove to be cumbersome. Second, due to the inherent differences between microculture and macroculture environments, biological data obtained from closed channel microfluidic devices are difficult to compare with conventional cell culture experiments [76, 77]. Conditions for sensitive cell types for long-term biological experiments need to be adjusted specifically for microfluidic devices, creating another barrier for use by life scientists outside of the microfluidics community [76]. Third, closed channel microfluidic devices suffer from disadvantages such as high hydraulic resistance, difficulty to introduce cells and tissues, and clogging by particulates and air bubbles [78]. Fourth, flow-induced shear stresses may confound the biology of interest and have deleterious effects on cells, e.g. affecting ion channel activation [79], motility [80], or in the case of sensitive cell types such as neurons, even causing cell death [81].

To address the numerous drawbacks of closed microfluidic systems, several groups have developed "open-chamber" devices that operate within an open architecture without sealed channels and chambers [52, 54]. A central goal is for devices to deliver localized chemical stimulation to large cell culture surface areas and tissues in open architectures. Many designs seek to create a user-friendly experience for the researcher and a more benign microenvironment for the cells [74, 82, 83]. In open-chamber designs, in which cells are bathed in the bulk media bath like in a petri dish, results can be directly compared with conventional cell cultures. Open chamber microfluidic devices circumvent the media-replenishing problem of closed devices by operating within an open reservoir, allowing for easy media exchange. Furthermore, open-chamber devices allow straightforward cell seeding by simple top-loading with a pipette.

1.3.3.1 Open-chamber laminar flow-based devices

The author's group, the Folch Lab, developed a class of open chamber gradient-generating devices known as "microjets." The device operated at low flow rates, which applied minimal shear stresses and was shown to be benign to mammalian neurons [74, 84]. Delamarche and colleagues developed a class of devices using hydrodynamic focusing known as microfluidic probes (MFPs). These devices combined the concepts of laminar flow microfluidics and scanning probes to perform noncontact localized chemistries on surfaces [85, 86]. MFPs had high enough resolutions to individually address small groups (two to four) of cells [87].

1.3.3.2 Open chamber membrane-based microfluidic devices

Scott et al. demonstrated focal delivery of chemicals via microchannels bonded to an aperture-defined porous membrane to cultured brain tissue slices in an open reservoir [56]. Cate et al. developed an open chamber gradient-generating device capable of producing steep gradients ~33 μm wide [88]. Notably, this device features an "open face sandwich" architecture where cells, grown on a microporous membrane are exposed to the open bulk cell culture media on their apical side, while receiving localized soluble signal from their basal side via PDMS microchannels. Schematically similar to the open face sandwich concept, several approaches for focal stimulation have relied purely on passive diffusion through porous membranes in the absence of underlying fluidic channels. Takoh et al. developed a device where myocytes were selectively exposed to a soluble stimulant through a PDMS micromask that defined small permeable holes in a porous polycarbonate membrane [89]. Only myocytes overlying the holes were exposed to gap junction inhibitors, allowing observation of effects of selective dosing on cytosolic calcium transients [90]. Similarly, there have been other membrane-based devices

fabricated by PDMS wet microstamping for area-selective basal side delivery for stem cell co-culturing [91] and drug assays [92].

1.4 OBJECTIVES AND DESIGN CRITERIA

The objective of this work was to develop *in vitro* microfluidic models of neuromuscular junction formation. Specifically, in our models, we utilized microfluidic focal delivery of neurochemicals to subcellular regions of cultured myotubes, mimicking the localized neuronal presentation of neurochemicals to muscle. By controlling the *in vitro* neuromuscular junction substrate and fluidic microenvironments, we aimed to study the dynamics and spatial patterns of AChR clustering upon focal application of synatogenic factor agrin.

To achieve these objectives and to optimize the previously discussed advantages, we considered device designs that would satisfy the following criteria:

- ***Focal stimulation:*** reproducible local delivery of soluble stimulants that would be sustainable for up to hours, using either laminar flow or membrane-based approaches.
- ***Amenable to micropatterning:*** device substrate must be compatible with a micropatterning scheme for creating organized myotube patterns for maturation and automated timelapse microscopy.
- ***Cell benign:*** biocompatible cell culture material, and focal fluidic stimulation that imparts minimal shear stresses on cells.
- ***Open chamber:*** device would operate while bathed in the bulk cell culture media, maintaining steady gas/nutrient concentration, pH, and osmotic stability, and permitting long-term (~ weeks) cell cultures.
- ***Amenable to microscopy:*** compatible with phase contrast and fluorescence microscopy and shows good optical clarity.

- ***High-throughput:*** device would feature large arrays of units consisting of myotubes receiving focal stimuli, allowing large-scale parallelization.
- ***User-friendly:*** device is adapted to a common cell culture platform, i.e. 6-well plate, and is easily operable by a non-specialized scientist.

Beyond our goal of building an in vitro model of NMJ synaptogenesis, we aimed to test two hypotheses using our microfluidic systems:

- Agrin is a locally acting AChR pro-clustering factor and this action only occurs locally, not globally on the myotube surface, when stimulus is applied locally.
- Agrin is a locally acting stabilizer of large laminin-induced AChR "pretzels" that resemble the *in vivo* synaptic AChR clusters.

1.5 EXECUTIVE SUMMARY

The overarching goal of this dissertation was to develop a new generation of microfluidic focal stimulation devices for the study of neuromuscular junction synaptogenesis. We first aimed to engineer focal stimulation microfluidic platforms that satisfied the criteria established in the previous section, of operating in open format, being compatible to micropatterning techniques, cell benign, amenable to microscopy, high-throughput, and user-friendly. In **Chapter 2**, we describe a laminar flow-based strategy for generating focal streams of soluble reagents in open space, directed to micropatterned C2C12-derived myotubes and primary myofibers. Independently, in **Chapter 3**, we describe a novel, fluorosilane-based micropatterning method for the long-term confinement of cells that is versatile for a multitude of substrates. To further satisfy the criteria of a cell benign, high-throughput and user-friendly device, we tested another design: a modified Transwell focal stimulation device that operates based on passive diffusion, described in **Chapter 4**. Finally, in **Chapter 5**, we address the hypotheses of agrin-induced AChR clustering and stabilization. We demonstrated with our Transwell microfluidic platform, with a large sample size, that focal agrin application induced localized AChR microcluster formation. Surprisingly, we found that focal agrin had no effect on the rate of AChR loss, but may *decelerate* the rate of receptor insertion in myotubes. These results corroborated with bath agrin studies but refuted previous focal agrin studies. Together, we have built and characterized a suite of microfluidic platforms for muscle cell culture, and applied the system to understanding AChR clustering dynamics in the context of NMJ synaptogenesis.

CHAPTER 2: AN OPEN-CHAMBER FLOW-FOCUSING DEVICE FOR FOCAL STIMULATION OF MICROPATTERNED CELLS

2.1 SUMMARY

Microfluidic devices can deliver soluble factors to cell and tissue culture microenvironments with precise spatiotemporal control and enable high throughput experiments. However, enclosed microfluidic environments typically result in low cell viability, especially for experiments requiring long-term cell culture. Therefore, we developed a user-friendly open-chamber hydrodynamic focusing device allowing for focal delivery of soluble agents to cells over long time periods (i.e. several hours). We demonstrated the advantage of the open-chamber feature by differentiating myoblasts into myotubes, a process, which normally occurs over 7 – 10 days and is difficult to achieve in closed-chamber microfluidic devices. We integrated a microfabricated trench or a series of microwells into the microfluidic device for patterning myoblasts or trapping individual primary myofibers, respectively. By controlling the flow-rates and altering the device geometry, we were able to produce sharp focal streams with widths ranging from 36 μm to 187 μm. The focal streams were stable: having about 11.5% relative standard deviation between units and showing 20% increase in stream width over 10 hours of operation. We show that mature myotubes, as well as primary myofibers can be cultured in the device using conventional tissue culture techniques. Finally, we demonstrated focused delivery of cytoplasmic and nuclear dyes to micropatterned myoblasts and myofibers.

2.2 INTRODUCTION

Hydrodynamic focusing, the confinement of a central stream by faster flowing side streams, is a promising method to achieve focused microfluidic flows, having been used in applications such as protein gradient generation in hydrogels [93], miniaturized biochemical assays [94], and cell sorting [95]. The flow rates of the center stream and the flanking streams in microfluidic devices can be adjusted to define the width of the focusing stream and the diffusion patterns at the stream interface [96]. Accordingly, many biological events can be closely mimicked based on the simple generation of hydrodynamic focusing streams in microfluidic devices. Previously, Wang et al. and Liu et al. reported closed-chamber microfluidic devices utilizing hydrodynamic focusing for focal delivery of soluble reagents to cells [97, 98]. Chen et al. used a hydrodynamically focused microfluidic device to investigate gap junctions by delivering calcein AM to target cells and tracking its transport into neighboring unexposed cells [99]. While these devices enabled insightful experiments, their utility was limited to short-term experiments on the order of minutes.

In this chapter, we describe a microfluidic device that produces stable, reproducible hydrodynamically focused streams in an "open-chamber" design that can be sustained for long-term operation on the order of hours. The open-chamber design allows for the device to be accessible and cells to be maintained at high viability using conventional cell culture protocols. We demonstrate the advantage of the open-chamber architecture in enabling long-term cell cultures of myoblasts and differentiation into myotubes over 7 – 10 days. Moreover, we coupled the open microfluidic system with a PDMS surface modification technique for long-term attachment and growth of C2C12

myoblasts and a trapping technique for primary muscle fibers. We showed localized delivery of soluble molecules to cells at microscale resolution.

2.3 Materials and Methods

2.3.1 Device Overview

The microfluidic device operates on the principle of hydrodynamic focusing, which involves laminar flow with outer "sheath" flanking streams that hydrodynamically "squeeze" a central focal stream [62, 96]. Using appropriate flow rates, the effect of lateral diffusion of the soluble species can be minimized [62], maintaining a steady state focal stream for long periods of time. Furthermore, by tuning the relative flow rates of the flanking and focal streams, the width of the focal stream can be controlled [96]. In our device (Figure 2.1) the focal stream is ejected into an open cell culture reservoir and applied to focal regions on the apical surface of cells micropatterned orthogonal to the flow direction. Flow is driven by a "push" (syringe-pump-driven positive pressure) and "pull" (vacuum-driven negative pressure) mechanism.

The device consists of three layers of PDMS bonded to a custom-made glass-bottom petri dish. The three layers from bottom to top are: Layer I, the cell patterning layer, Layer II, the perfusion layer, and Layer III, the ports layer (Figure 2.1A, Figure 2.2A). Depending on the application, whether for myotube or myofiber focal stimulation, the cell patterning layer consists of either A) two micro-scale trenches that serve to contain and promote aligned micropatterns of myotubes, or B) two rows of microwells for trapping myofibers. The depressed trenches and microwells serve to shield the cells from flow-induced shear stresses (Figure 2.1B) [100]. The perfusion layer consists of one

focal channel, adjacent to which are two flanking channels which drive flow into an open chamber containing the cells, and apposed on the other side of the open chamber by a vacuum channel which aspirates the flow (Figure 2.1B, C). We define the focal and flanking channel openings as "microjets," as the cross-sectional areas of these openings are much smaller than the rest of the connected fluidic channels [74, 84]. The soluble species diffuses down to the cells on the bottom of the trench or microwell (Figure 2.1B). Finally, the ports layer provides for off-chip connections with inlets for the focal and flanking inputs and an outlet for connection to a vacuum source. The binary network of channels feeding the focal and flanking microjets are connected into two planes by a system of vertical passages (vias) and converge only at the microjets opening at the perfusion layer. We scaled up the device into configurations for large-scale experiments: 32 and 64 sets of focal and flanking channels for the myotubes and myofibers devices, respectively.

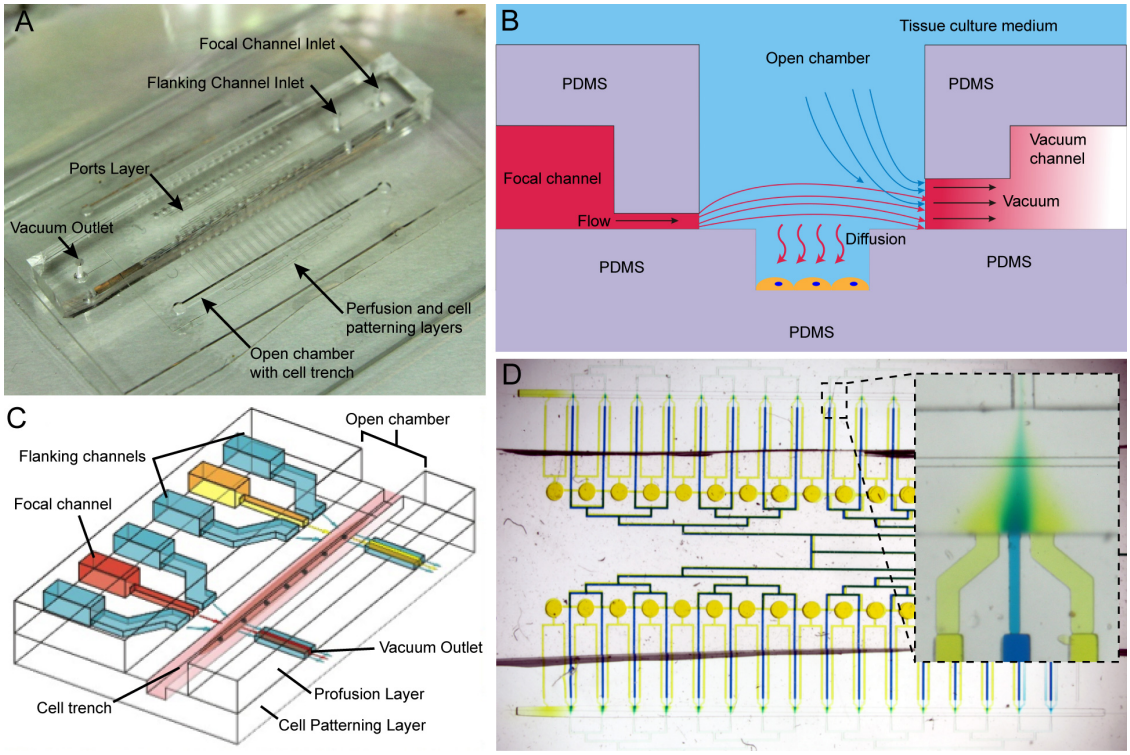

Figure 2.1: Schematics and operation of the microfluidic device.

(A) Photograph of the device shows that the focal and flanking inlets and the vacuum outlet are introduced by a central PDMS inlets layer. The focal and flanking microjets are on a middle perfusion layer, while the cell trench lies within the open chamber (cannot be seen in the picture). (B) A 2D cross-sectional side view of the device through the fluidic channels: there is continuous flow driven by positive pressure from syringe pumps and negative pressure from the vacuum channels. The molecule of interest then diffuses down to the cells, which lie in trenches. Note that cells are open to the media. (C) A 3D schematic shows two sets of focal and flanking channel apposed by corresponding vacuum aspiration channels. The flanking channels effectively squeeze the stream from the central focal channel by hydrodynamic focusing to deliver factors to cells (e.g. myotubes and myofibers) in trenches, which lie in a chamber open to the bulk tissue culture media. (D) The device consists of 32 sets of focal and flanking channels, as represented by the blue and yellow dyes in the focal and flanking channels, respectively. The inset shows one set of focal and flanking channels, showing hydrodynamic focusing of flow.

2.3.2 Fabrication of master molds

Standard photolithography techniques were used to create three SU-8 masters: I) a one layer master for the cell patterning layer, II) a four-layer master for the perfusion layer, and III) a one layer master for the ports layer. Transparency photolithography masks were designed using AutoCAD (AutoCAD 2013, AutoDesk, San Rafael, CA) and printed at 5080 dpi by a high-resolution laser printer (Fineline Imaging, Colorado Springs, CO). Control of feature thickness was achieved by spincoating the photocurable negative photoresist, SU-8 2000 series (Microchem Corp, Newton, MA) of varying viscosities at different spin speeds onto 100 mm silicon wafers (University Wafers, #590). Master I (110 μm thick, defining the cell trenches) was created by spincoating SU-8 2075 at a final speed of 2000 rpm. Master II (Figure 2.2B) (total thickness 400 μm) consists of four SU-8 layers consisting of A) the alignment marks on the wafer periphery (2 μm thick), B) the microjets (20 μm thick), C) the channels (20 μm thick), and D) the open layer which includes the open structures such as the reservoir to the bulk media (for cell seeding and nutrient exchange), and the vias connecting to the inlets layer above it. Alignment of the second and third masks was enabled by alignment marks on the Layer A that were selectively developed and protected from subsequent spincoating by tape (Scotch tape 1/2" x 3/4"). Master III (110 μm thick) was constructed of SU-8 2075 at a final spin speed of 2000 rpm. Wafers were developed in a developer bath of propylene-glycol monomethyl ether acetate (Baker BTS-220 Edge Bead Remover, #6343-05) for 1 h, rinsed with fresh developer, rinsed with isopropyl alcohol (Macron Chemicals #3043-10), and dried with an air gun. The wafers were subsequently hard baked at 200°C with a ramping rate of 100°C/h for 1 h. To assist PDMS release after molding, wafers were passivated by vapor deposition of trichloro(1H,1H,2H,2H-perfluorooctyl)silane (Sigma-Aldrich #448931) in a vacuum desiccator.

(A) Assembly of Layers

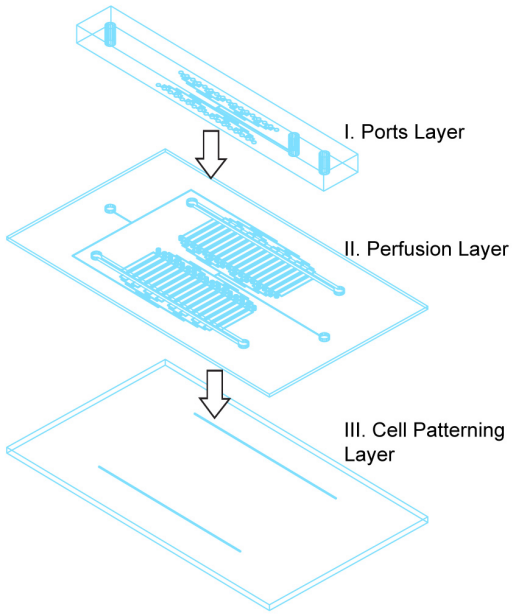

(B) Perfusion Layer Fabrication

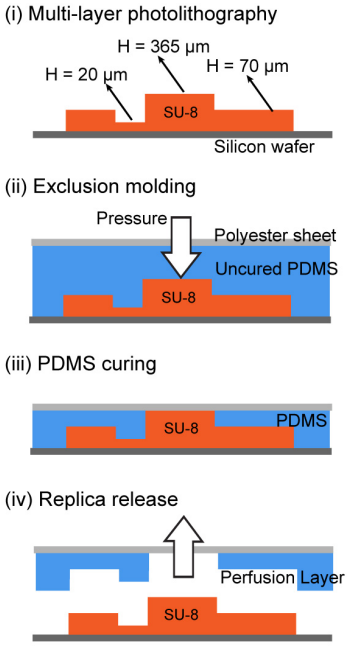

(C) Micropatterning Scheme

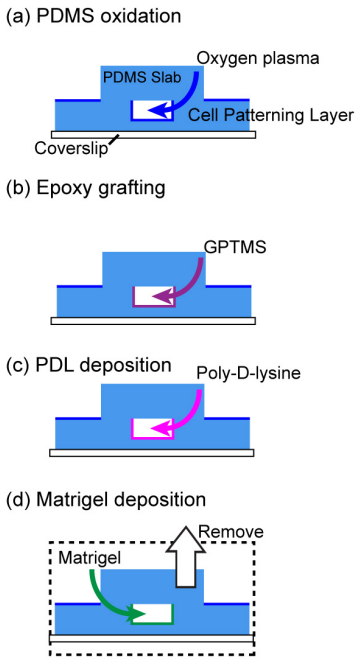

(D) Device Assembly

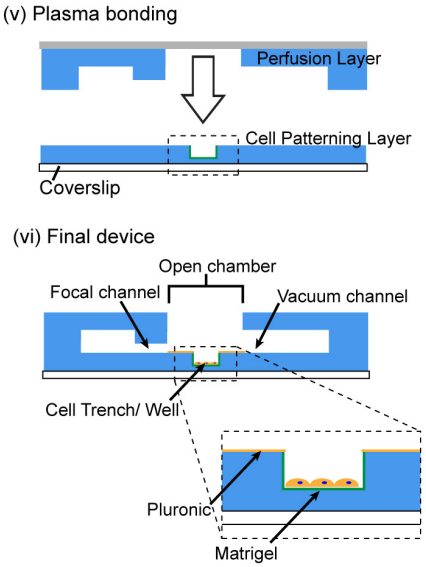

Figure 2.2: Fabrication of the microfluidic device.

The device consists of 3 layers of PDMS from bottom to top: I) the cell patterning layer containing either cell trenches or myofiber wells, II) the perfusion layer containing the focal and flanking microjets, their associated channels, and vacuum channels, and III) the ports layer that contains the inlets and the channels that feed the flanking microjets through a system of vias down to the perfusion layer, and outlets which connect with the vacuum channels. (B) (i) A master mold for the perfusion layer is defined using multi-layer photolithography. (ii)-(iv) Exclusion molding, where PDMS is pressed down to the highest SU-8 features with a polyester sheet backing, is then used to create open reservoirs and vias. (C) For the cell micropatterning scheme, (a) the insides of the cell trench are selectively oxidized by oxygen plasma, (b) an epoxy silane GPTMS is grafted to oxidized PDMS, (C) Polylysine covalent coated onto PDMS to promote (d) protein (Matrigel) adsorption, preserve biological activity, and promote long-term cell attachment. (v) Subsequently, the perfusion layer is bonded to the cell trench layer using oxygen plasma. After bonding, the background areas outside of the cell trenches are backfilled with Pluronic F127 to prevent cell attachment. (vi) In the final device, cells can be easily top loaded into the trenches.

2.3.3 Soft lithography and exclusion molding

The cell patterning layer (Layer I) and the ports layer (Layer III) were molded by standard PDMS replica molding. PDMS (Sylgard 184 Silicone Elastomer Base and Curing Agent, Dow Corning) was mixed at a 10:1 ratio of elastomer base to curing agent, degassed in a vacuum desiccator, poured onto the masters, and cured at 70°C overnight. An established method from our group, termed “exclusion molding” [101], was used for creating open structures in PDMS for the perfusion layer (Layer II). Here, the master mold was placed onto four sheets of polyester film (Scotchpak 9744 PET film, 3M, St. Paul, MN) on a 4” diameter, 0.5” thick steel disc (McMaster-Carr, Santa Fe Springs, CA). PDMS (Sylgard 184 Silicone Elastomer Base and Curing Agent, Dow Corning) was mixed at a 10:1 ratio of elastomer base to curing agent, de-gassed in a vacuum desiccator, and poured onto the masters. Prior to molding, a polyester film was treated under oxygen plasma at 60 W, at 670 mtorr, 30 s. This plasma treatment prior to exclusion molding allowed the stiff polyester backing to be non-covalently adhered to the cured PDMS,

ensuring intact release of the fragile thin PDMS layer. The plasma-treated side of the film was then placed onto the uncured PDMS, taking care to prevent trapping of air bubbles. Four additional sheets of polyester film were placed over the first sheet, topped by an acrylic disc, then compressed using a no-twist C clamp (#5046A18, McMaster-Carr), with a pressure such that PDMS was visibly excluded from the tallest SU-8 features, and finally cured at 70°C in a convection oven for 2 hours. The perfusion layer (Layer II) of PDMS was gently released using a sharp blade with the polyester sheet backing still adherent on it. A 25 μm tip micro probe (Bonn Microprobe, #10030-13, Fine Science Tools, Foster City, CA), was used to verify, under a stereomicroscope, that exclusion-molded vias and inlet holes were open.

2.3.4 Device assembly

From bottom to top, the device consisted of the glass-bottom petri dish, the cell patterning layer, the perfusion layer, and the ports layer (Figure 2.2A). All devices were contained within modified tissue culture polystyrene 100 mm petri dishes (BD Falcon #353003) with No.1 glass coverslip bottoms (Gold Seal 65x48 mm No. 1 coverslip). Rectangular holes (50 mm x 38 mm) were laser-cut into petri dish bottoms. Glass coverslips (Gold Seal Cover Glass #3335) were cleaned in Contrad 70 detergent (Decon Labs) for 2 hours, dried with nitrogen gas and 70°C convection oven, and then bonded to the petri dish using a double-sided tape containing both silicone and acrylic pressure sensitive adhesives (#SA 1020, Adhesive Applications, Easthampton, MA). The acrylic adhesive side was applied to the petri dish, providing a silicone adhesive side to bond the glass coverslip, creating a seal that prevented leakage. Additionally, a 10:1 ratio of PDMS elastomer base to curing agent was applied around the perimeter of the glass-plastic interface and cured at 70°C to create a PDMS sealant. The cell patterning layer

(Layer I) was bonded to the glass bottom petri dish using oxygen plasma bonding (Diener Zepto, 60 W, 670 mTorr, 60 s) followed by heating on a hot plate at 85°C for 5 min. All PDMS-PDMS and PDMS-glass bonding were done using these oxygen plasma parameters. The fluidic part of the device, Layers II and III were aligned under a stereomicroscope and bonded using oxygen plasma. For the ports layer (III), inlets for the focal and flanking channels and an outlet for vacuum channels were punched using a 1.00 mm core biopsy punch (Harris Uni-core, Sigma Aldrich #Z708801).

2.3.5 Device operation and characterization of focal stream

The device setup is shown Figure 2.3. Flow was driven simultaneously by both a positive pressure source (two syringe pumps) and a negative pressure source (vacuum). Syringes (ranging from 3 mL to 25 mL) carrying the focal and flanking solutions (BD Falcon #309604) were mounted on separate syringe pumps (Kent Scientific, Chemyx Fusion 200 Syringe Pump) and connected to the ports layer of the device via stainless steel 19 gauge blunt needle connectors using Cole-Parmer silicone tubing (0.020 in. ID, 0.092 in. OD, #95609-18) for dye-based experiments or Sanipure silicone tubing (1/32 inch ID, 3/32 inch OD, Cole Parmer #96132-00) for cell-based experiments. Flow rates between 100 μL/h to 3000 μL/h were used to drive flow. Low adsorption Sanipure silicone tubing was used to minimize protein adsorption and loss. House vacuum was also connected to the vacuum outlet using the same connector type. A vacuum regulator (Airtrol) was used to control the vacuum strength, which was measured by a vacuum gauge (Ashcroft). The vacuum was set to a pressure (1 psi) that is low enough to minimize shear stress on cells yet capable of generating focal streams. For experiments on delivery of soluble reagents to live cells and myofibers, devices were imaged on an on-stage incubator, with a temperature controller and 5% carbon dioxide source.

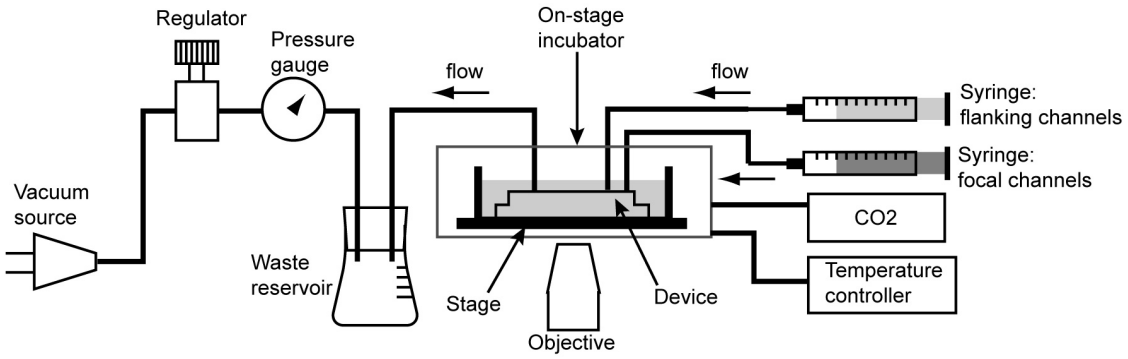

Figure 2.3. Device setup.

Negative pressure (house vacuum) is controlled by a regulator and pressure gauge. Flow is driven by two syringe pumps containing the focal and flanking channel solutions. For cell experiments, the device was enclosed within an on-stage incubator with temperature control and CO_2 source.

In pilot studies on device operation, blue and yellow food coloring dyes (FD&C Yellow #5 – tartrazine and FD&C Blue #1 – erioglaucine) were delivered through the focal and flanking channels, respectively, and observed under a stereomicroscope. To measure the effectiveness of focal soluble factor delivery to specific regions, we used fluorescently-labeled bovine serum albumin (BSA): Alexa Fluor 594 BSA conjugate (7.6 μM, #A13101, Life Technologies) to quantify the stream width. Bovine serum albumin was chosen as a model protein to simulate the transport of large molecules of interest, e.g. proteins. For quantification of long-term stream stability, we used 10 kDa Dextran-Alexa Fluor 594 conjugate at 10 μM (#D-22913, Life Technologies). Here, Dextran was chosen due to its low surface adsorption, reducing the likelihood of fluorescence accumulation and signal saturation during long timelapse acquisitions. Operation conditions, including focal and flanking flow rates of 100 μL/h and 400 μL/h respectively, and a vacuum negative pressure of 1 psi, were kept constant in stream stability experiments.

Fluid flow in the devices was measured using standard epifluorescence microscopy and stereomicroscopy. Epifluorescence microscope images were acquired

using a Nikon Eclipse TE 2000-U model inverted microscope with Nikon Plan Fluor 4X / 0.13 NA, Nikon Plan Fluor 10X / 0.30 NA, and Nikon Plan Fluor ELWD 20X / 0.45 NA objectives, fluorescence filter turrets (Nikon Instruments, Melville, NY) with a 12-bit cooled CCD camera (ORCA-ER, Hamamatsu, Japan) with an automated stage. Image analysis was performed using Fiji (ImageJ) software and curve fitting and statistics done with the MATLAB curve fitting toolbox. To characterize the stream width, we took fluorescence images of the same field of view of each of the 32 channels under varying flow conditions. A 1344-pixel wide linescan was taken in the open chamber along a line, which was equidistant from the focal channel and the vacuum channel. The full width at half maximum (FWHM) fluorescence intensity was then obtained to represent the stream width.

2.3.6 FEM simulations

The 3D simulation of the open-chamber hydrodynamic focusing device was generated using the finite-element software COMSOL Multiphysics (COMSOL, Burlington, MA). The Laminar Flow module was used to define the pressure driven flow. The Transport of Diluted Species module was used to define the concentration inlets of focal and flanking channels with BSA (M.W. = 60 kDa) as the diffusing species (diffusion coefficient, $D = 4 \times 10^{-8}$ $m^2 s^{-1}$) to simulate concentration profiles at the open chamber region.

2.3.7 PDMS surface modification, Matrigel coating and plasma bonding

To selectively render the insides of the PDMS cell trenches hydrophilic and permissive to cell adhesion while keeping the outside regions hydrophobic and non-permissive to cells, a PDMS slab (2.1 cm x 2.1 cm) spanning the length of the trenches was placed in conformal contact, covering the open trenches and turning them into

microchannels. Oxygen plasma was then applied (60 W, 670 mTorr, 60 s) to create hydroxyl groups on the inner surfaces of the PDMS trenches (Figure 2.4). 50 μL of GPTMS (1% v/v in H_2O, Sigma Aldrich #440167) was then drawn into the trenches using a Pasteur pipette connected to house vacuum, incubated at room temperature for 20 minutes, and washed three times with sterile H_2O. Subsequently, 50 μL of a positively charged polyamino acid, 100 μg/mL poly-ornithine (Molecular weight 30,000-70,000, Sigma Aldrich #P4957, St. Louis, MO), was flowed through the covered trenches, incubated for 1 h at room temperature, and washed three times by flowing sterile H_2O through the trenches. The basement membrane extract Matrigel (BD Biosciences #356234, San Jose, CA), diluted 1:50 in Dulbecco's Modified Eagle's Medium (DMEM, Gibco, Invitrogen, #11995), was infused into the trenches, allowed to polymerize at 37°C for 30 minutes, and dried for 5 hours or overnight within the trenches. Matrigel, a mouse sarcoma extract rich in extracellular matrix components, provided a cell culture substrate that mimics the skeletal muscle basement membrane. After Matrigel coating, the fluidic part of the device, Layers II and III were aligned and bonded together using oxygen plasma. Surprisingly, these bonding steps did not negatively affect the Matrigel coating, as discussed in Section 2.4.4. After bonding, PDMS was allowed to recover hydrophobically such that the non-permissive regions outside of the cell trenches would adsorb Pluronic. Pluronic is a triblock copolymer consisting of a central hydrophobic poly(propylene oxide) (PPO) block, which is known to adsorb to PDMS by hydrophobic interactions [102, 103], flanked by two blocks of poly(ethylene oxide) (PEO), known to repel protein adsorption and cell adhesion. The device was bathed in Pluronic F127 (0.2% w/v in PBS, Invitrogen, #P6866), $[(PEO)_{100}\text{-}(PPO)_{70}\text{-}(PEO)_{100}]$ for 1 h. To eliminate bubbles from microchannels, the device was de-gassed in a vacuum desiccator for 1 h prior to cell seeding and operation. For cell culture experiments, the device was

naturally de-bubbled for the course of 7 days by the high CO_2 environment of the cell culture incubator.

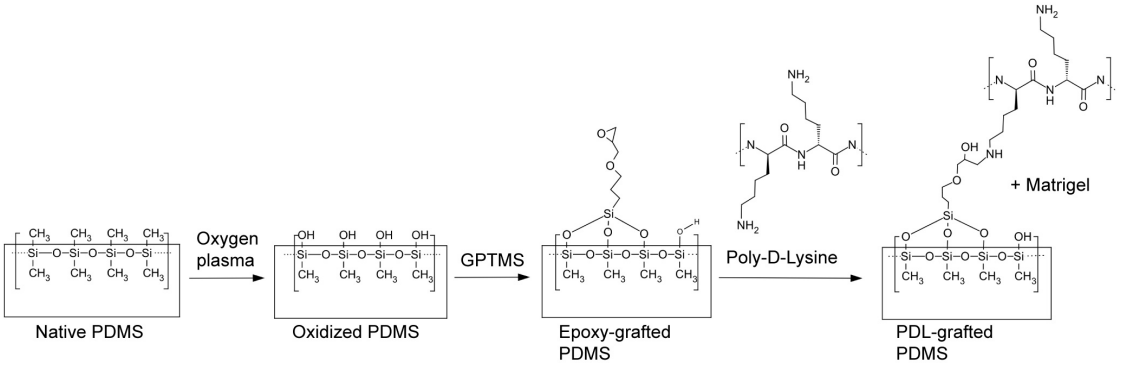

Figure 2.4. PDMS surface modification chemical reaction scheme.

We covalently modified PDMS trenches for long-term cell culture. The native PDMS is oxidized by oxygen plasma to create hydroxyl groups. Subsequently, the available hydoxyl groups react with the epoxy-silane, GPTMS to create epoxy-grafted PDMS. The free epoxide groups can then react with poly-D-lysine (or poly-ornithine) to create a positively charged surface that promotes protein attachment (i.e. Matrigel coating).

2.3.8 C2C12 cell seeding and culture

The myotubes were derived from the mouse myogenic cell line C2C12 (American Type Cell Culture #CRL-1772, Manassas, VA). Myoblasts were expanded on gelatin-coated (Sigma-Aldrich, #1393) petri dishes in DMEM supplemented with 20% fetal bovine serum (FBS, PAA Laboratories) and 1% penicillin/streptomycin in a 5% CO2 incubator at 37 °C. Cells were passaged at 80% confluence to prevent differentiation and were used before passage 10. Cells were seeded as a 400 μL droplet (4.0 x 10^5 cells/mL) on top of the trenches and allowed to settle by gravity and attach for 25 minutes in the cell culture incubator. Cells that did not attach were rinsed away with three washes of media. Cells were allowed to grow for 24 hours or longer until confluence inside the trenches, after which media was changed to low serum differentiation media (DM):

DMEM supplemented with 2% horse serum (Sigma-Aldrich #H1138) and 1% antibiotic/antimycotic, and replenished every 2 days. C2C12 myoblasts were allowed to fuse into mature myotubes for 7-10 days after switching to DM.

2.3.9 Myofiber harvest, culture and microfluidic device adaptation

Muscle fibers from mouse hindlimbs were harvested and cultured using a previously described method [104]. All animal procedures were approved by the Institutional Animal Care and Use Committee of the University of Washington, and were performed in accordance with guidelines of the National Institutes of Health and the Association for Assessment and Accreditation of Laboratory Animal Care (AAALAC). Adult C57BL6 mice, 2 months – 1 year old (Jackson Laboratories), were euthanized by cervical dislocation and the flexor digitorum brevis (FDB) muscles were immediately dissected. The myofibers were dissociated from the muscle in 0.2% collagenase (Sigma-Aldrich, #C0130) solution in DMEM for 2-3 hours in a cell culture incubator at 37°C. Using a sterilized, scored and flame-polished Pasteur pipette, the collagenase-digested muscle was triturated, liberating myofibers. The myofibers and their associated satellite cells were further purified from fibroblasts and other mononuclear cells by passing the digested muscle solution through a series of three horse serum-coated glass centrifuge tubes (Corex, 10 mL glass centrifuge tube, Cole Parmer) and collecting the myofibers from the bottom of the column. Individual myofibers could be manipulated and hand picked using a P-20 micropipette. Under a stereomicroscope, the myofibers were suspended in solution above the microwells using a P-10 micropipette and then allowed to settle by gravity into microwells. For myofibers, the microfluidic device design was altered to contain 64 focal stimulation channels with 128 flanking channels. Microwells for trapping myofibers had dimensions of L x W x H = 400 μm x 80 μm x 110 μm or 360

μm x 60 μm x 110 μm. The microwells were offset during the plasma bonding process such that one end of the well was aligned to the focal channel and the other end was distal to it. This configuration allowed application of a focal stream on one end of the myofiber, effectively generating a gradient along the length of the myofiber.

2.3.10 Focal delivery of soluble factors to myoblasts and myofibers

Calcein AM (5 μM, #C3100MP, Life Technologies) was applied onto myoblasts for 30 minutes using focal and flanking flow rates of 200 μL/h and imaged in the GFP channel. Hoechst 33342 and Hoechst 33258, both at 5 μg/mL (#H1399, #H3569, Life Technologies) in PBS were used to label myoblast and myofiber nuclei, respectively. For image processing of Hoechst 33258 labeling of myonuclei, the individual myonuclei were manually segmented using Fiji (ImageJ) software by thresholding the fluorescence images at four different levels such that the regions of interest (ROIs) of the nuclei appeared at each thresholding level. The position and mean intensities of the resulting nuclei ROIs were recorded and plotted as a scatterplot of x-position from focal channel versus normalized intensity (mean intensity of nucleus / mean intensity of brightest nucleus).

2.4 Results and Discussion

2.4.1 Characterization of focal stream

We characterized the capability of the device to control steady state streams of BSA-Alexa Fluor 594 (Figure 2.5A). We showed that stream width, defined as the linescan FWHM, can be controlled by varying the ratio of the flanking and focal flow rates, k. We tested this phenomenon in two device formats: open chambers with 600 μm

and 200 μm separation distances between the focal and vacuum channel openings. In the 600 μm gap device, we were able to vary the stream width ranging from 71 μm at k = 12, to 187 μm at k = 0.25. In the 200 μm gap device, we obtained stream widths ranging from 36 μm at k = 20, to 75 μm at k = 1. In Figure 2.5B, the plot of k versus focal stream width, shows an inverse relationship, which is consistent with theoretical models [105]. In both device formats (200 μm and 600 μm), our experimental results indicate that the stream width follows an inverse relationship between k and the stream width (Figure 2.11).

We further characterized the surface level fluorescence of BSA-Alexa Fluor 488 after one hour of continuous flow (Figure 2.5C). After multiple washes with PBS, a fluorescence pattern similar to the active flow pattern remained on the PDMS substrate, indicating that fluorescently-labeled BSA had locally adsorbed onto the substrate. This result is notable because it indicates that BSA deposited locally to the regions of the cell trench underneath the focal stream, suggesting that cells would locally receive the soluble signal. In Figure 2.5**C**, the bright signal on the upper trench wall may be due to the presence of a dead zone where BSA signal accumulated over time, thereby creating an especially bright signal.

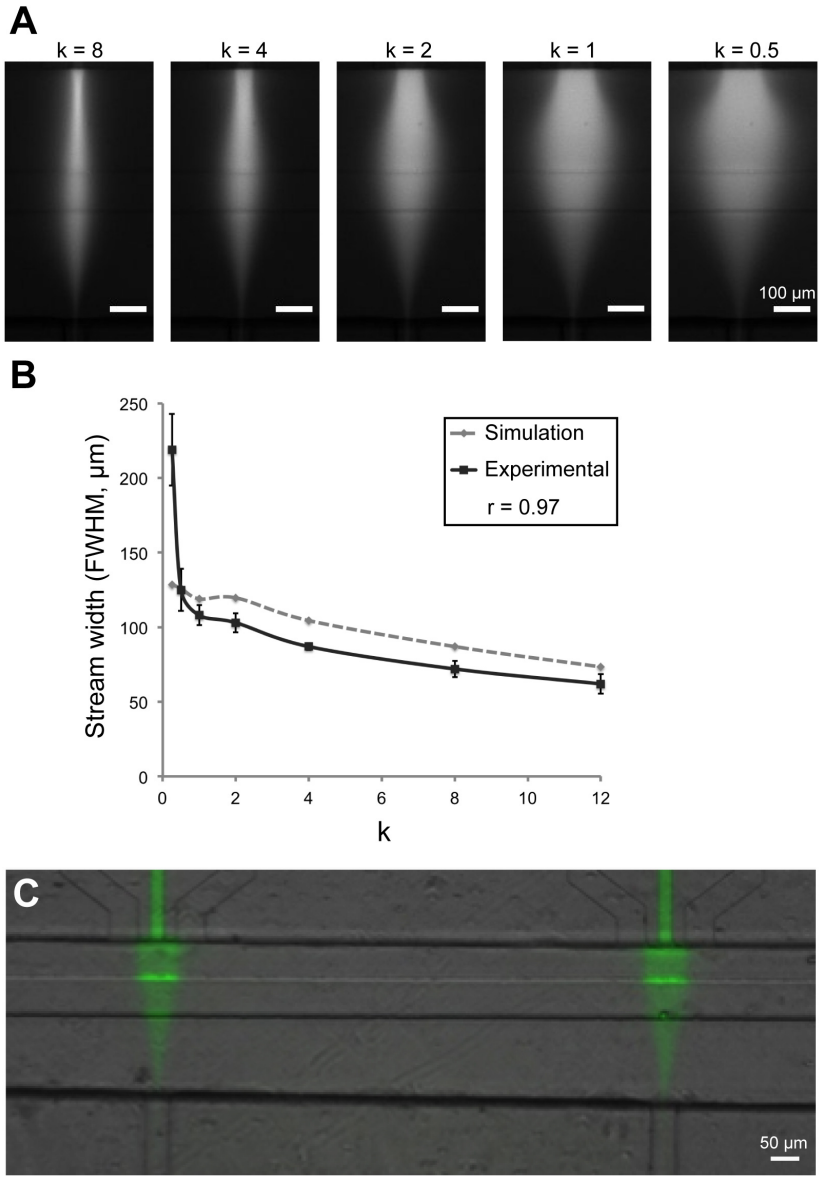

Figure 2.5: Characterization of hydrodynamic focusing control of microfluidic device.

(A) The width of the focal stream (BSA-Alexa Fluor 594) can be controlled by adjusting the relative flow rates of the focal and flanking channels. The ratio k indicates the relative magnitudes of the flow rates of the flanking to focal channels. (B) The stream width (FWHM) is plotted as a function of k, the ratio of flanking to focal flow rates, showing an inverse relationship. The dotted grey line and solid black line show the simulation and experimental stream widths, respectively, and have a strong correlation (r = 0.97). (C) A pattern of BSA-Alexa Fluor 488 that deposited onto the floor of the device, including the bottom of the cell trench. This demonstrates that a focal stream of soluble factors deposited locally onto the substrate.

2.4.2 FEM simulations of local concentrations and shear stresses

For the concentration profile, we performed FEM simulations of the experimental flow parameters for one single unit of the device, i.e. one focal channel paired with two flanking channels (Figure 2.6A, B). We held the focal channel flow rate constant and varied the flanking channel flow rate to simulate changes in the concentration profile. Similar to the analysis of the experimental stream fluorescence images, linescans of the concentration were taken midway between the focal jet opening and the vacuum channel opening under 7 flanking flow conditions (Figure 2.6C). From the simulations, we observed an inverse relationship between k, the ratio of flanking : focal flow rates, and the width of the focal stream. At each given flow condition except k = 0.25, simulated stream widths were found to be strongly correlated with experimental stream widths, with Pearson correlation coefficient, r = 0.970 (Figure 2.5B). One exception was at an extremely low flanking flow rate of 25 μL/h (k = 0.25), where correlation was poor, likely due to higher dominance of diffusion. Our simulation results show that the flanking flow rate should be at least 4 times higher than the focal flow rate to minimize diffusion of the species into the culture bath.

In our microfluidic system, it is important to consider the effect of flow-induced shear stresses on cultured cells. Shear stress from microfluidic flows may be deleterious to cells, introduce migration bias, and generally alter the underlying biology of interest [80, 106]. For example, Bhattacharjee et al. from the author's group reported that 0.7 dyn/cm^2 was benign to neurons, some of the most sensitive cell types to shear stress [74]. We designed a micro trench for cells to be confined and shielded from flow-induced shear. Due to the difficulty of experimentally measuring shear stresses on cells, we included simulations of local shear stress in our COMSOL model. Figure 2.6D and E

show plots of local flow velocities with 3 different outlet pressures and 3 different flow velocities at 10 μm above the bottom of the trench. The range of velocities simulated, 10 μm/s to 100 μm/s, are well below the range of 500 μm/s to 1500 μm/s high enough to introduce chemotactic migration bias [84]. The trench significantly reduces the shear stress across the cell culture area and makes the cell culture surface less sensitive to the change of the outlet flow velocity.

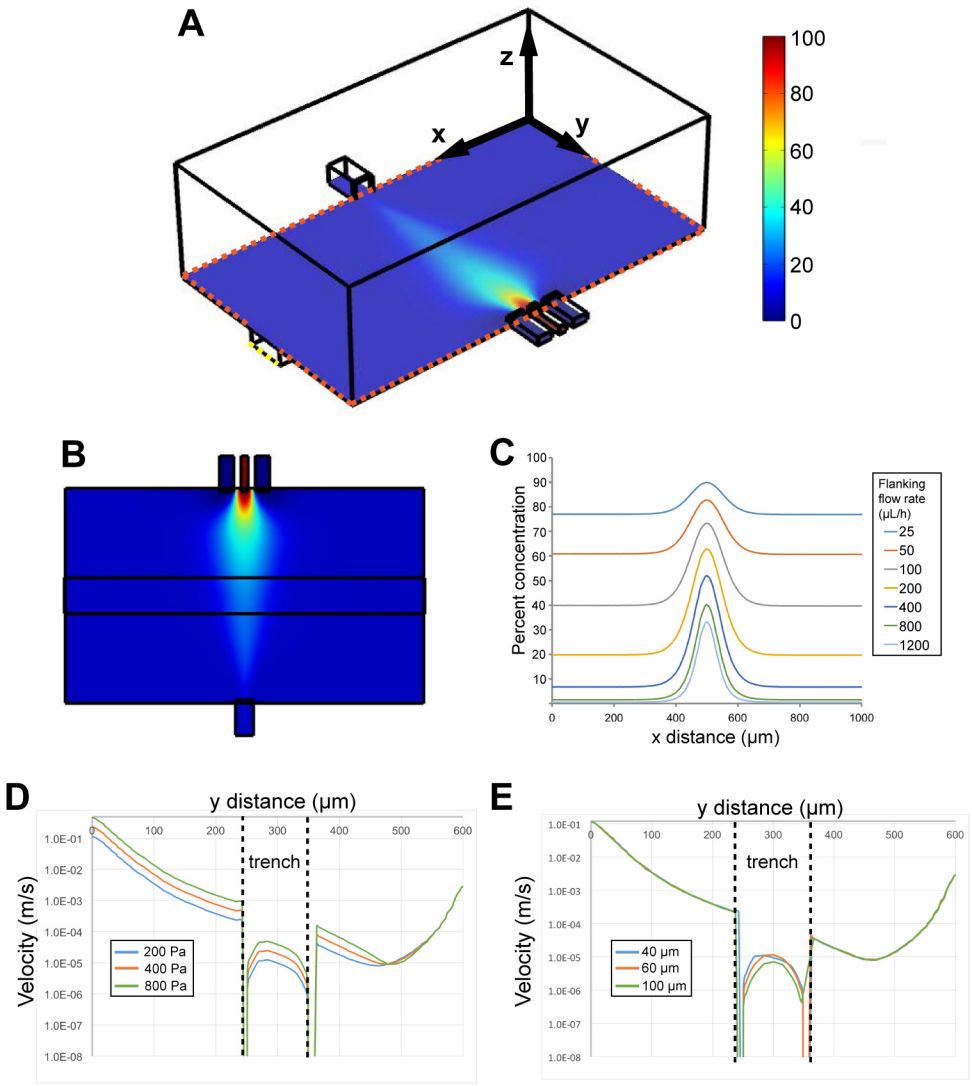

Figure 2.6: Computational simulations of local concentrations and velocities.

(A) An isometric view of one unit, showing the xyz coordinates, and a color map of local concentrations at the plane of the bottom of the channels. (B) Top view colormap of one unit. (C) A plot of the simulation linewidths at a constant focal channel flow rate of 100 μL/h, and 7 varying flanking channel flow rates ranging from 25 μL/h to 1200 μL/h. Note that there is considerable lateral diffusion of species, resulting in much higher baseline concentrations outside of the focal stream at lower flanking flow rates. (D) Velocity plot, with varying vacuum pressures. Note the drop in local velocities inside the cell trench, marked by the dotted line. (E) Velocity plot, with varying trench depths. Note the drop in local velocities inside the cell trench. Figure credit: Chi-Ting Chang.

2.4.3 Characterization of focal stream stability and reproducibility

One key feature of this microfluidic system is the ability to generate multiple parallel focal streams, enabling high throughput cell experiments. To determine focal stream reproducibility between microjets, we quantified the position and stream widths of fluorescent Dextran in 31 of the total 32 microjets averaged over a timespan of 10 hours. Here, one microjet's field of view, which was obscured by a dust particle, was discarded in the analysis. We characterized two parameters of focal stream stability: 1) the stream width, as defined by the full width at half maximum (FWHM) of the linescan curve, and 2) the stream position, as defined by the x-displacement of the linescan curve maximum from its initial position. The stream x-displacement was calculated by obtaining the x-position of the linescan maximum at each timepoint and subtracting the x-position of the maximum at the initial timepoint. In Figure 2.7A, we show a plot of 49 superimposed linescans of a single representative microjet over 10 hours of device operation. Here, all timepoint images were background-corrected such that the baseline minima of all linescans were equal. We observed that the linescan FWHM only increased 7.9% from 138 μm at the initial timepoint to 149 μm at 9.75 hours. Moreover, the standard deviation of the mean x-displacement was 9.7 μm, which was only 6.5% of the FWHM, indicating the consistent positioning of the focal stream. In Figure 2.7B, we show the time-averaged stream widths of the 31 microjets. The average stream-width over all the microjets was 147 $\pm$ 17 μm. Therefore, under the same flow conditions, the device can generate multiple focal streams with less than 12% variability. The variation in stream widths between microjets may be attributed to channel clogging due to fabrication imperfections, particulates or air bubbles. The position of the focal streams also showed very little variation between microjets (Figure 2.7C), as the average displacement for all jets was 3.3 $\pm$ 6.9 μm. Over 10 hours of operation, the cumulative average stream width of all

microjets changed from 134.5 $\pm$ 20.8 μm to 161.7 $\pm$ 20.6 μm, a 20% increase (Figure 2.7D), whereas the cumulative average position shifted by only 4.8 $\pm$ 10.0 μm (Figure 2.7E). The stream width increase over time may be due to a decrease in negative pressure, possibly attributed to a drop in the hydrostatic pressure head from depletion of the petri dish bath or possibly from particulates clogging the vacuum channels. Furthermore, surface accumulation of Dextran onto PDMS may have contributed to increased fluorescence intensity, effectively broadening the stream width. Together, these results showed that the focal streams generated in this open chamber microfluidic device have low variability between multiple microjets and were stable over long-term operation timescales. The low variability between microjet units allows the potential for future parallelization with more high-throughput designs.

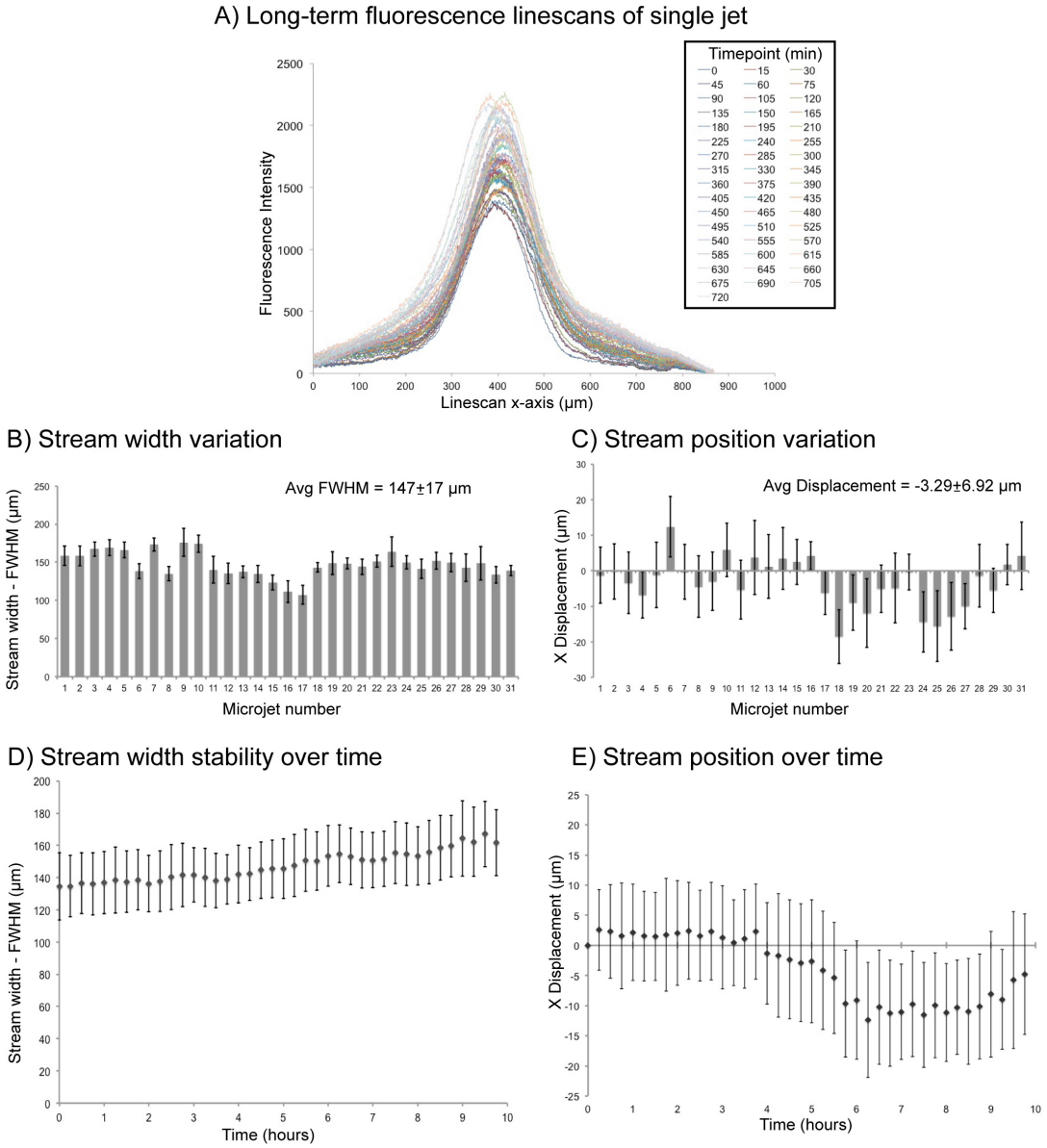

Figure 2.7: Characterization of focal stream reproducibility and long-term stability.

(A) Linescans of a focal stream of Dextran 10kDa - Alexa Fluor 594 at 49 timepoints taken in 15 minute intervals over a 10 hour operation period. (B) The time-averaged stream widths of 31 microjets in a single device. (C) The time-averaged x-position of the stream maximum intensity relative to its original x-position in the 31 microjets averaged. For B and C, error bars represent standard deviations of stream width over the 10 h timelapse. (D) The average width of the 31 focal streams plotted as a function of time. (E) The average x-position of stream fluorescence linescan peaks plotted as a function of time. For D and E, error bars represent standard deviations of stream width between 31 microjet units in a device.

2.4.4 Micropatterning of myoblasts and myotubes in trenches

We found that native PDMS, due to its hydrophobicity, did not support protein (i.e. Matrigel) coatings for long-term (~2 week) cell culture (data not shown). Furthermore, even after oxygen plasma treatment, PDMS undergoes fast hydrophobic recovery within hours, and also did not support long-term cell viability [107]. To address this problem, we developed a method to selectively covalently modify the PDMS surface inside the trenches with a positive charge molecule to support Matrigel adhesion. We utilized a covalent grafting approach using an epoxy-silane, (3-glycidoxypropyl) trimethoxysilane (GPTMS), to modify PDMS surfaces [108, 109]. We applied a PDMS slab on top of the trenches by conformal contact to mask the outside zones such that only the trench would be hydrophilized by plasma oxidation, creating hydroxyl groups (Figure 2.2C and Figure 2.4). The silane groups on GPTMS covalently react and bond with the hydroxyl groups on PDMS, creating a surface of epoxide groups. The amine groups on poly-D-lysine or poly-ornithine react with the epoxide groups from GPTMS, forming a covalently bound layer of poly-D-lysine or poly-ornithine inside the trench surface. The positively charged layer of poly-D-lysine/poly-ornithine serves to improve protein adsorption and preserve protein biological activity [63], facilitating Matrigel coating within the trench. In contrast, in the zones outside of the trench, which were protected from plasma oxidation by the PDMS slab, we expected Pluronic F127 to adsorb to the untreated hydrophobic PDMS substrate and repel cell attachment. Pluronic forms a "brushlike" molecular conformation, in which the hydrophobic PPO blocks adsorb to the hydrophobic PDMS substrate and the hydrophilic PEO blocks face the solution, resisting protein adsorption by repulsive osmotic force, thereby minimizing cell adhesion [103, 110]. We found that this micropatterning scheme supported long-term culture of myotubes within trenches (Figure 2.8).

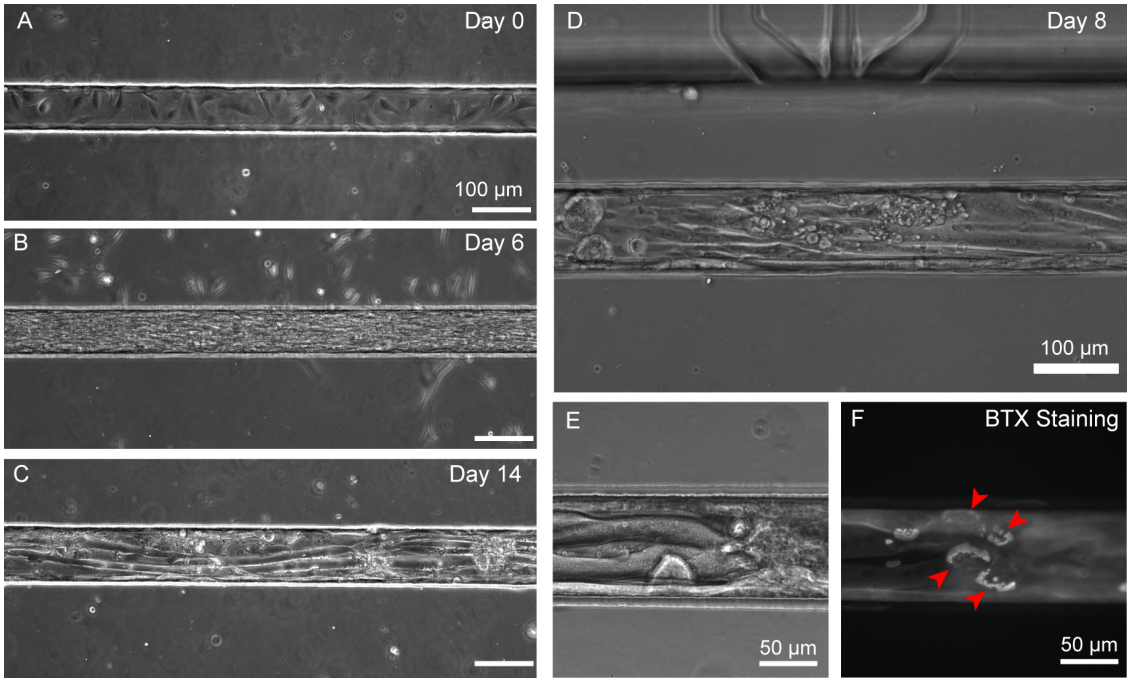

Figure 2.8: Long term cell culture and myoblast differentiation into myotubes.

(A) Day 0: One hour after cell seeding, C2C12 myoblasts are adhered and spread inside the Matrigel-coated PDMS trench. Very few cells attached on the outside of the trench, showing the effectiveness of the Pluronic F127 cell-repellant coating. Cells grew confluent and filled the trench by Day 3, during which the growth media was changed to differentiation media containing low serum (not shown). (B) At Day 6, 3 days after change to differentiation media, elongated fused myoblasts formed. (C) Day 14: Mature myotubes are shown within a 100 µm wide trench. Note that cells outside of the trench have died and detached. (D) On-chip differentiation of C2C12-derived myotubes at Day 9 showed their elongated, mature phenotype. (E) A high-magnification image shows elongated myotubes within a 100 µm wide trench and showing signs of maturation. (F) Myotubes expressing numerous AChR "pretzel" patterns when labeled with bungarotoxin-Alexa Fluor 488 (red arrows). Together, these results demonstrate the capability of micropatterning muscle cells and their capacity to differentiate and mature within the microfluidic chip.

Within one hour of cell seeding, C2C12 myoblasts attached inside the Matrigel-coated trenches, while a lower density of cells also adhered to the zones outside of the trenches. While bathed in growth media, myoblasts proliferated and spread within the trenches. When the cells became 80% confluent at Days 1 – 3, media was changed to low-serum differentiation media and myoblasts fused into myotubes, aligning with the

axis of the trenches (Figure 2.8 A-D). Usually, mature myotubes formed within 5 – 7 days after media change, both inside the trenches and on flat substrate controls. Mature myotubes could be maintained for several days thereafter, i.e. for at least 14 days after initial seeding. Moreover, we found that thinner trench dimensions of 15 – 20 μm width and 40 μm height allowed confinement of single myotubes, allowing for single cell manipulation (Figure 2.12). Meanwhile, over the first few days of culture, the cells outside of the trenches became rounded, died, and detached from the substrate. This observation may be attributed to two factors: 1) the Pluronic surface was sufficiently cell-repellant, and 2) the hydrophobicity of the outside zones prevented long-term cell adhesion, possibly through a cell-repelling mechanism due to the presence of bovine serum albumin in the media [111].

The microscale geometry of the open chamber (gap widths of 200 μm or 600 μm) necessitated that the protein micropatterning step be done prior to bonding of the cell patterning layer and the perfusion layer. Therefore, there was concern that the bonding of these two layers, which would expose the Matrigel-coated trenches to oxygen plasma, would cause denaturation of the protein coating. Surprisingly, we found no problems with cell adhesion and long-term viability after this step. We observed robust long-term myotube maturation, growth and expression of laminin-induced acetylcholine receptor cluster "pretzels" in intact devices (Figure 2.8E). These mature, elaborate AChR cluster pretzels which form independently in the absence of motor neuron signaling, indicate that laminin, which is present as 60% of Matrigel, is biologically active [23]. We hypothesize that there is a sufficiently thick Matrigel coating that remains active even if a superficial layer of Matrigel gets stripped or denatured from plasma treatment. Overall, these long-

term cell culture conditions allow for high-throughput microfluidic delivery of chemicals to cultured myotubes.

2.4.5 Focal delivery of soluble factors to myoblasts

We tested the focal delivery of a cytoplasmic live cell stain, calcein AM and a nucleic acid stain, Hoechst 33342 to micropatterned myoblasts (Figure 2.9). Under conditions of: focal flow rate = 100 μL/h, flanking flow rate = 400 μL/h, 1 psi negative pressure, a mixture of calcein AM cell tracer, Hoechst 33342, and BSA-Alexa Fluor 594 stream tracer was focally delivered to cells. Cell staining with calcein was observed within 10 minutes and Hoecht within 30 minutes. We observed that calcein AM staining of cell cytoplasms and Hoechst 33342 staining of cell nuclei were largely confined to the areas under the focal streams as indicated by the fluorescent BSA tracer. This localized staining was maintained for up to four hours.

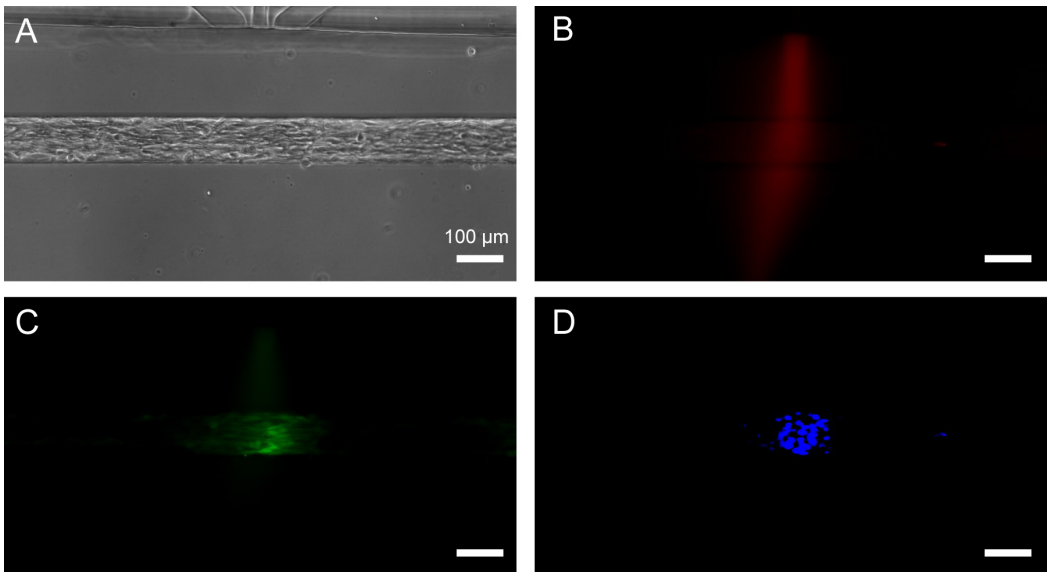

Figure 2.9: Focal delivery of soluble reagents to micropatterned cells.

(A) Brightfield images of C2C12 myoblasts in a trench (100 μm wide, 110 μm deep). (B) A fluorescent BSA-Alexa Fluor 594 tracer was also spiked into the solution in the focal channels track the focal stream. (C) Regio-selective calcein AM staining of C2C12 cells under the focal stream. (D) Regio-selective staining of nuclei by Hoechst 33342. (Focal flow rate = 100 μL/h, flanking flow rate = 400 μL/h).

2.4.6 Focal delivery of soluble factors to trapped myofibers

The open-chamber architecture of the microfluidic device allowed simple top-loading of cells, which enabled microfluidic manipulation of alternative cell culture models other than C2C12 cell lines. We altered our microfluidic device such that the cell patterning layer contained an array of 64 microwells to immobilize myofibers, which are used as a model system for understanding the growth, differentiation and migration of satellite cells within their intact niche microenvironment [104, 112-115]. FDB myofibers isolated from mouse hindlimbs were viable and stained positively for myosin heavy chain 48 hours after dissection and immobilization in the microfluidic device (Figure 2.13). Myofibers showed striations and multiple cell nuclei and some satellite cells on their surfaces (Figure 2.10A). As a proof-of-concept experiment to show localized soluble factor delivery, we applied focal streams of Hoechst DNA to locally label nuclei in myofibers. We observed a gradient pattern of myonuclei/satellite cell nuclei staining along the lengths of the myofibers using Hoechst 33258 as seen in Figure 2.10C. In contrast, nuclei on myofibers simply bathed in a solution of Hoechst 33258 were homogeneously stained. The gradient of nuclei staining intensity indicated that different myonuclei along the myofiber length were receiving different local concentrations of the soluble factor. DNA fluorescence staining intensity is sensitive to the delivered Hoechst dye concentrations from 0.01 μg/mL to 1 μg/mL. We expected that the local concentrations varied from the highest possible level of 5 μg/mL in the center of the focal

stream to 0.01 µg/mL on the periphery of the stream. The spatial profile of the nuclei staining intensities followed the exponential distribution pattern seen in the BSA stream and myoblast cell staining patterns (Figure 2.10D).

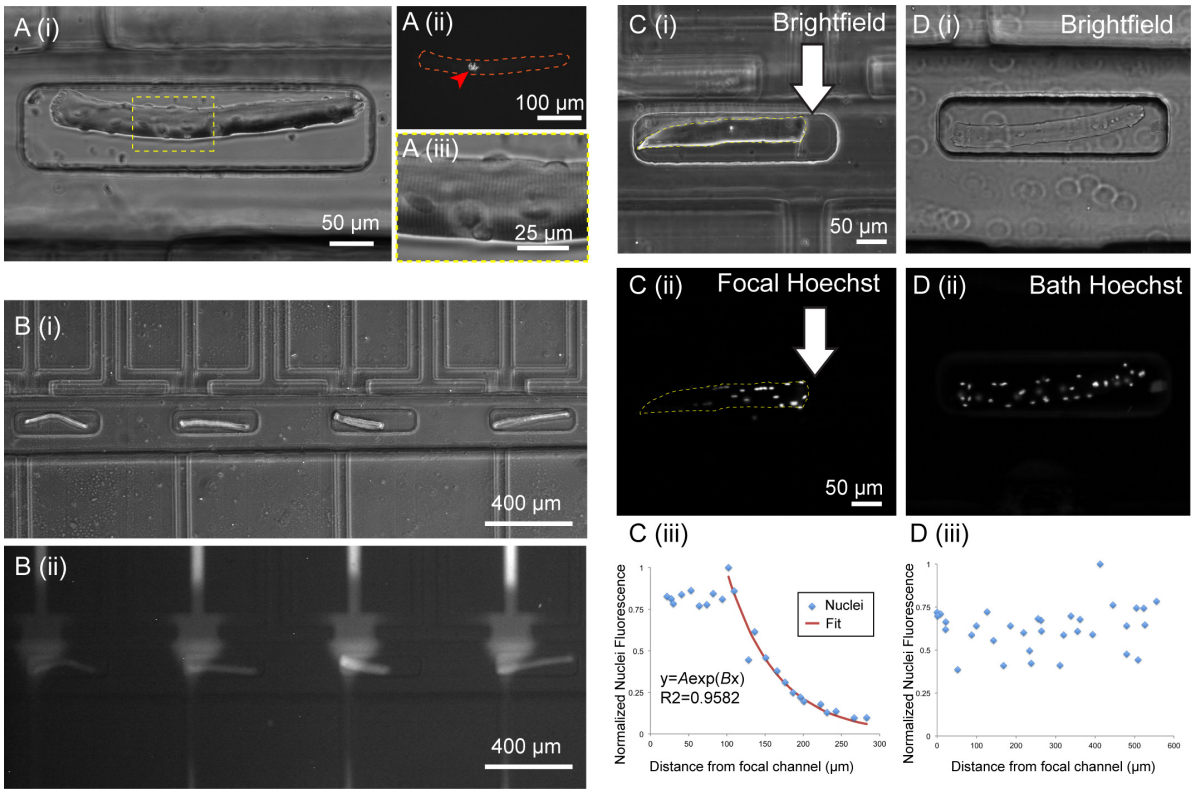

Figure 2.10: Focal delivery of DNA stain to nuclei in trapped myofibers.

(A-i) Brightfield image of a FDB muscle fiber trapped inside a microwell. (A-ii) The orange outline shows the same myofiber with a red arrow pointing to bungarotoxin-Alexa Fluor-488-stained AChR cluster signifying the synapse. (A-iii) An inset shows the muscle fiber striations and myonuclei. (B) The myofiber culture system can be scaled up to 64 microwells per device. (B-ii) BSA-Alexa Fluor 594 was applied focally to one side of the myofibers, generating gradients within single myofibers. Note that the flow profiles are different from the myotubes device due to the different channel configuration in the myofiber device design. (C) We investigated the generation of gradients within single myofibers by applying Hoechst 33258 live nuclear stain in the focal channels of the microfluidic device. In the top panel, myonuclei and nuclei of surface-lying satellite cells were selectively stained on the right side of the myofiber where the focal stream was applied. There is a gradient of decreasing nuclear staining intensity from right to left. Data was fitted to an exponential function of the form y = A exp (Bx), where A and B

were constants with values of A = 4.503, B = -0.01529, and R-square=0.9582. Note that the points within the first 100 μm were discarded because there was a maximum intensity value within the ROI that reached saturation. (D-i-iii) In the bottom panel, a bath of Hoechst nuclear stain was applied and we saw uniform nuclei staining as expected. From N=5 myofibers that were focally targeted with Hoechst dye, we see a distance dependence of myonuclei staining fluorescence intensity with respect to the source focal channel (data in supplementary materials).

2.5 CONCLUSIONS

We have developed a microfluidic platform for the focal delivery of soluble factors to micropatterned cells that operates within an open architecture. In the open format, cells can be seeded, cultured, and differentiated with the straightforward ease of a conventional petri dish. The device operates on the principle of hydrodynamic focusing, with the ability to generate focused streams (36 – 187 μm wide) in the open space. Cells and muscle fibers can be confined within trench or trap geometries, respectively, that allow precise interrogation and provide physiological mimicry. We demonstrated focal delivery of calcein AM dye focal delivery to cells. Furthermore, we showed focal delivery of Hoechst DNA stain locally to myonuclei on myofibers. The intensity of nuclei staining showed a gradient pattern along the length of the myofiber, reflective of the variation in local dye concentration created by the focal stream. The trenches can be selectively micropatterned with a PDMS epoxy-silane covalent modification method that facilitates long-term cell culture and differentiation on-chip. We envision that this microfluidic device will enable precise, high-throughput studies of a multitude of muscle biology questions.

Ultimately, our goal was to apply this flow-focusing microfluidic platform in studying AChR dynamics in an *in vitro* model of NMJ synaptogenesis, effectively

replacing the motor neuron with a focal stream of agrin delivered to subcellular portions of micropatterned myotubes. In these efforts, we faced challenges with: 1) myotube viability, 2) imaging of AChR clusters, and 3) relatively low throughput. 1) Although myotubes were successfully confined into trenches, we sometimes observed low myotube viability, especially during live cell experiments. It is possible that cells face toxicity from GPTMS surface modifications, although this has not been confirmed. 2) When myotubes were packed inside of a trench, especially in wider trenches (~ 100 μm wide, 110 μm high), there were often multiple layers of myotubes, rendering many AChR clusters out of focus. As a solution, we utilized thinner trenches, (~ 35 μm wide, 40 μm high), but saw low cell viability, especially in the interior of the trenches (i.e. several millimeters from the trench ends). We attribute this to non-optimal hydrophilization of the thinner trenches with oxygen plasma, which may require a higher plasma dose. 3) The 32 unit device configuration was relatively low-throughput, as the incidence of a pre-existing AChR pretzel cluster coinciding with a focal stream was rare. Future studies will need to optimize the plasma hydrophilization conditions for thinner trenches, i.e. 20 to 35 μm. To address many of these shortcomings, we developed a membrane-based focal delivery system, discussed in **Chapter 4**.

2.6 SUPPLEMENTARY FIGURES

Table 2.1: Photolithography protocol for master molds: flow-focusing device

	Layer	Thickness	Photoresist	Spin Coat	Soft Bake	UV Exposure	Post exposure Bake	Develop	Hard Bake
Master I (Cell Patterning Layer)		110 μm	SU-8 2075	2000 rpm for 40 s	15 min @ 65°C, 30 min @ 95°C, 100°C/h (3x)	264 mJ/cm^2	15 min @ 65°C, 30 min @ 95°C, 100°C/h	60 min	60 min @ 200°C, 100°C/h
Master II (Perfusion Layer)	**Layer A (Alignment Marks)**	2 μm	SU-8 2002	3000 rpm for 30 s	1 min @ 95°C, 100°C/h	80 mJ/cm^2	2 min @ 95°C, 100°C/h	3 min	60 min @ 200°C, 100°C/h
	Layer B (Microjets Layer)	20 μm	SU-8 2015	2125 rpm for 40 s	12 min @ 95°C, 100°C/h	159 mJ/cm^2	15 min @ 95°C, 100°C/h	\	\
	Layer C (Channels Layer)	50 μm	SU-8 2035	2300 rpm for 40 s	9 min @ 65°C, 27 min @ 95°C, 100°C/h	216 mJ/cm^2	6 min @ 65°C, 21 min @ 95°C, 100°C/h	\	\
	Layer D (Exclusion molded Layer)	330 μm	SU-8 2075	2000 rpm for 40 s (3x)	15 min @ 65°C, 30 min @ 95°C, 100°C/h (3x)	487 mJ/cm^2	15 min @ 65°C, 90 min @ 95°C, 100°C/h	60 min	60 min @ 200°C, 100°C/h
Master III (Ports Layer)		110 μm	SU-8 2075	2000 rpm for 40 s	15 min @ 65°C, 30 min @ 95°C, 100°C/h (3x)	264 mJ/cm^2	15 min @ 65°C, 30 min @ 95°C, 100°C/h	60 min	60 min @ 200°C, 100°C/h

* Note that thickness denotes thickness of a single layer, not cumulative thickness

Table 2.2: Stream widths with varying flow conditions: 600 µm gap width

k	Focal Flow Rate (µL/h)	Flanking Flow Rate (µL/h)	Stream Width (µm)
12	100	1200	71 ± 6
8	100	800	74 ± 4
4	100	400	87 ± 6
2	100	200	112 ± 13
1	100	100	137 ± 21
0.5	100	50	161 ± 21
0.25	100	25	187 ± 17

Table 2.3: Stream widths with varying flow conditions: 200 µm gap width

k	Focal Flow Rate (µL/h)	Flanking Flow Rate (µL/h)	Stream Width (µm)
20	100	2000	36
9	100	900	39
4	100	400	58
2	100	200	68
1	100	100	75

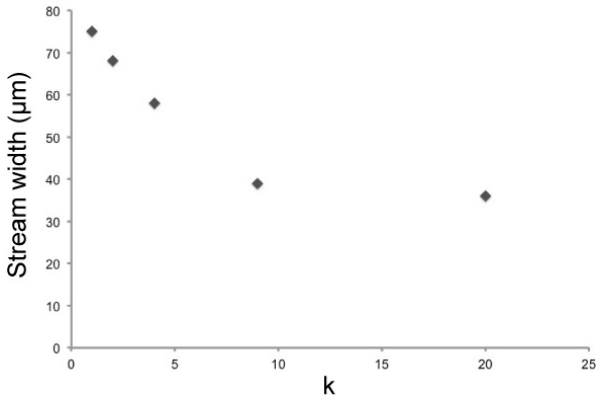

Figure 2.11: Characterization of stream widths with respect to flow rates in 200 µm open chamber gap device.

k = flanking/focal flow rate ratio. k was plotted against the stream width. A rational function was fitted to the points. We see an inverse relationships between the k and the stream widths, as expected.

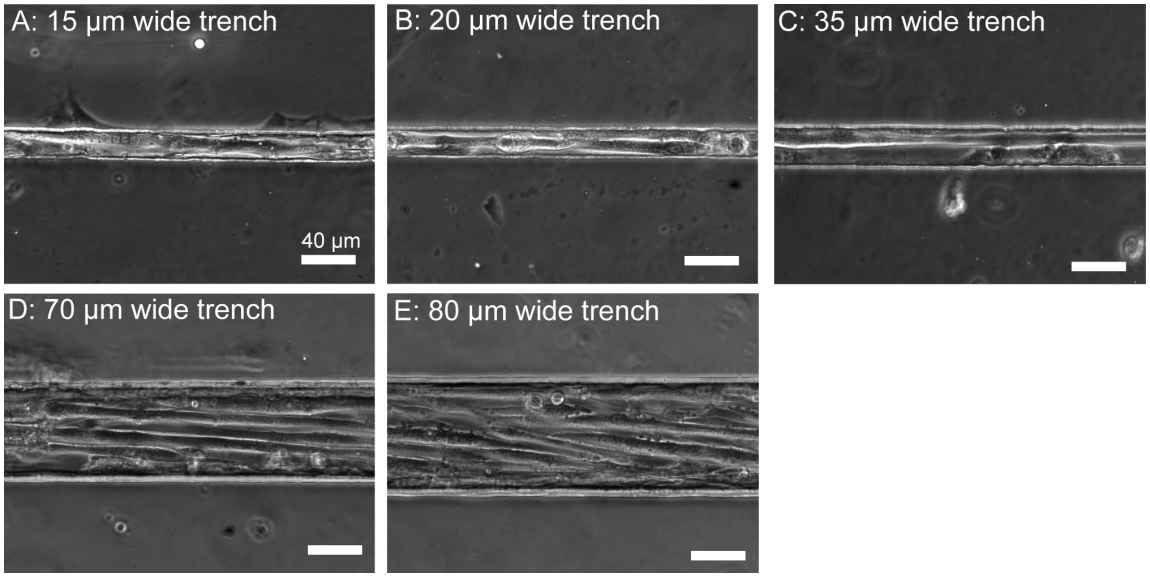

Figure 2.12: Trench dimensions affect myotube micropatterning.

C2C12-derived myotubes at Day 7 in trenches of varying widths from 15 µm to 80 µm. Trenches as thin as 15 to 20 µm constrain single myotubes. Note the absence of cells outside of the trenches, showing the effectiveness of the micropatterning method.

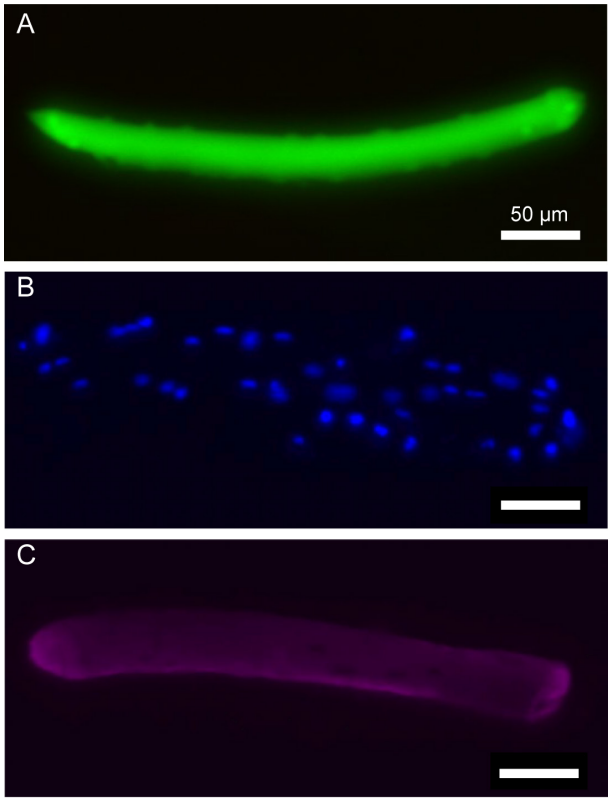

Figure 2.13: Myofiber immuno-fluorescence staining.

(A) Calcein (live) and ethidium homodimer (dead) cell staining of a whole myofiber. We see few dead cells, indicating high viability. (B) DAPI staining of myonuclei. (C) Fast skeletal myosin heavy chain staining.

Focal Hoechst Application

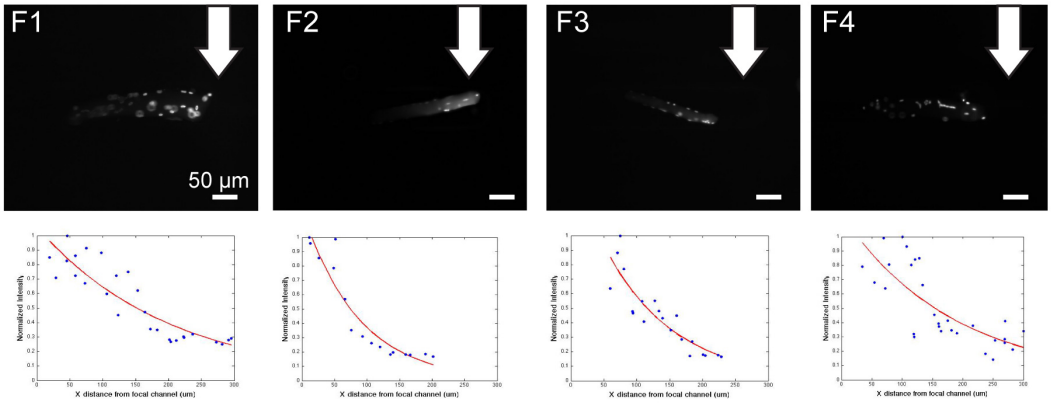

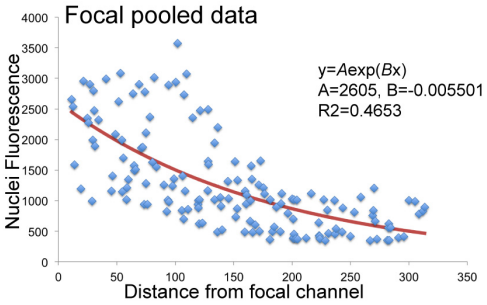

Myofiber	B	R-square
F1	-0.00494	0.7954
F2	-0.01173	0.8925
F3	-0.01239	0.7896
F4	-0.00742	0.5926

Bath Hoechst Application

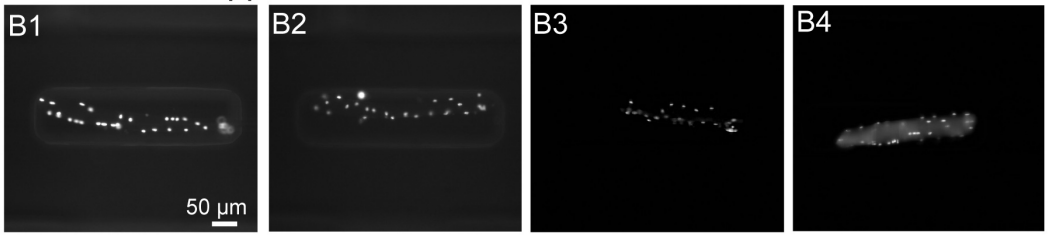

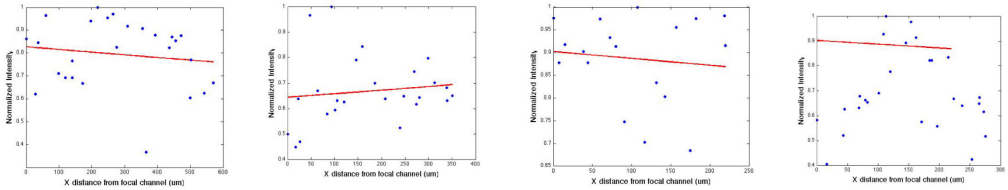

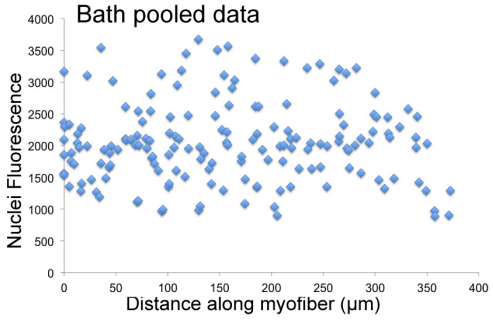

Myofiber	B	R-square
B1	-0.0001463	0.0198
B2	0.0002097	0.0152
B3	-0.00017	0.0114
B4	5.62E-05	4.73E-04

Figure 2.14: Fluorescence (DAPI channel) images of Hoechst-stained nuclei.

White arrows show the focal channel mouth. The intensity profiles of individual myofibers are shown in focal (F) and bath (B) Hoechst 33258 application. Data was fitted to an exponential decay function of the form $y = A\exp(Bx)$. The data was also pooled together to give a composite distribution of distance from focal channel versus absolute intensity. The tables show the decay constant B and the R-square values for the fits. Note that the R-square values (correlation) are much higher in the focal application versus bath.

CHAPTER 3: FLUOROSILANE-BASED CELL MICROPATTERNING

3.1 SUMMARY

We developed a novel cell micropatterning technique based on the principle of creating alternating hydrophilic cell adhesive and hydrophobic cell repellant microtracks. The method involves: 1) blanketing a substrate with hydrophobic silane, 2) selectively etching the fluorosilane into hydrophilic tracks using a PDMS micropatterning template, 3) coating the tracks with Matrigel to render it cell-adhesive, and 4) filling the background regions with Pluronic, creating cell repellant regions. The method is technically facile (taking ~2 hours to fabricate) and versatile for common cell culture substrates such as glass. We generated high-resolution micropatterns of hundreds of parallel myotubes within a few square centimeters for high throughput experiments.

3.2 INTRODUCTION

In parallel with our efforts on the open-chamber flow-focusing device, we looked to alternative membrane-based focal delivery designs that would provide higher throughput and be more user-friendly. We envisioned a device with large 2D arrays of micropatterned myotubes that could be individually addressed by fluidic apertures (**Chapter 4**). Therefore, we needed a method for patterning large arrays of myotubes on 2D culture surfaces. In our system, micropatterned myotubes could be easily tracked and monitored with timelapse microscopy, while avoiding confounding factors from neighboring cells. Furthermore, micropatterning of myotubes provides a physiological mimic of the highly aligned anisotropic *in vivo* architecture of skeletal muscle [116].

When organized in micropatterns, C2C12 cells show optimal fusion, maturation, and response to electrical pulse stimulation [117]. Myoblasts can sense microscale chemical or topographical cues, which guide their orientation, guidance, and direction of fusion [118]. Motivated by the needs to automate microscopy acquisitions and provide physiological mimicry, we aimed to develop a facile micropatterning strategy adaptable to porous PET membrane substrates.

Cell micropatterning schemes largely follow one of two strategies: 1) selective cell attachment is guided by preferential adhesion to favorable versus unfavorable substrate compositions, or 2) cell attachment to a homogeneous substrate is blocked in some areas by a physical barrier [49, 119]. We chose the first approach, a strategy that is similar in principle to that of Tourovskaia et al. [63, 120]: deposit a blanket layer of cell-repellant background, selectively remove the cell-repellant material using etching through microchannels of a PDMS mask, and then finally selectively adsorb matrix protein through the microchannels to generate cell-adhesive microtracks (Figure 3.1). Since the chemical grafting of an interpenetrating polymer network (IPN) is specific to glass surface chemistries and is a labor-intensive a process that takes ~9-10 hours [64, 120, 121], we developed a simpler, more versatile fabrication approach adapted for a variety of substrates, including PET membranes and glass.

3.3 Materials and Methods

3.3.1 Fabrication of master molds and replica molding

For photolithography of the master for the micropatterning template, an adhesion-promoting 13 μm thick base layer of SU-8 2015 was spin-coated at 4000 RPM, and UV

exposed at 132 mJ/cm^2. Subsequently, a 40 μm thick layer defining the micropatterned cell tracks was spin-coated using SU-8 2035 at 3300 RPM, UV exposed at 164 mJ/cm^2, post exposure baked, developed for 30 minutes, and hard baked at 150°C. Prior to PDMS molding, masters were passivated in vacuum desiccator with trichloro(1H,1H,2H,2H-perfluorooctyl)silane (#448931, Sigma-Aldrich) to assist PDMS replica release. The micropatterning template was replica molded by pouring 5 mL of 10:1 ratio of PDMS elastomer base to curing agent onto its master mold and curing at room temperature for 48 hours. Room temperature curing minimized PDMS shrinkage, which ensured accurate registration of the micropatterns to the apertures.

3.3.2 Fabrication of micropatterns

The micropatterning scheme is shown in Figure 3.1. The substrate (e.g. PET membrane or glass) was first treated with oxygen plasma to facilitate silane deposition, then rendered hydrophobic by vapor deposition of a fluorosilane, trichloro(1H,1H,2H,2H-perfluorooctyl)silane in a vacuum desiccator. A few drops (~ 500 μL) of fluorosilane were added to lint-free wipes (Berkshire, Pro-Wipe #PW.880.0810.12) at the bottom of the vacuum desiccator chamber and vacuum was applied for 1 h. Next, a PDMS template containing microchannels (40 μm wide and 40 μm high, 14 mm long, separated by 120 μm) was aligned under a dissection microscope (Nikon SMZ 1500) such that channels were in direct registration over the apertures, and placed in conformal contact with the PET membrane. Oxygen plasma (60 W, 670 mTorr, 60 seconds) was used to etch the fluorosilane surface into patterns of cell-adhesive hydrophilic tracks, while the regions in contact with PDMS were protected. After plasma, areas exposed under the channels were infused with dilute Matrigel (#356234, BD Biosciences, San Jose, CA) (1:50 dilution from stock in DMEM) or fibronectin (50

μg/mL in PBS) by vacuum suction with a P-100 micropipette tip. The Matrigel patterns were allowed to polymerize inside the microchannels in a 37°C incubator for 30 minutes, and then dried for at least 4 hours at room temperature in a laminar flow hood. Subsequently, the PDMS template was removed, and the surface was incubated with 0.2% Pluronic-F127 (#P3000MP, Life Technologies, Carlsbad, CA) in D-PBS (#14190250, Life Technologies), which adsorbed to the remaining fluorosilane, creating background cell-repellant regions.

3.3.3 Cell culture

Cells selectively attached to the Matrigel-patterned regions, and then were induced to fuse into myotubes by changing from growth media within 24 hours of seeding (DMEM, 20% fetal bovine serum, 1% pencillin/streptomycin) to growth factor-depleted differentiation media (DMEM, 2% horse serum, 1% pencillin/streptomycin). C2C12 cells readily attached, proliferated, and fused into myotubes in differentiation medium within days 6-7 on Matrigel-coated modified Transwell devices. To assess their maturation, myotubes were visualized using immunofluorescence microscopy in DAPI (#D1306, Life Technologies) to demonstrate their multi-nucleated state, and phalloidin-Alexa Fluor 488 (#A12379, Life Technologies) to show the filamentous actin cytoskeleton. Briefly, cells were washed with PBS and fixed in 4% paraformaldehyde in PBS at room temperature for 10 minutes, followed by permeabilization using 0.1% Triton-X100 in PBS for 10 minutes at room temperature, staining with 50 μg/mL phalloidin-Alexa Fluor 488 and 250 nM DAPI, and imaged using an epifluorescence microscope.

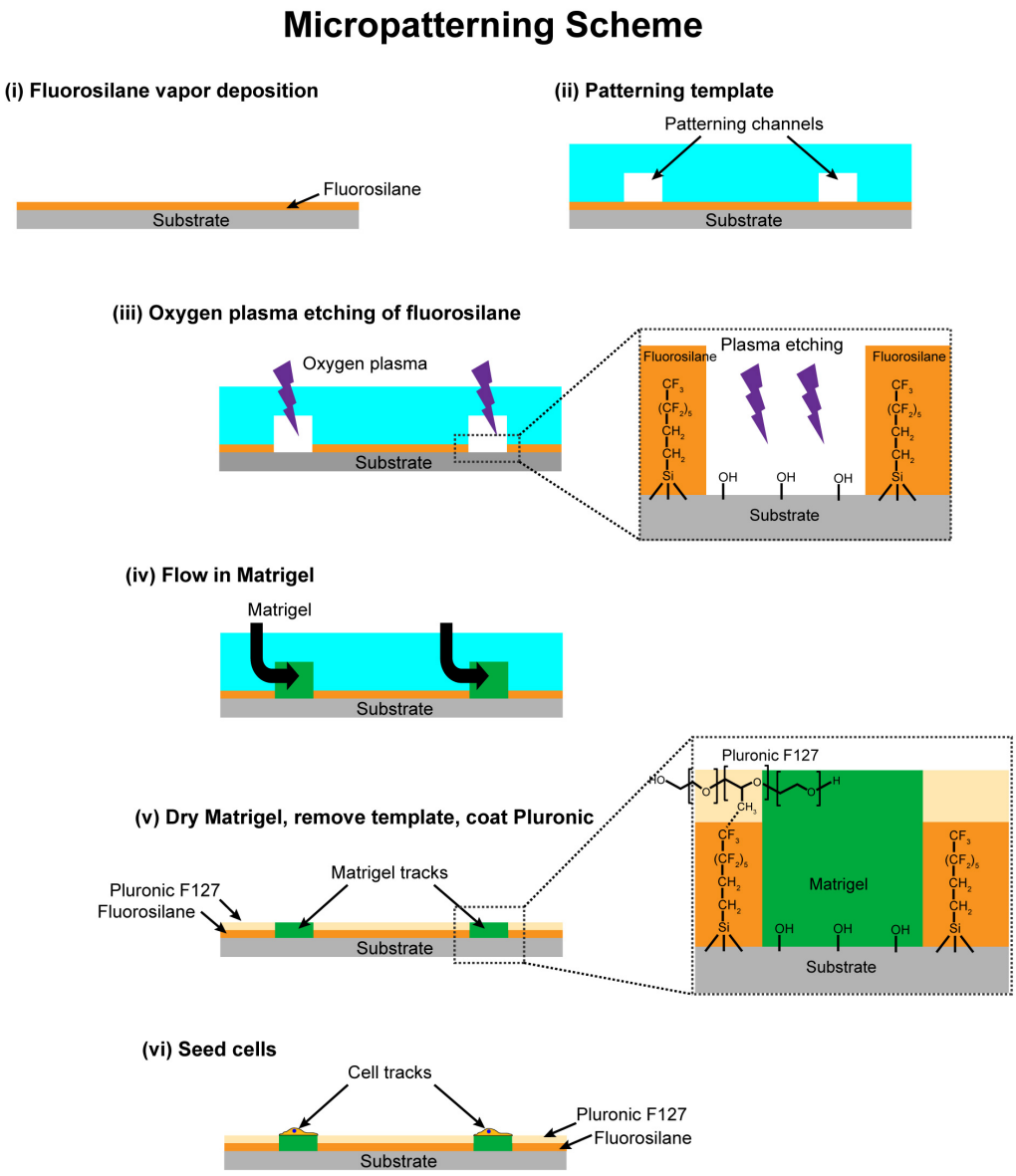

Figure 3.1: Fluorosilane-based micropatterning scheme.

(i) The native substrate is homogeneously coated with fluorosilane. (ii) A PDMS patterning template with microchannels is aligned in registration with apertures (or more generally, on any substrate) and (iii) oxygen plasma is applied to etch fluorosilane into hydrophilic tracks. (iv) The microchannels are filled with Matrigel, creating cell-adhesive tracks. (v) Pluronic, a cell repellant, is physisorbed onto the hydrophobic regions. (vi) Cells are seeded and selectively adhere to the Matrigel lanes.

3.3.4 Comparison of micropatterning method on glass, TCPS, and PDMS

To demonstrate the versatility of the method for other common cell culture substrates, a similar method was applied to micropatterning borosilicate glass coverslips, tissue culture polystyrene (TCPS), and PDMS. For glass substrates, coverslips (Gold Seal Cover Glass #3335) were cleaned in Contrad 70 detergent for 2 hours, dried with nitrogen gas, and dried in a 70°C oven. Treated sterile tissue culture polystyrene petri dishes (Corning #430293) were used for the TCPS substrates. PDMS substrates were prepared by curing of 10:1 PDMS base : curing agent inside of 100 mm petri dishes, and sterilization under a UV lamp. The same micropatterning steps were used: 1) initial plasma oxidation of the substrate, 2) fluorosilane vapor deposition, 3) placement of PDMS patterning template in conformal contact to the substrate, 4) spatially selective plasma etching of the fluorosilane in microtracks, 5) Matrigel filling of the tracks and drying, and 6) Pluronic backfilling of the cell-repellant background.

To determine the necessity and sufficiency of the steps in the micropatterning method, we assessed cell attachment under various conditions with and without each of the steps (Table 3.2). Samples for these experiments consisted of PET membranes bonded to PDMS slabs. Samples were assessed for cell attachment by labeling cells with nuclear dye Hoechst 33342 (5 μg/mL) and counting cell nuclei.

3.3.5 Contact angle measurements

Contact angle measurements were made with an FTA 200 Dynamic Contact Angle Analyzer to assess the wettability of substrates at various stages of the micropatterning method. Dynamic advancing contact angles were measured using deionized water at a flow rate of 0.3 μL/s. Three contact angle measurements were made per sample, and the mean and standard deviations were recorded.

3.3.6 ToF-SIMS analysis

Samples for ToF-SIMS were prepared using the same micropatterning protocol described in Section 3.3.2. Silicon wafers (1 x 1 cm^2, Silicon Quest Intl., Santa Clara, CA) cleaned by sequential sonication in DI water, dichloromethane, acetone, and methanol were used as model substrates to avoid confounding factors for ToF-SIMS, i.e. impurities from salts such as potassium chloride in borosilicate glass, and topographical unevenness in porous membranes. ToF-SIMS acquisition was performed using an ION-TOF 5-100 (ION-TOF GmbH, Münster, Germany) with "mass filtered" 25keV Bi_3^+ liquid-metal primary ion source, which hit the target at an angle of 45°. Charge compensation was achieved with a pulsed, low-current electron gun. A Bi_3^+ pulsed bunched primary ion beam with a typical current of 0.08 – 0.1 pA was used to acquire positive and negative secondary ion images and spectra. Target currents were measured before each data set using a Faraday cup. Analysis using a Bi_3^+ dose of 4.77×10^{10} ions/cm^2 was used to acquire spectra (256 x 256 pixels) and rastered over a 300 × 300 μm^2 area. The mass resolution ($m/\Delta m$) for positive polarity spectra was roughly 4200 and 4500 at $C_2H_3^+$ (m/z 27), negative polarity $m/\Delta m$ ranged from 3800 to 4200 at C_2H^- (m/z 25). Positive spectra were calibrated to CH_3^+, $C_2H_3^+$, and $C_3H_6^+$, negative spectra were calibrated to O^-, OH^-, and C_2H^-. For final analysis all images were binned by 4 pixels resulting in a 128 x 128 pixel image.

3.4 Results and Discussion

We developed a fluorosilane micropatterning scheme based on the microscale control of differential wettability between cell-adhesive and cell-repellant regions. Trichloro(1H,1H,2H,2H-perfluorooctyl)silane is a hydrophobic fluorosilane commonly

used to passivate silicon wafers to aid in release of PDMS replica molds. Under typical conditions, i.e. 1 hour inside a vacuum chamber at 0.35 bar, vapor deposition of fluorosilane generates a hydrophobic film ~40 nm thick [122]. Plasma etching (ashing), commonly used in stripping >1 μm thick photoresists in the microelectronics industry, has been previously used to remove organosilanes and polymeric interpenetrating PEG networks in micropatterning techniques [120, 123]. Our strategy was to homogeneously blanket a hydrophobic fluorosilane film onto the substrate, apply a PDMS template containing micropatterns, selectively plasma etch hydrophilic microtracks for cell adhesion, coat the hydrophilic tracks with matrix proteins, and backfill the remaining fluorosilane regions with cell-repellant co-polymer.

3.4.1 Cell adhesion and long-term pattern fidelity

C2C12 myoblasts selectively adhered to the micropatterns within 1 hour of seeding and fused into myotubes within 7 days after changing to low-serum media (Figure 3.2A). Patterns remained in high fidelity for at least 2 weeks, beyond which observations were not made. Myotubes showed highly aligned F-actin fibers with phalloidin-FITC staining, multiple nuclei with DAPI staining (Figure 3.2A), aneural AChR "pretzel" clusters on the myotube basal side by labeling with bungarotoxin-Alexa Fluor-594 conjugate (see **Chapter 5** for detailed results), and spontaneous twitching. The micropatterning method is simple and time efficient (all steps up to Matrigel drying take a total ~ 2 hours). Another advantage of this method is the versatility of micropatterning geometry and location, which can be easily aligned with micro-features on the device (e.g. underlying apertures and microchannels) with the aid of a stereo-microscope. We have found that myotubes mostly stay within their tracks when separated by 120 μm or

more. At separation distances of 80 μm and smaller, myotubes may "bridge" into the next cell track (data not shown).

3.4.2 Adaptability of micropatterning method to other substrates

We assessed the adaptability of the micropatterning method to other common cell culture substrates, such as glass, tissue culture polystyrene (TCPS), and PDMS (Figure 3.2B). All substrates underwent the same type of chemical treatment as shown in Figure 3.1 to create Matrigel microtracks. On day 1 after seeding, we observed formation of cell micropatterns on glass and PDMS substrates, but homogeneous cell attachment on TCPS. On days 4 – 6, we observed cells detaching on PDMS substrates, while robust micropatterns remained on glass for long culture periods over 7 days. We surmise that PDMS undergoes hydrophobic recovery from the initial plasma hydrophilization, resulting in desorption of cell-adhesive proteins and cell detachment and death. For long-term culture, alternative strategies to covalently modify PDMS may be necessary for adaptation of this micropatterning method [107, 108, 124].

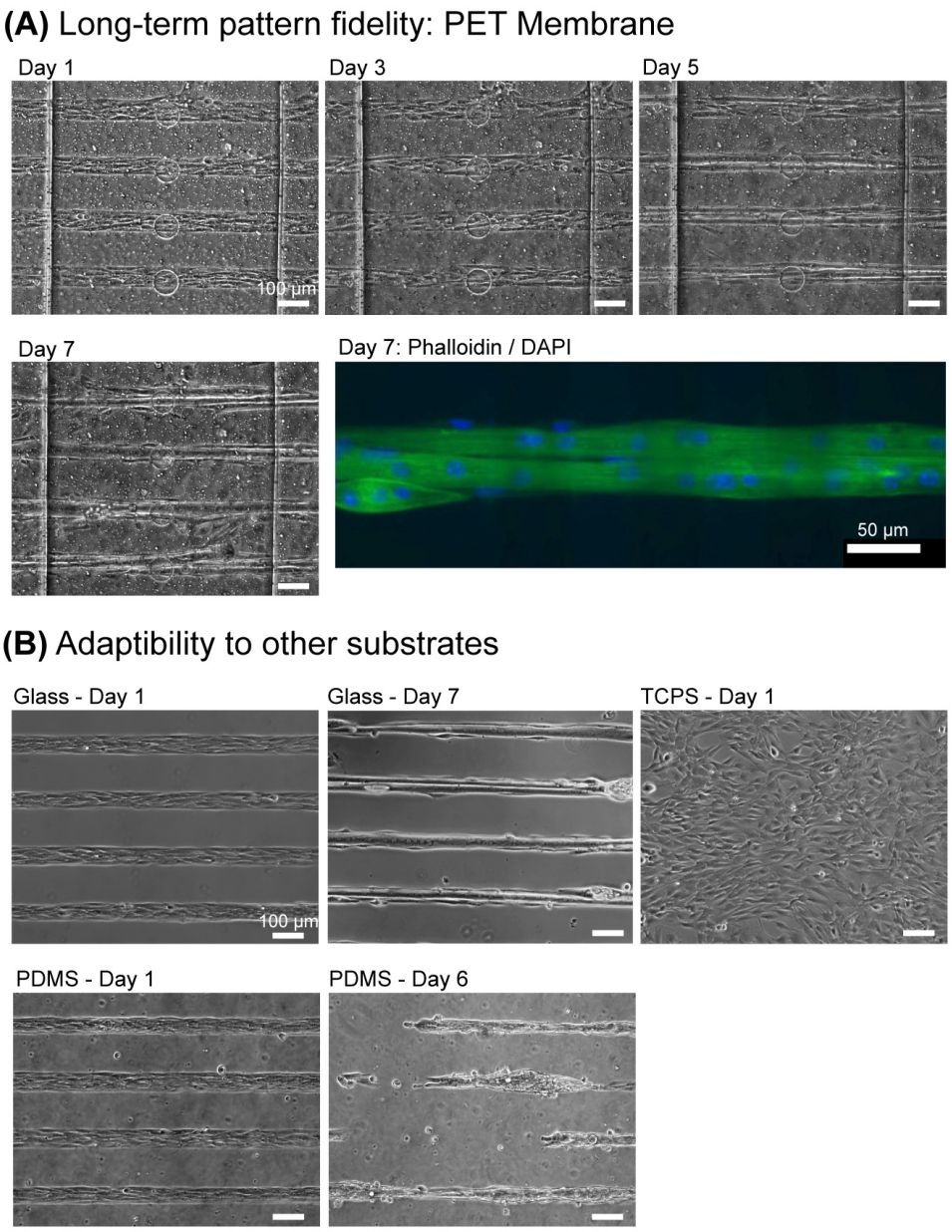

Figure 3.2: Cell-adhesion, long-term stability, and adaptability to various substrates using fluorosilane micropatterning method.

(A) C2C12 myoblasts form 40 µm micropatterns overlying 40 µm apertures at days 1, 3, 5, 7. Note that the myoblasts fuse into myotubes along the patterns. (B) Adaptability of fluorosilane micropatterning method to glass, TCPS, and PDMS: on glass, myoblasts micropatterns formed and fused into myotubes from days 1 to day 7. On TCPS, no micropatterns formed. On PDMS, micropatterns formed initially, but cells detached at day 6.

3.4.3 Contact angle measurements

To further investigate the micropatterning mechanism, we first assessed the control of wettability of various bulk cell culture substrates from fluorosilanization and subsequent oxygen plasma etching. The contact angles of 0.1 μm microporous PET membranes, borosilicate glass coverslips, PDMS, and TCPS in 1) their native state, 2) after fluorosilane vapor deposition, and 3) after plasma etching following silanization, were measured. As expected, all substrates were rendered hydrophobic after fluorosilane deposition, and all became more hydrophilic, even relative to the native substrates, after oxygen plasma treatment (Table 3.1). Previously, cell culture substrates rendered hydrophilic from oxygen plasma treatment have been reported to promote Matrigel adsorption and increase cell attachment [125, 126]. Furthermore, Pluronic F127 favorably adsorbs onto hydrophobic surfaces with advancing contact angles greater than 80° and optimally at 98° [102, 103]. Pluronic F127 is a triblock copolymer of poly(ethylene oxide) (PEO) and poly(propylene oxide) (PPO) in a configuration of $(PEO)_{100}$-$(PPO)_{70}$-$(PEO)_{100}$. On hydrophobic surfaces, Pluronic forms a "brushlike" molecular conformation, in which the PPO blocks adsorb to the substrate and the PEO blocks face the solution, resisting protein adsorption by repulsive osmotic force, thereby minimizing cell adhesion [103, 110, 127]. Therefore, we predict that tuning the wettability of the cell adhesive tracks hydrophilic and the cell repellant regions hydrophobic optimized the adsorption of key molecules, Matrigel and Pluronic, which promoted and prevented cell adhesion, respectively.

Table 3.1: Contact angle measurements: fluorosilane etching

Substrate	Native	Fluorosilanized	Etched
Porous PET Membrane (1 μm)	77.8 ± 1.2	110.0 ± 0.6	21.1 ± 5.2
Glass	79.7 ± 7.0	104.2 ± 3.2	13.9 ± 3.5
PDMS	110.4 ± 2.6	107.3 ± 3.4	42.8 ± 22.4
TCPS	81.5 ± 8.1	100.7 ± 7.7	56.4 ± 12.4

3.4.4 ToF-SIMS surface analysis

Time-of-flight secondary ion mass spectrometry (ToF-SIMS) was used to create spatial maps of surface chemical compositions at various stages of the micropatterning method. ToF-SIMS was used to characterize: 1) etched micropatterns within a fluorosilane background, and 2) Matrigel microtracks with a Pluronic/fluorosilane background. ToF-SIMS was used to determine the characteristic chemical species present and ascertain: removal of fluorosilane, PDMS-substrate contact, localization of protein (Matrigel) in micropatterns, and localization of Pluronic F127 adsorption.

In the first ToF-SIMS experiment, silicon substrates were homogeneously coated with fluorosilane, a PDMS patterning template with 40 μm wide microchannels separated by 120 μm was brought into conformal contact, and oxygen plasma at 670 mTorr, 60 W, 60 s was applied to selectively etch the tracks. To determine the effectiveness of etching of the fluorosilane, we identified F_2H^- (m/z = 39.00) negative fragments in the cell repellant 120 μm regions. There was a distinct difference in F_2H^- intensity between the cell adhesive regions (low to no intensity) and the cell repellant regions (high intensity) (Figure 3.3A). Linescans of the F_2H^- fragment taken orthogonally to the track axes showed a sharp stepwise pattern resulting from the plasma etching (Figure 3.3B). However, there was a visible gradient of fluorosilane etching from the open end of the

patterning template towards the interior, as shown by the intensity differences of F_2H^- in the left (green solid line) and right (blue dotted line) regions of interest in Figure 3.3A and B. In the far interior of the micropattern, i.e. 4 to 7 mm from the template microchannel openings, there was less contrast in F_2H^- intensity between the etched and non-etched fluorosilane regions (image not shown), indicating diffusion-limited penetration of plasma ions. However, as shown in the next section, this gradient in etching efficiency along the tracks axis did not affect cell attachment, as cells were homogeneously attached throughout the Matrigel-coated microtracks. We further confirmed that regions in contact with PDMS were protected from plasma etching: the F_2H^- pattern and $SiC_3H_9^+$ (m/z = 73.06) positive fragments indicative of PDMS oligomers were detected only in the cell repellant regions (image not shown) [128, 129].

In the second SIMS experiment, silicon substrates were treated the same way as in the first SIMS sample set, but with the additional steps of Matrigel and Pluronic background coating, respectively. Positive ToF-SIMS fragments confirmed the spatial localization of $C_4H_8N^+$ within the cell adhesive microtracks, confirming the localization of Matrigel (Figure 3.3D). $C_4H_8N^+$ is a characteristic amino acid fragment generated from isoleucine, leucine, proline, valine, lysine, and arginine [130-132]. ToF-SIMS also identified C_3HO^+ (m/z = 53.00) and $C_4H_7O_2^+$ (m/z = 87.04) as previously reported Pluronic F127 fragments in the cell repellant regions within in the same dataset (Figure 3.3E) [133, 134]. The overlay image shows a distinct spatial separation of the protein fragment (green) in the cell adhesive microtracks and Pluronic fragments (red) in the cell repellant background regions (Figure 3.3F).

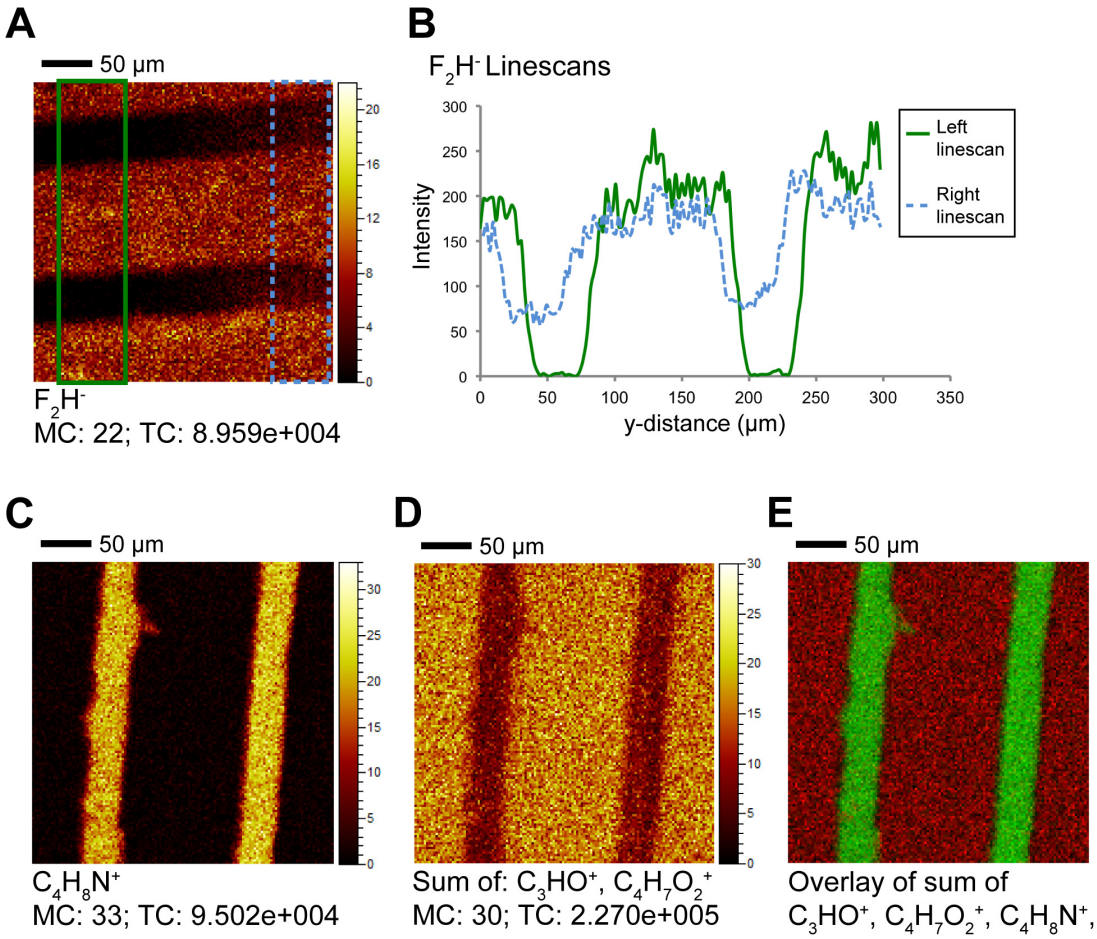

Figure 3.3: ToF-SIMS analysis of micropatterned surfaces.

(A) F_2H^- corresponding to fluorosilane shows localized etching in the microtracks. (B) Area intensity linescans of the left and right regions of interest in image (A) in the y-direction (origin at top of image) shows stepwise presence of silane. (C) $C_4H_8N^+$ shows localization of protein (Matrigel) in the microtracks. (D) A sum of two fragments, C_3HO^+ and $C_4H_7O_2^+$ shows localization of Pluronic-F127 on the cell-repellant regions. (E) Overlay of (C) and (D) shows protein tracks (green) distinctly separate from Pluronic (red) regions. MC = maximum counts per pixel, and TC = total counts.

3.4.5 Necessity and sufficiency of fluorosilane micropatterning steps

To further understand the molecular mechanisms of the fluorosilane-based micropatterning method, we tested the necessity and sufficiency of each step of the method by quantifying cell attachment inside the prescribed micropatterns versus outside (Table 3.2, Figure 3.4). Cells were stained with Hoechst 33342 to simplify cell counting. For each condition, five representative 10X fields of view were analyzed by taking preset rectangular ROIs (40 μm x 869 μm) at the original positions of the cell-adhesive tracks and the cell-repellant background regions (120 μm x 869 μm). From the thresholded Hoescht-stained images, the cell attachment densities in the adhesive and repellant ROIs were calculated as the nuclei count per unit area. A score for micropatterning fidelity termed the cell attachment ratio, ϕ, was calculated using the equation:

$$\phi = \frac{n_a - n_r}{n_a + n_r}$$

where n_a and n_r are the adhesive and repellant region cell densities, respectively, with possible values of: $-1 \leq \phi \leq 1$. For reference, a score of $\phi = 1$ signifies a perfect micropattern, with all cells attached inside the prescribed microtracks and no cells outside; a score of $\phi = 0$ signifies a perfectly homogeneous surface; and a score of $\phi = -1$ signifies a perfect inverted micropattern with all cells outside the prescribed microtracks and none inside. Positive and negative values of ϕ signify preferential cell attachment to the cell adhesive and repellant zones, respectively.

Table 3.2 shows the conditions tested and resulting cell attachment ratios. Condition 1, which included all steps, showed the highest cell attachment ratio ($\phi = 0.976 \pm 0.022$), with the highest cell density in adhesive regions, and lowest cell density in cell repellant regions amongst all conditions. In condition 2, which lacked Pluronic F127, there was a faint cell pattern, but cells significantly overgrew into cell repellant

regions ($\phi = 0.276 \pm 0.088$). In condition 4, in which there was neither Matrigel coating of microtracks nor Pluronic background, there was very low cell attachment in the cell adhesive regions and nonspecific attachment in the cell repellant regions ($\phi = 0.102 \pm 0.089$). In condition 5, in the absence of fluorosilane deposition, cells showed moderate attachment in cell adhesive regions, but overgrew into cell repellant regions ($\phi = 0.515 \pm 0.040$), suggesting that fluorosilane deposition plays a key role in repelling cell attachment. In condition 6, in the absence of both fluorosilane deposition and plasma etching, cells showed moderate attachment in the cell adhesive regions and overgrowth into cell repellant regions ($\phi = 0.564 \pm 0.044$).

We further tested whether micropatterns would form in the absence of pre-adsorbed Matrigel using the same fluorosilane etching technique. It is known that cell adhesion proteins present in serum, such as fibronectin and vitronectin, preferentially adsorb to moderately hydrophilic surfaces rather than hydrophobic ones [135, 136], and using this hydrophilic/hydrophobic tuning was sufficient to form cell micropatterns [135]. In conditions 3 a-c, we examined the effects of hydrophilicity of microtracks on cell attachment. Conditions 3 a-c represent increasing plasma etching doses corresponding to increasingly hydrophilic microtracks, (a: 670 mTorr, 60 W, 1 min; b: 150 mTorr, 60 W, 1 min; c: 150 mTorr, 60 W, 3 min). We found that, with increasing etching doses, there was increased cell attachment, notably more "penetration" of cell attachment incrementally by a few hundred microns towards the interior of the patterning template, also reflected in higher cell attachment ratios in 3b and 3c ($\phi = 0.886 \pm 0.082$ and 0.868 ± 0.112) compared to 3a ($\phi = 0.464 \pm 0.031$). This finding was consistent with previous reports that showed plasma etching is limited by the extent of plasma ion diffusion into microchannels [137]. Penetration of plasma ions into microchannels

depends on the oxygen plasma settings, including duration, partial pressure of oxygen, and power [138, 139]. Cell attachment on hydrophilic microtracks showed lower density and cell spreading than Matrigel-coated surfaces.

Matrigel coating of the etched microtracks apparently overrides the effect of the plasma etching dose (condition 2). Even at the lowest etching dose (670 mTorr, 60 W, 1 min), Matrigel coating ensures high cell attachment (condition 2). This finding posed the question of whether the plasma etching step was necessary. In condition 7, in the absence of plasma etching, there was minimal cell attachment, even onto Matrigel microtracks. This result suggested that Matrigel adsorption depends on some minimal threshold of substrate hydrophilization. Even a low plasma etching dose (condition 2) likely provided sufficient but necessary hydrophilization for Matrigel and cell attachment. This result is consistent with Kohen et al., who reported that optimal Matrigel adsorption occurs on plasma-treated substrates [126]. Since it was apparent that condition 1 gave the most well-defined micropatterns, we compared its cell attachment ratio against all other conditions using Student's t-tests, and showed statistically significantly ($p < 0.0001$) higher cell attachment ratios than conditions 2, 3a, 4, 5, and 6, and ($p < 0.05$).

Table 3.2: Table of conditions and results for testing fluorosilane-based micropatterning.

Condition	Fluorosilane vapor deposition	Oxygen plasma etching	Matrigel infusion	Pluronic F127	Cell attachment ratio
1	+	+	+	+	0.976 ± 0.022
2	+	+	+	-	0.276 ± 0.088
3a	+	+	-	+	0.464 ± 0.031
3b	+	++	-	+	0.886 ± 0.082
3c	+	+++	-	+	0.868 ± 0.112
4	+	+	-	-	0.102 ± 0.089
5	-	+	+	+	0.515 ± 0.040
6	-	-	+	+	0.564 ± 0.044
7	+	-	+	+	0.669 ± 0.170

+ denotes step was included, - denotes step was not included, ± denotes standard deviation

*Oxygen plasma conditions: + 670 mTorr, 60 W, 1 min; ++ 150 mTorr, 60 W, 1 min; +++ 150 mTorr, 60 W, 3 min

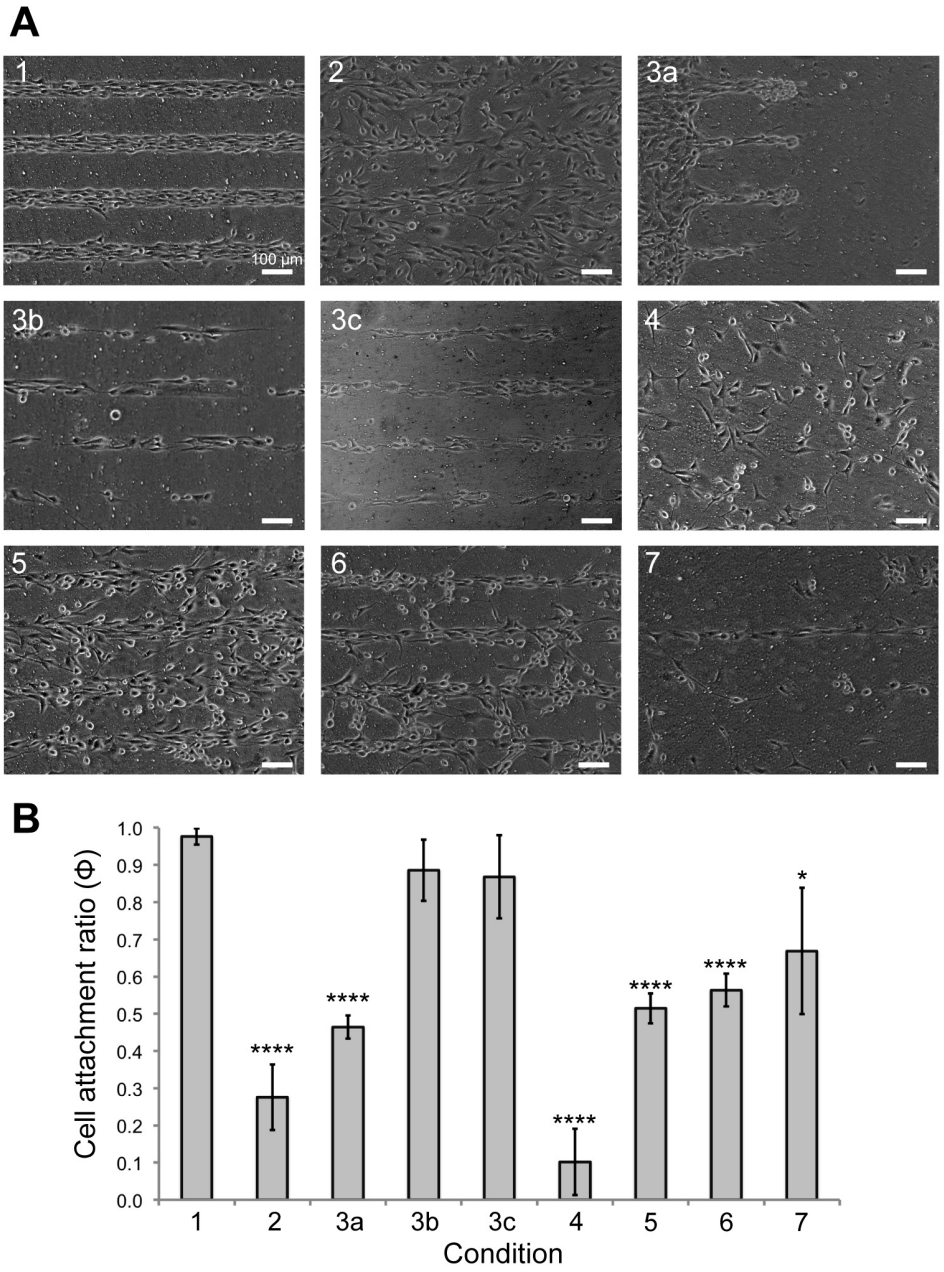

Figure 3.4: Testing of necessity and sufficiency of micropatterning steps.

(A) Representative phase contrast micrographs of C2C12 cell attachment in various conditions shown in Table 3.2. (B) The cell attachment ratios of each of the conditions. p-values shows results of t-tests between condition 1 and all other conditions: **** $p < 0.0001$; *** $p < 0.001$; ** $p < 0.01$; * $p < 0.05$; no sign $p > 0.05$.

We further investigated cell attachment onto micropatterns of fibronectin using the fluorosilane-based micropatterning method. We observed that although initial (Day 1) cell attachment was comparable to Matrigel, cells detached within a culture period of 3 days (Figure 3.5). We surmise that for applications that require protein coatings other than Matrigel, plasma etching conditions will need to be further optimized.

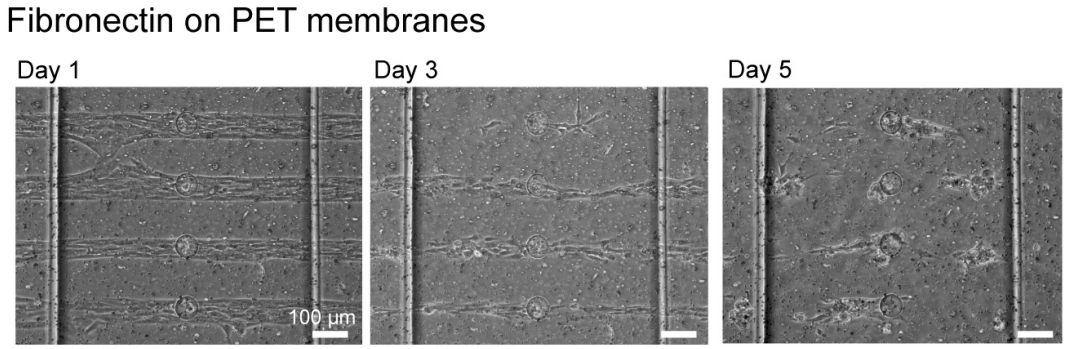

Figure 3.5: Cell attachment on fibronectin-coated micropatterns on PET membranes.

In summary, we determined that all steps of the micropatterning scheme, including fluorosilane deposition, plasma etching, Matrigel coating, and Pluronic adsorption were necessary to form cell micropatterns. Together, the results from contact angle, ToF-SIMS, and cell attachment experiments led us to draw the following conclusions:

- Fluorosilane is necessary for maintaining the cell repellant regions.
- Oxygen plasma etching is necessary for cell attachment in the cell adhesive regions; plasma etching renders hydrophilic surfaces, which promotes Matrigel adsorption; however, cells may still attach in the absence of pre-adsorbed protein, i.e. Matrigel, where the amount of cell

attachment depends on the dose of plasma etching of the underlying fluorosilane which likely affects adsorption of serum proteins.

- Matrigel is necessary to ensure a high density of viable cell attachment.
- Pluronic F127 is necessary for maintaining the cell repellant regions; the effectiveness of Pluronic is dependent upon its physisorption onto the hydrophobic fluorosilane layer.

3.5 CONCLUSIONS

We developed a fluorosilane-based micropatterning method that is a facile and robust strategy for long-term geometric control of cells on PET and glass substrates. We found excellent micropattern fidelity over weeklong cultures of C2C12 myoblasts and C2C12-derived myotubes. A combination of contact angle, ToF-SIMS, and cell attachment results suggest that the establishment of hydrophilic tracks and hydrophobic background regions using plasma etching is critical to pattern formation. The differential wettabilities also allow optimal adsorption of matrix proteins (i.e. Matrigel) onto the cell-adhesive tracks and cell-repelling Pluronic onto the cell-repellant backgrounds. The method can be easily coupled with our modified Transwell focal delivery system, described in **Chapter 4**.

CHAPTER 4: FOCAL DELIVERY OF SOLUBLE FACTORS TO CELLS BY PASSIVE DIFFUSION THROUGH MICROPOROUS MEMBRANES

4.1 SUMMARY

We developed a highly user-friendly microfluidic focal stimulation device based on the modification of a Transwell insert. The device is conceptually simple, relying entirely on passive diffusion. Cells, which are grown "hanging" on the underside of a microporous PET membrane, receive diffusible soluble stimulus from the upper compartment to their basal side through the membrane. Focal delivery is achieved by the bonding of a PDMS masking layer containing apertures onto the porous membrane, rendering only selective areas permeable. The cell side can be micropatterned using the fluorosilane-based micropatterning method described in **Chapter 3**, creating micropatterned cells in register with apertures. The device is easily operated within a standard 6-well plate. We characterized the platform, showing a lower aperture size limit of 20 μm and sustained focal delivery of a plasma membrane dye, wheat germ agglutinin, to cells for up to 48 h, with minimal leakage. Furthermore, we demonstrated the versatility of the system by focally delivering Lipofectamine-pMax-GFP and showing area-specific transfection of a sheet of CHO K1 cells.

4.2 INTRODUCTION

As discussed in **Chapter 1**, one promising approach for focal delivery to cells is by passive delivery through apertures to the basal side of cells through a porous membrane. Our design is based on a modification of the standard Transwell® insert

(Corning Life Sciences), which is a permeable support consisting of a microporous membrane. Cells, which are grown on the membrane, uptake molecules from either the apical side in the media bath above (apical compartment) or from the basal side through the porous membrane (basal compartment) (Figure 4.1A). The commercially available membranes (~ 9 – 23 μm thick) are "track-etched" using charged particle bombardment and chemical etching to create vertical cylindrical pores, which ensure area-specific transport of chemicals without lateral diffusion within the membrane. Utilizing the vertical cylindrical pores, we integrated a PDMS masking (apertures) layer to the porous membrane, which defines permeable open aperture zones to select cells and impermeable PDMS zones (Figure 4.1). Combined with the fluorosilane-based method described in **Chapter 3**, micropatterned cells can be aligned with the apertures, such that only sub-cellular portions of patterned cells are targeted. This design allows area-specific focal delivery of soluble factors to the basal side of select cells within a cell monolayer or micropatterned array.

The device satisfies all of the design criteria established in **Chapter 1**. Utilizing a recently developed dipodal silane bonding technique [68], the device features an "open face sandwich" architecture, in which the porous membrane is bonded on only one side to a PDMS layer, facilitating open access cell culture. The transparent polyethylene terephthalate (PET) porous membranes are amenable to standard microscopy, and commercially available in pore sizes of 0.4 μm, 1 μm, 3 μm, and 8 μm. The system is user-friendly, fitting into a standard 6-well plate format. Transport by passive diffusion eliminates the need for external equipment, such as tubing and syringe pumps, simplifying operation for non-specialized scientists. Temporal control of focal delivery is achieved simply by switching the solution to a different factor in the basal (upper)

compartment. Furthermore, the substrate, PET, is proven to be biocompatible, and the lack of flow eliminates shear stress, making the system cell-benign. Here, we describe the characterization of the spatial resolution limitations of our fabrication method, the sustainability of focal delivery, and the ability of the cell layer to prevent stimulant leakage into the apical side compartment. We further explore application of the Transwell system in region-selective delivery of a transfection agent, Lipofectamine, to cell sheets.

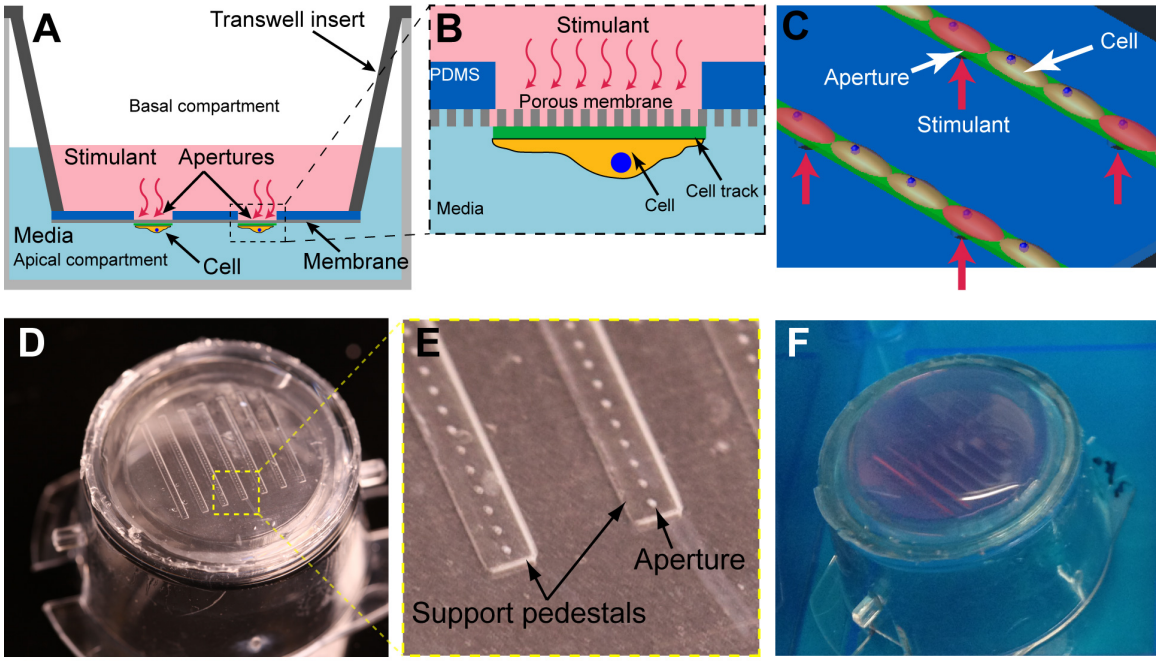

Figure 4.1: Modified apertures Transwell device schematic.

(A) and (B) A side-view cross-section of the modified Transwell device shows that the cells are grown either non-patterned or micropatterned (as shown) on microporous membranes. Apertures, which are in register with micropatterned cells, define the only permeable zones for which stimulant diffuses from the basal compartment to the basal side of cells, contained in the apical compartment. (C) An isometric 3D view of micropatterned cells on a cell microtrack (green) overlying apertures, which are selectively permissive to diffusion of stimulant (red arrows). In principle, only cells overlying apertures (red) are stimulated. (D) A photograph of the modified Transwell insert from the bottom membrane side, showing an array of 7 x 36 (252) of 40 μm apertures. (E) A high magnification view shows an array of 40 μm apertures within columns of support structures. Cell microtracks (not visible) are orthogonal to the columns and overlying the apertures. (F) Cell seeding directly onto the lower membrane side.

4.3 MATERIALS AND METHODS

4.3.1 Microfabrication: photolithography and soft lithography

Standard multi-layer photolithography was used to fabricate SU-8 masters, which were replica molded in PDMS to create the apertures layer. For soft lithography of the apertures PDMS layer, we used an established method from our group, termed "exclusion molding," in which a fluoropolymer-coated polyester sheet was pressed against the tallest SU-8 features, excluding the PDMS pre-polymer from these zones and creating open features, e.g. apertures [101]. Exclusion molding of features shorter than ~80 μm was technically difficult, which limited the apertures layer thickness to 80 μm or greater. Furthermore, due to the aspect ratio limitation of SU-8 (~ 1:3), in order to fabricate apertures of 40 μm diameter or smaller (about the size of an AChR pretzel), we needed SU-8 structures to be no thicker than 120 μm. With these constraints, we designed a two layer SU-8 master mold for the apertures layer: 1) a rectangular base "support pedestal" (200 μm thick) that would aid exclusion molding (these pedestals appear to be rectangular channels in PDMS when viewed from above) and 2) a thin apertures layer (20 μm thick) atop the pedestal layer, giving a total thickness of 220 μm. As a result, the PDMS replica was a series of apertures above rectangular indentations, such that the membrane/cell side is directly apposed to the apertures.

Device features were designed in AutoCAD (AutoCAD 2013 for Mac, AutoDesk, San Rafael, CA) and printed layer-by-layer as a set of Mylar photolithography masks by CAD/Art (Bandon, OR) at 40,000 dpi. Three designs were made: 40 μm diameter apertures in a 12 x 12 array and a 6 x 36 array, and varying aperture diameters of 10, 20, 40, 60, 80, 100, 120, 200, and 400 μm in a 12 x 9 array. SU-8 2000 series epoxy resin photoresist (Microchem, Newton, MA) was spin-coated using a headway spinner onto

100 mm silicon wafers (University Wafers, #590) and photopatterned using multilayer photolithography. To define the pedestals layer, SU-8 2075 was spin-coated twice at 2125 RPM, giving a thickness of 200 μm. After UV exposure at 340 mJ/cm^2 and post-exposure baking, the apertures layer was defined by spin-coating SU-8 2015 at 2100 RPM and UV exposure of 350 mJ/cm^2, followed by post-exposure baking, developing in SU-8 developer, propylene glycol monomethyl ether acetate (Sigma-Aldrich #484431) for 1 hour, and hard baking at 150°C on a hotplate.

For exclusion molding, the master mold was placed onto four sheets of polyester film (Scotchpak 9744 PET film, 3M, St. Paul, MN) on a 4" diameter, 0.5" thick steel disc. PDMS (Sylgard 184 Silicone Elastomer Base and Curing Agent, Dow Corning) was mixed at a 10:1 ratio of elastomer base to curing agent, de-gassed in a vacuum desiccator, and poured onto the masters. Prior to molding, a polyester film was treated under oxygen plasma at a power of 60 W, at 670 mtorr for 30 seconds. This plasma treatment prior to exclusion molding allowed the stiff polyester backing to be non-covalently adhered to the cured PDMS, ensuring intact release of the fragile thin PDMS layer after curing. The plasma-treated side of the film was then placed onto the uncured PDMS, taking care to prevent trapping of air bubbles. Four additional sheets of polyester film were placed over the first sheet and topped by an acrylic disc, and were then compressed using a C-clamp (#5046A18, McMaster-Carr), and cured at 70°C in a convection oven for 2 hours. The PDMS apertures layer was gently released using a sharp blade with the polyester sheet backing still adherent on it. A 25 μm tip micro probe (Bonn Microprobe, #10030-13, Fine Science Tools, Foster City, CA), was used to verify, under a dissection microscope (Nikon SMZ 1500), that exclusion-molded apertures were open. Devices with less than

80% open apertures were discarded. The PDMS apertures layer with its attached polyester backing was then ready for bonding onto the Transwell insert.

4.3.2 Transwell device assembly

The assembly of the modified Transwell device consisted of two steps: 1) bonding of the apertures layer to the bottom of a hollow Transwell insert, and 2) bonding of a microporous track-etched membrane to the PDMS apertures layer. We casted a PDMS flange along the bottom of the original Transwell plastic support devoid of the membrane, providing a PDMS surface for plasma bonding the apertures layer and membrane. An acrylic disc (20 mm diameter, 1/8" thick) with a single side of adhesive was applied onto a 100 mm petri dish (BD Falcon) and used as a spacer in the center, and a PDMS mixture (10:1 base to curing agent) was poured around the spacer. The original Transwell support without the membrane was then pressed down centered around the spacer, and PDMS was allowed to cure at 70°C in a convection oven, creating a PDMS flange for bonding of the membrane/apertures construct (Figure 3.1).

Track-etched PET membranes (1.0 μm pore diameter, 1.6 x 10^6 pores/cm^2, and 3.0 μm pore diameter, 8.0 x 10^5 pores/cm^2), were cut out from a Transwell insert (#353102, BD Bioscience, San Jose, CA) using a sharp blade and bonded to the PDMS apertures using a dipodal silane bonding method described previously [68]. PET membranes were treated with oxygen plasma (60 W, 670 mtorr, 60 seconds) and then immersed in a solution containing 2% v/v bis[3-(trimethoxysilyl)propyl]amine solution (#413356, Sigma-Aldrich), 1% v/v tetrabutyl titanate (#244112, Sigma-Aldrich), and 97% isopropyl alcohol for 20 min at 80°C, then rinsed with isopropyl alcohol and dried in a convection oven at 70°C for 1 hour. The silane-modified membranes were then soaked in 70% ethanol for 30 minutes at room temperature. Prior to bonding, the PDMS

apertures layer was treated with oxygen plasma at a power of 60 W, at 670 mtorr for 60 seconds using a Diener Zepto, placed into conformal contact with the ethanol-wetted porous membrane (with the apertures side facing the membrane) and baked at 70°C in a convection oven for 2 h. This bonding method proved to be hydrolytically stable in cell culture conditions, i.e. in Dulbecco's Modified Eagle's Medium for at least several weeks [Sip, 2014]. Subsequently, the membrane/apertures construct was bonded onto the PDMS flange on the Transwell support under oxygen plasma at a power of 60W, at 670 mtorr for 60 seconds.

Prior to cell culture, the device was sterilized under a UV lamp for 20 minutes, and treated with oxygen plasma to render PDMS apertures hydrophilic and prevent bubbles from clogging them. For homogeneous (non-patterned) cell cultures, Matrigel (#356234, BD Biosciences, San Jose, CA) (1:50 dilution) was coated overnight at room temperature, and for micropatterned cell cultures, a fluorosilane-based micropatterning method (described in **Chapter 3**) was used.

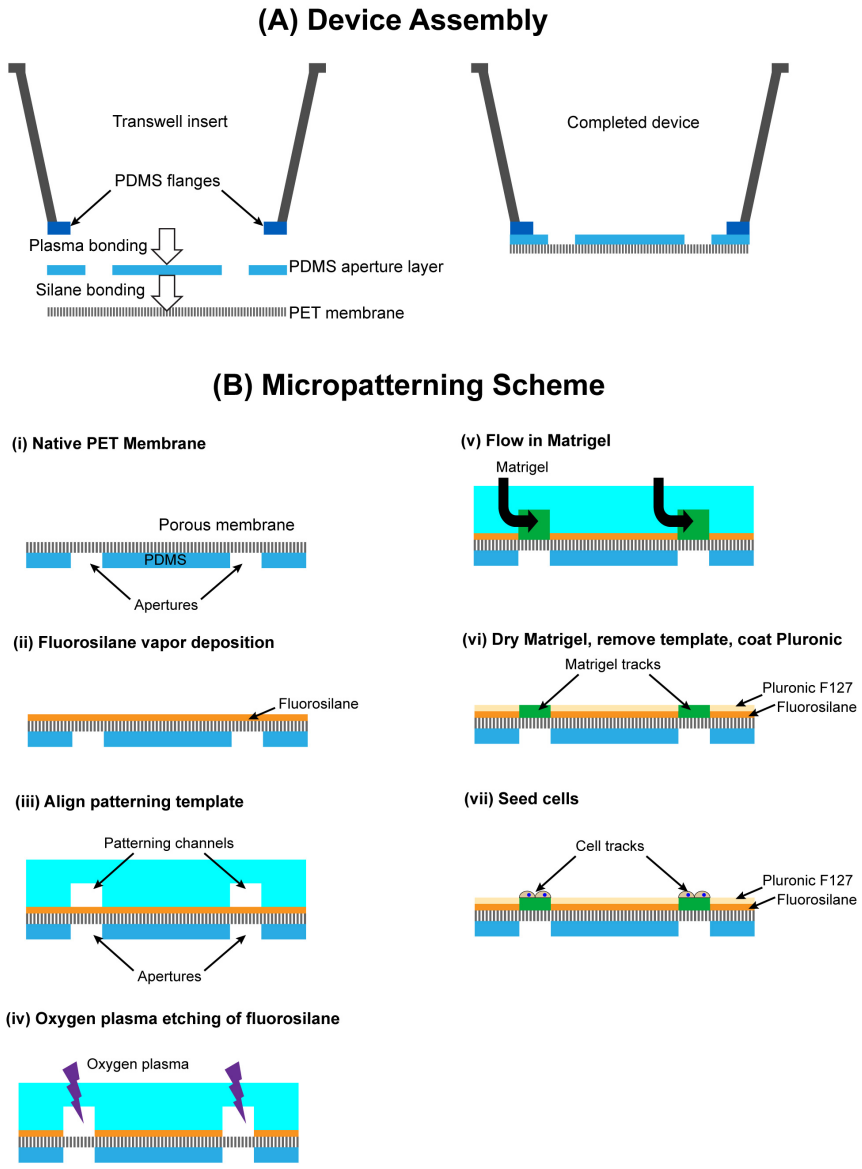

Figure 4.2: Transwell device fabrication and micropatterning.

(A) The exclusion molded PDMS apertures layer is bonded onto a PDMS flange lining the bottom of the hollow Transwell insert. Subsequently, the porous PET membrane is bonded onto the apertures layer, completing the device. (B) A similar micropatterning scheme as described in Chapter 3 is used: (i)-(ii) The native PET membrane is homogeneously coated with hydrophobic fluorosilane. (iii) A PDMS patterning template with microchannels is aligned in registration with apertures and (iv) oxygen plasma is applied to selectively etch fluorosilane into hydrophilic tracks. (v) The microchannels are filled with Matrigel, creating cell-adhesive tracks. (vi) Pluronic, a cell repellant, is physisorbed onto the hydrophobic regions. (vii) Cells are seeded and selectively adhere to the Matrigel lanes.

4.3.3 Cell culture

C2C12 myoblasts (American Type Culture Collection, Manassas, VA) were cultured and passaged before reaching 80% confluence on TCPS petri dishes coated with 0.1% gelatin (Sigma-Aldrich, #G1393). Cells were either seeded in an "upright" format with the cells attached on the upper side of the membrane, with apertures below them, or in a "hanging" format in which cells were attached on the bottom side of the membrane, with apertures above them. For cell seeding in the hanging format, 800 μL of the cell suspension at 3 x 10^5 cells/mL was applied as a droplet onto the bottom side of the device (Figure 4.1F). Cells were allowed to attach for 1 hour, and washed twice in growth media before placing into a standard 6-well plate and cell culture incubator. Micropatterned cell culture protocols were similar to those described in **Chapter 3**.

4.3.4 Microscopy

Microscope images were acquired using a Nikon Eclipse Ti model inverted microscope with Nikon Plan Fluor 10X / 0.30NA, and Nikon S Plan Fluor EL WD 20X / 0.45NA objectives, fluorescence filter turrets, automated translational stage, and z-positioner (Nikon Instruments, Melville, NY) with a 12-bit cooled CCD camera (ORCA-ER, Hamamatsu, Japan). Large areas of phase contrast and fluorescence images were stitched together using the Nikon Elements software large image ND Acquisition feature. For signal spreading experiments, the same fields of view were semi-automatically tracked over different timepoints using the well-plate macro feature in Nikon Elements. The regularly spaced apertures provided landmarks to return to the same fields of view over many acquisitions.

4.3.5 Device operation and characterization of signal spreading

To measure the effectiveness of soluble factor delivery to specific regions, we added calcein AM (#C3100MP, Life Technologies) at 25 μM, wheat germ agglutinin-Alexa Fluor 647 conjugate (WGA) (#W32466, Life Technologies) at 10 μg/mL, and/or Hoechst 33342 (#H3570, Life Technologies) to the basal compartment and followed the staining of cells using time-lapse epi-fluorescence microscopy (Figure 4.3 and Figure 4.4).

4.3.6 Image analysis

Image analysis was performed using Fiji (ImageJ, National Institutes of Health, Bethesda, MD) software. For quantitative analysis of the temporal spread of the WGA signal, we took the fluorescence intensity linescan surrounding the aperture. The micropatterned cells allowed straightforward quantitation, as signal spreading was mostly in the x-direction, allowing rectangular regions of interest (ROIs) that could be designated along the axis of the cell tracks. The full width at half maximum (FWHM) of the linewidth curve was recorded as a measure of WGA fluorescence signal in the x-direction.

4.3.7 Characterization of molecular transport through microporous membranes

To assess the permeability of the modified Transwell focal stimulation device, and the reliability of cell-cell junctions to prevent leakage and diffusive broadening of focal signal, we measured the flux of fluorescently-conjugated Dextran (70 kDa) (Dextran-70 kDa-fluorescein, Life Technologies #1823), from the bottom compartment (well-plate) into the upper compartment following an established protocol [140, 141]. We compared an unmodified Transwell insert (1.0 μm pores) to our modified Transwell device containing 144 x 40 μm apertures bonded to a 1.0 μm porous membrane with and

without cultured myotubes (10 days). A 1.5 mL volume of Dextran-70kDa-fluorescein (0.5 mg/mL) in growth media or PBS was added to the basal compartment, while a 1.5 mL volume of growth media or PBS was added to the apical compartment. At time points of 0, 4, 8, and 24 hours, a 10 μL sample was collected from the apical compartment, diluted 1:10 in PBS to 100 μL, and measured for fluorescence intensity using a microplate reader (Safire II, Tecan Group Ltd., Mannedorf, Switzerland). We inferred the permeabilities of the systems from the amount of fluorescent Dextran transported into the upper compartment.

4.3.8 Localized cell transfection

We demonstrated localized delivery of a transfection agent, Lipofectamine 2000, carrying the plasmid DNA, pMax GFP (Lonza Amaxa Nucleofector kit) which has a ubiquitous promoter and can be taken up and universally expressed in CHO K1 cells. Prior to the transfection experiment, the device membrane was homogeneously coated with Matrigel (1:50 dilution in DMEM) for 1 hour and washed. Chinese Hamster Ovary cells (CHO K1, ATCC #CCL-61) were seeded at a density of 2.7×10^5 cell/mL such that the cell monolayer was at 70% confluence during the time of transfection. Dilutions of 4.84 μg plasmid DNA in 700 μL OptiMEM and 57 μL Lipofectamine 2000 (Invitrogen) in 743 μL OptiMEM were prepared. The DNA dilution and Lipofectamine dilution were mixed in a 1:3 ratio and incubated for 5 min at room temperature. 1.5 mL of the transfection dilution mixture was added to the basal (upper) compartment while 1.5 mL of Opti-MEM with no serum was added the apical (lower) compartment. Cells were kept in transfection medium for up to 24 hours, after which medium was changed to Opti-MEM containing serum, and final observations were made at 43 hours.

4.4 RESULTS AND DISCUSSION

4.4.1 Focal delivery and characterization of signal spreading

To test the ability of our system to focally deliver molecules to cells, we characterized the transport of low molecular weight species, calcein AM and Hoechst 33342, and high molecular weight species, wheat germ agglutinin (WGA). Calcein AM, acetoxymethyl (AM) (M.W. 994.87 Da) is an ester derivative of the fluorescent dye calcein containing lipophilic groups that permeate cell membranes. Once inside the cell, nonspecific intracellular esterases cleave the lipophilic groups, yielding calcein, a fluorescent dye that is retained in the cytoplasm and labels the whole cell. Calcein AM was applied in the basal (upper) compartment of the modified Transwell with non-patterned or micropatterned cells on the porous membrane on the apical (lower) compartment side, such that only the basal side of cells overlying the aperture open zones would encounter calcein. Figure 4.3A shows non-patterned C2C12 myoblasts overlying a single 40 μm diameter aperture. When calcein AM was applied in the basal compartment, only four cells directly overlying the aperture were selectively stained within 5 minutes. We tested the aperture size limitation of our exclusion molding fabrication method with an array of varying aperture sizes of 10 μm, 20 μm, 40 μm, 60 μm, 80 μm, 100 μm, 120 μm, 200 μm, and 400 μm (Figure 4.3B). Calcein AM and Hoechst (not shown) stained the cell sheet in good agreement with the pattern of the apertures. We observed focal cell staining with aperture sizes as small as 20 μm. Below this aperture size, at 10 μm, we did not observe staining. This suggests that using our fabrication method, the aperture resolution is ~20 μm, or about the size of a single cell. The focal staining observation was extended to micropatterned cells in 40 μm wide cell microtracks overlying 40 μm apertures (Figure 4.3C). When a mixture of calcein and

WGA were applied through apertures, only cells overlying apertures on the micropattern were selectively stained.

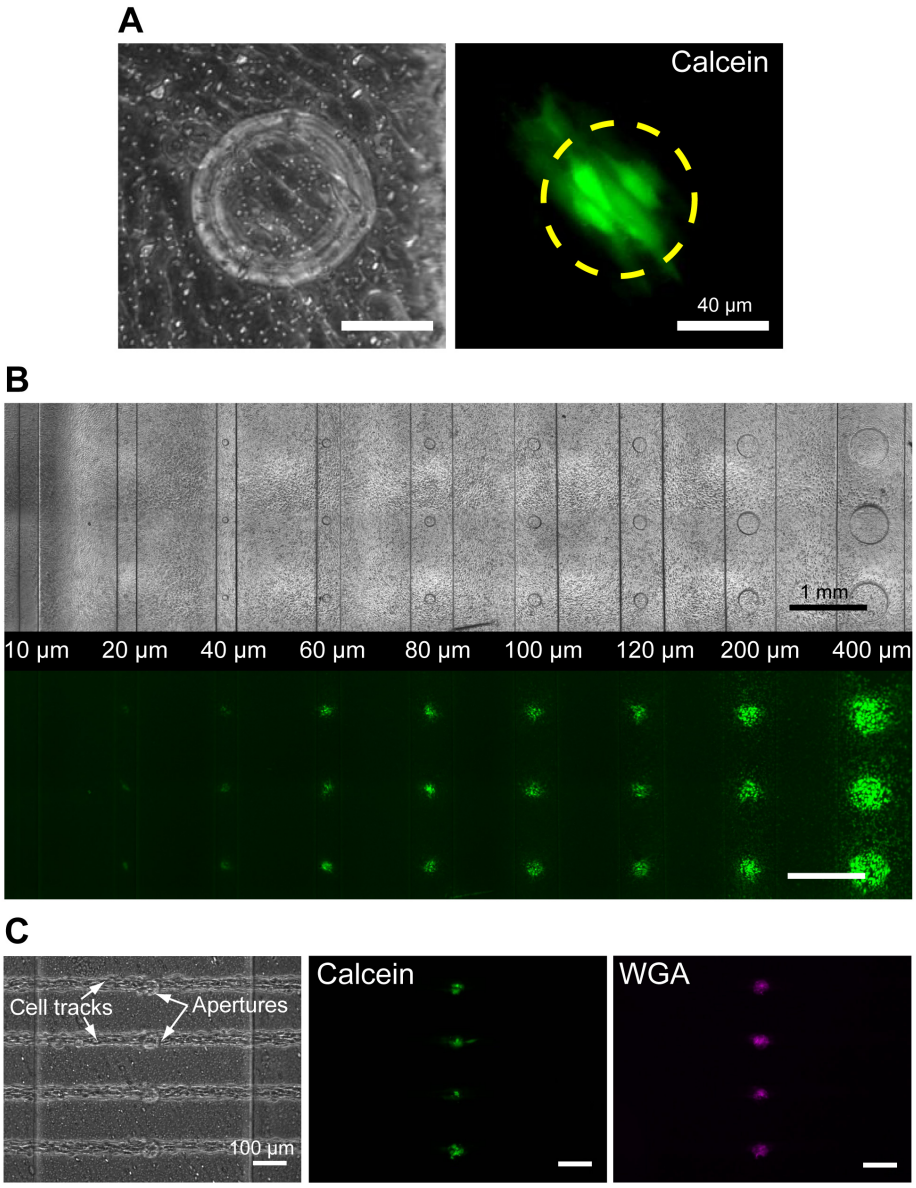

Figure 4.3: Characterization of focal delivery of soluble molecules through apertures.

(A) Non-patterned C2C12 myoblasts on a microporous membrane overlying a single 40 µm diameter aperture. Calcein AM was delivered through the aperture and selectively stained four cells directly above it. (B) A large stitched image of non-patterned myoblasts on a Transwell device with varying aperture sizes of 10 µm, 20 µm, 40 µm, 60 µm, 80 µm, 100 µm, 120 µm, 200 µm, and 400 µm. Cells directly above the apertures were selectively stained with calcein AM, with an apparent limit at 20 µm. (C) Micropatterned C2C12 myoblasts (40 µm, 120 µm separation) in register with 40 µm apertures. Cells were also spatially selectively stained with calcein AM and wheat germ agglutinin (WGA).

To characterize the long-term sustainability of focal delivery of soluble molecules through apertures, we measured the long-term lateral spread of cell staining. Since the working solution of calcein AM is susceptible to hydrolysis, it is only effective as a cell labeling agent for a few hours, after which hydrolysis in solution causes increases background fluorescence. Wheat germ agglutinin (WGA, M.W. ~38 kDa) is a lectin that binds nonspecifically to N-acetylglucosamine and N-acetylneuramic acid residues on cell membranes, and is stable for long-term applications. Thus, fluorescently conjugated WGA, which has been used to stain cell microdomains in a microfluidic laminar flow device [60], was used to visualize long-term focal delivery to subcellular regions of the plasma membrane of myoblasts and myotubes. WGA-Alexa Fluor 647 conjugate was continuously focally applied through the apertures onto non-patterned and micropatterned C2C12 cells and fluorescence images were taken at timepoints of 2, 24, and 48 hours. Figure 4.4A shows WGA applied focally through 40 μm apertures (yellow dotted circles) onto 40 μm microtracks separated by 120 μm and the spread of fluorescence signal over time. The fluorescence intensity linescans of the microtracks (region marked by red dotted rectangles in Figure 4.4A) at each timepoint for a single representative aperture is shown in Figure 4.4B. The full width at half maximum (FWHM) was measured from the linescan and the average FWHM from 6 apertures was plotted against time in Figure 4.4**C**. We observed the FWHM broadening from an average width of 33.7 $\pm$ 6.3 μm at 2 h, to 52.5 $\pm$ 19.7 μm at 24 h, to 68.8 $\pm$ 18.3 μm at 48 h. Thus, from the spread of this model tracer molecule, we determined that our system applies a temporally evolving gradient. Assuming homogeneous cell coverage of the aperture, the timescale of broadening is likely dependent on the molecular weight and binding affinity of the species. We attribute the variation between apertures to several factors: 1) variation in number of available pores, 2) variation in cell coverage of the aperture, and 3) variation

in openness of apertures. 1) Since, the pores in the track-etched membranes are randomly distributed, there is an inherent variation in pores per unit area. 2) There is variation in the local cell density, which may affect the cell-cell junctions from preventing solute leakage. 3) Due to fabrication limitations of the exclusion molding technique, there may be some apertures that are partially closed, i.e. contain a flap of PDMS. All three factors are difficult to control and intrinsically a part of the device design.

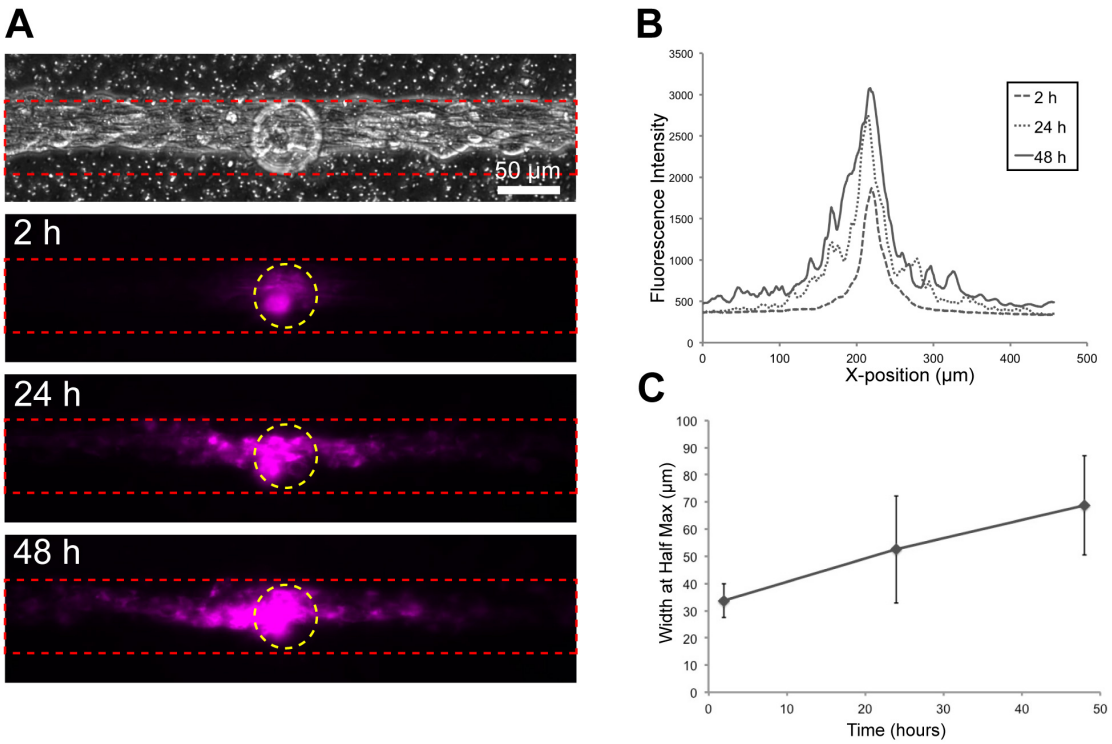

Figure 4.4: Temporal characterization of spread of a cell membrane dye, wheat germ agglutinin (WGA) onto micropatterned C2C12 myoblasts.

(A) WGA fluorescence signal at 2 hours, 24 hours, and 48 hours. (B) Linescans of the single aperture from part (A) at each timepoint. (C) The average width at half maximum of linescans of WGA fluorescence signal from 6 different apertures over 48 hours, showing the lateral spread of WGA. Dots represent the mean FWHM, and error bars represent standard deviation.

4.4.2 Molecular transport through porous membranes and apertures

We examined transport phenomena of species of different molecular weights through the device (i.e through the 1 μm diameter pores). We calculated the Stokes radius of various molecules of interest, given the molecular weight (MW), assuming a solute molecule is spherical:

$$R = \left[\frac{3(MW)}{4\pi N\rho}\right]^{1/3}$$

where N is Avogadro's number, ϱ is the density of water; we calculated the diffusion coefficient in water from the Stokes radius, from the Stokes-Einstein Equation:

$$D = \frac{kT}{6\pi\eta R}$$

where k is the Boltzmann's constant, T is temperature (assume 298 K), η is the viscosity of water, R is the Stokes radius. So the diffusion constant is related to molecular weight by:

$$D = \frac{kT}{6\pi\eta\left[\frac{3(MW)}{4\pi N\rho}\right]^{1/3}}$$

Therefore diffusion coefficient is proportional to molecular weight by the following relationship:

$$D \sim (MW)^{-1/3}$$

The Stokes radii and diffusion coefficients in water for some solutes of interest in our experiments in **Chapter 4** and **Chapter 5** are shown in Table 4.1.

Table 4.1: Calculated Stokes radii and diffusion coefficients of solutes of interest

Species	MW (g mol^{-1})	Stokes Radius (m)	Diffusion Coefficient (cm^2 s^{-1})
Calcein AM	994.87	7.3×10^{-10}	2.99×10^{-6}
Wheat Germ Agglutinin	38,000	2.5×10^{-9}	8.72×10^{-7}
Agrin (C-terminal fragment)	90,000	3.3×10^{-9}	6.61×10^{-7}
Dextran (70kDa-FITC)	70,000	3.0×10^{-9}	7.27×10^{-7}

The radius of the solutes (even with large proteins like agrin) is many orders ($\sim 10^3$) of magnitude smaller than the pore radius. Therefore, we do not expect significant physical solute-pore interactions, but there may be nonspecific adsorption of solute (i.e. agrin adsorption) on the pores, which may hinder their transport.

Given the density of 1.6×10^6 pores/cm^2 of a commercially available 1.0 μm pore track-etched membrane (Corning Life Sciences), we calculated that only 1.3% of the area of the membrane consists of void space. In our modified Transwell device, we mask most of the surface area of the porous membrane such that, in a 12 x 12 aperture device, only 144 individual 40 μm apertures overlying porous membrane are permissible (only 0.058% of the surface is permissible through apertures). This further reduces the void surface area of the entire device surface to 0.0000754%. Therefore, the total area for flux is extremely small even if the diffusion coefficient for a single molecule through each 1 μm pore is unaffected by the pore walls. As with a conventional Transwell, we expect a molecular gradient across the membrane during device operation [142], but in the case of the modified Transwell, due to a much smaller available area for flux, we expect transport to occur much slower, as shown in Figure 4.5.

We compared the transport of a high molecular weight inert molecule, fluorescently-conjugated Dextran, through conventional versus modified Transwells with

and without cells over a period of 24 h. The results were not surprising, in order of decreasing permissiveness, indicated by fluorescence intensity units at 24 hours: 1) conventional Transwell (1650 $\pm$ 216), 2) modified Transwell with apertures without cells (669 $\pm$ 26), 3) modified Transwell with apertures and cells (15 $\pm$ 3) (Figure 4.5). Notably, there was negligible Dextran in the apical compartment after 24 h, suggesting that cell-cell junctions blocked Dextran transport across the membrane. This is consistent with our expectations that 1) the PDMS masks much of the surface area of porous membrane, thereby reducing the total flux considerably, 2) the cell-cell junctions effectively seal off soluble factors from escaping past the basal side of the cells, especially in the case of large molecular weight species, such as 70 kDa Dextran.

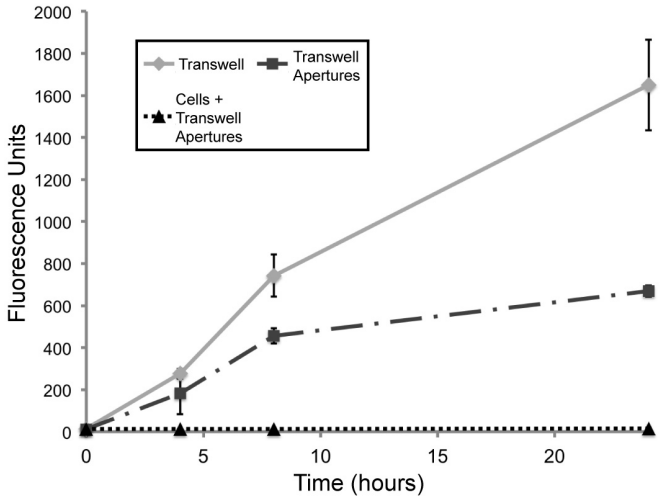

Figure 4.5: Fluorescent Dextran-70kDa permeation through three different devices in 24 hours.

We see that the fastest to slowest Dextran transport occurs in the following order: 1) conventional Transwell, 2) modified Transwell with apertures without cells, and 3) and modified Transwell with apertures with a monolayer of cells.

4.4.3 Localized cell transfection

As a proof-of-principle, we tested the feasibility of our system to locally transfect cell clusters using lipoplexes. Since lipoplexes such as Lipofectamine 2000 aggregate

into large particles, ranging from 200 nm to 2 μm in diameter, they are expected to sediment in solution [143]. Due to this phenomenon, we tried a "top-down" transfection scheme where lipoplexes would settle by gravity onto the basal side of "hanging" cells on the underside of the porous membrane. Indeed, we found zero transfection efficiency when cells were cultured in the upright configuration where Lipofectamine was delivered "bottom-up"; whereas much higher localized transfection efficiencies were observed with a top-down approach. For this application, a larger pore size membrane, 3 μm, was used to accommodate transport of the lipoplex particles and a PDMS layer with varying sized apertures from 10 μm to 400 μm was used to test the limit of transfection localization.

CHO K1 cells were seeded at 70% confluence onto the bottom of modified Transwell devices and transfected for 43 hours using a 1:3 DNA: Lipofectamine ratio. We observed localized cell transfection overlying and adjacent to the apertures occurring in aperture sizes from 400 μm to as small as 60 μm (Figure 4.6A). For quantitative image analysis, all transfected cells were manually segmented. The transfected cell position, defined as the distance of the cell centroid to the nearest aperture center, was determined. This data was then binned into five 100 μm intervals, up to 500 μm outward from the aperture center, or the halfway point to the next nearest aperture. The transfected cell count was divided by the area of its bin, i.e. the area of the concentric circle or donuts from the center to 500 μm, to obtain a cell transfection density. The cell transfection densities were plotted as histograms for three representative aperture sizes, 100 μm, 200 μm, and 400 μm (Figure 4.6B). In all three cases, a large percentage of the transfected cells were positioned overlying the aperture, i.e. left of the dotted line in the histograms. We saw a sharp dropoff from the aperture edge (dotted line) to the next bin outside of the aperture, proving that transfection was largely localized to cells above the apertures.

Next, to illustrate differences in the mean and median positions of transfected cells in the different aperture size groups, we plotted the positions of transfected cells as cumulative distribution functions (Figure 4.6C). The mean and median positions of transfected cells were: 208 $\pm$ 109 μm and 189 μm for 400 μm apertures; 111 $\pm$ 80 μm and 87 μm for 200 μm apertures; 81 $\pm$ 63 μm and 64 μm, 100 μm apertures. The dotted lines represent the aperture edges; the percentage of transfected cells encompassed within the edge was: 54% for 400 μm apertures, 58% for 200 μm apertures, and 35% for 100 μm apertures. Since the data was not normally distributed, a non-parametric Kruskal-Wallis one-way analysis of variance was used to test the null hypothesis that cell transfection positions were equal between the aperture sizes. A p-value < 0.001 was obtained, rejecting the null hypothesis, indicating that all groups were statistically different, and that there was regio-selectivity of cell transfection based on aperture size.

The presence of transfected cells outside of the apertures was likely due to either leakage of lipoplex particles through gaps between cells or migration of transfected cells. Optimal transfection necessitated that cells be seeded at 70% confluence, thus allowing gaps for particles to pass through. The low transfection efficiency seen in apertures smaller than 100 μm is likely due to the large sizes of lipoplexes. Since their size range is 200 nm to 2 μm, and pore sizes are 3 μm diameter, transport through the pores may approach the Knudsen diffusion regime, where collisions of the particle and pore walls become significant. Further characterization of the relationship between lipoplex particle size, pore size, and transfection efficiency will need to be carried out. One strategy to circumvent the problem of delivering large lipoplex particles through microporous membranes is to deliver small molecule activation agents to otherwise quiescent lipoplexes [144]. For example, Aytar et al. described a ferrocenyl cationic lipid that is

dormant when oxidized and is only activated by presentation of a reducing agent. They demonstrated millimeter-resolution spatial control of transfection by delivering the reducing agent to inactive lipoplexes homogeneously distributed on a cell layer. We predict that we will achieve much higher transfection spatial resolution combining this small molecule transfection strategy with our modified Transwell system, i.e. comparable to our calcein AM focal delivery results, where localized delivery on the order of 20 μm resolution was seen. Spatial control of transfection has many applications, including in the study of protein-protein and protein-drug interactions [145, 146] and as test platforms for cellular responses for developmental biology and tissue engineering studies [147]. Tavana et al. described a two-phase polymer system consisting of polyethylene glycol and dextran to control microscale delivery of Lipofectamine to a monolayer of cells [148]. However, resolution (~ 300-350 μm) was limited due to the size of the dispensing tip and the interfacial tension forces inherent in the method. We envision the spatial resolution and user-friendliness of our system will enable high-throughput cell transfection experiments delivering multiple genes to cell clusters for a broad range of applications.

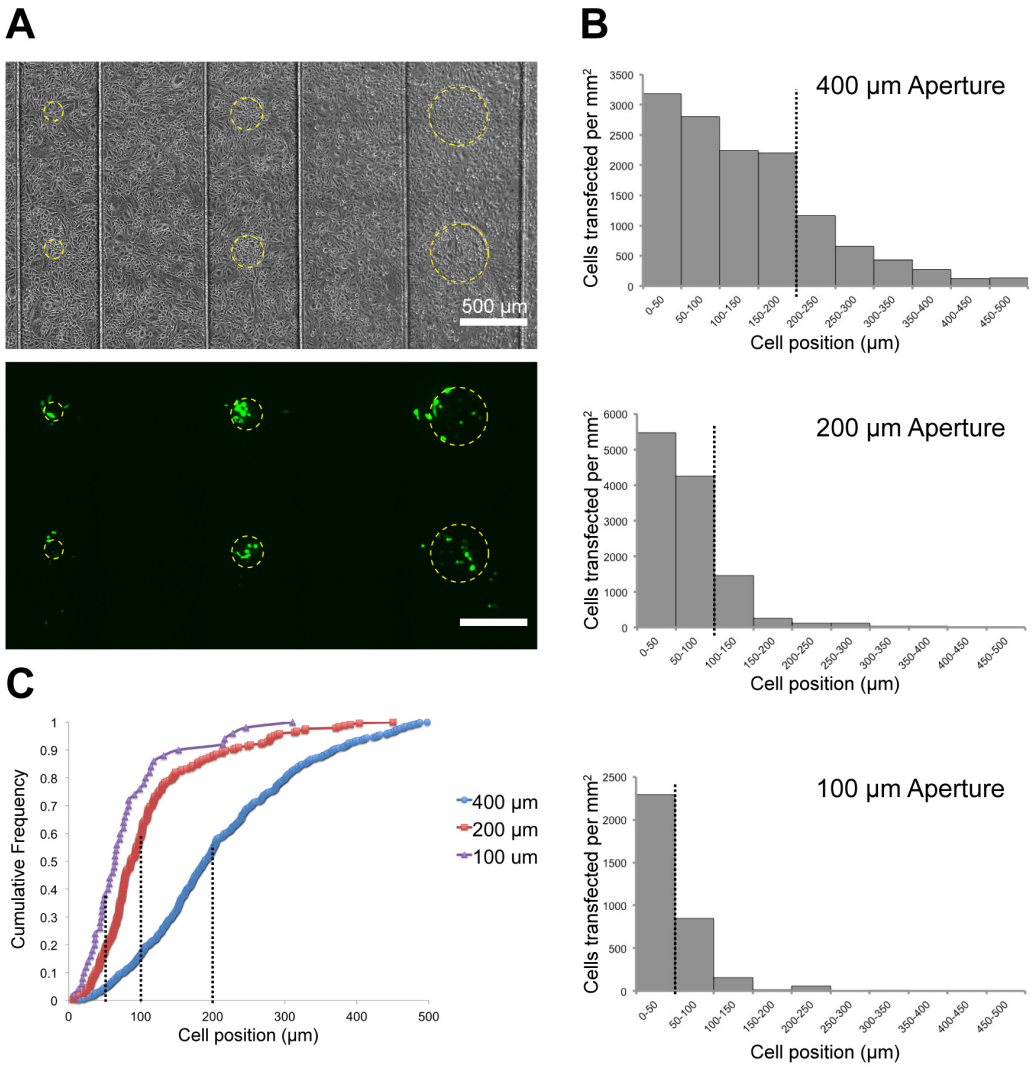

Figure 4.6: Regio-selective transfection of CHO cells with Lipofectamine 2000/pMax GFP complex.

(A) Brightfield image of a monolayer of CHO cells (nonpatterned) on the bottom of a Transwell aperture device with varying sized apertures (10 µm-400 µm diameters), with 120 µm, 200 µm, and 400 µm shown. (B) In the corresponding fluorescence micrograph, transfected CHO cells expressing GFP are mostly localized directly over or adjacent to the apertures. (B) The density of transfected cells (cells/mm^2) plotted as histograms with each bin normalized by its area as the area of each concentric ring. The dotted line indicates the extent of the aperture edge from center. (C) Cumulative distribution curve showing the frequency of positions of the transfected cells for apertures sized 100 µm, 200 µm, and 400 µm. Dotted lines indicate the outer boundary of the respective apertures.

4.5 ALTERNATIVE MODULES: MEMBRANE-BASED FOCAL STIMULATION

4.5.1 EPON 1002F photoresist: an alternative membrane material

Although the modified Transwell with PDMS apertures gave us basal side focal application results, there were a number of drawbacks to the approach. First, exclusion molding often yielded only about 60-70% open apertures in the 12 x 12 40 μm apertures device. This problem stemmed from the photolithography of the SU-8 masters: care was needed to ensure that the SU-8 photoresist was very flat – microscale unevenness resulted in exclusion molding failure on the side with thinner photoresist. Even with troubleshooting and using care during the critical spincoating and baking steps, it was still challenging to get more than 90% of features exclusion molded. Closed features could be opened using a fine 20 μm tip, but this process was highly tedious. Second, wafers failed – i.e. cracked or SU-8 features detached – after a few cycles of exclusion molding, necessitating time-consuming fabrication of new masters. Third, the thick 220 μm PDMS support structures caused phase contrast microscopy halo effects. This could not be avoided as the exclusion molding method becomes technically challenging for films thinner than 100 μm. Finally, fluorescence and bright field microscopy image quality through porous PET membranes was compromised by the presence of speckles.

We looked for an alternative masking material by which a permeable membrane could be directly patterned with arbitrary features. SU-8 has served as a structural material in microfluidic devices but its autofluorescence and brittleness preclude its application for forming thin freestanding films. EPON 1002F resin was recently found to be a high resolution, high aspect ratio negative photoresist comparable to SU-8, with low autofluorescence [149]. SU-8 shows high background fluorescence, especially in the green wavelengths (Figure 4.8A), an emission wavelength for common dyes such as

FITC and GFP. 1002F was used to make thin freestanding films with features as small as 5 μm on 10 μm thin films using standard photolithography [150, 151]. The ability to generate 5 – 10 μm holes would allow EPON films to directly support cell growth and substitute both the PDMS and PET porous membrane components of the former design. Thus, we considered EPON 1002F as an attractive alternative biomaterial for defining apertures, essentially enabling user-defined microporous membranes.

4.5.1.1 Fabrication of EPON 1002F thin films

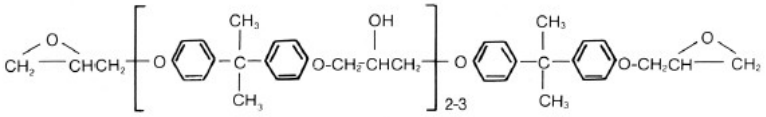

Figure 4.7: Chemical Structure of EPON 1002F Resin

EPON 1002F is an epoxy-based resin (Figure 4.7). The crosslinking reaction is similar to that of SU-8, but the crosslinked 1002F product consists of linear chains of the resin molecule. Polymerization begins when UV light activates the photoacid generator (photoinitiator) compound. Once the acid cation is generated, it induces ring opening of the epoxide group at one of the ends of the molecule. The resulting carbocation reacts with the epoxide group of a neighboring resin molecule to induce polymerization. The EPON 1002F photoresist was prepared by dissolving resin (phenol, 4,4'-(1-methylethylidene)bis-, polymer with 2,2'-[(1-methylethylidene) bis(4,1-phenyleneoxymethylene]bis[oxirane]) (Miller-Stephenson, Sylmar, CA) powder into gamma-butyrolactone (Sigma-Aldrich, St. Louis, MO) solvent at 49% and 46.1% of the desired final weight, respectively. The photoinitiator, triarylsulfonium hexafluoroantimonate salts (Sigma-Aldrich, St. Louis, MO), was later added at 4.9% of the desired final mass. Glass slides (75 x 50 mm) were cleaned using acetone, IPA, and

deionized water, and oxygen plasma etching (60 W, 60 seconds, 670 mTorr). The photoresist was made as a 10 μm thick film on 75 x 50 mm glass slides by spin-coating at 10 seconds at 500 RPM, then 30 seconds at 2000 RPM, then soft baked at 95°C for 30 minutes. UV exposure was optimized to be 50 mJ/cm^2 for a mask aligner with 3.98 mW/cm^2 power. Post-exposure baking was done at 4 minutes at 95°C, then 4 minutes at 120°C. Glass slides were gently developed in propylene glycol monomethyl ether acetate (PGMEA) for 10 seconds and rinsed in IPA, and finally hard baked at 10 minutes at 95°C, and 30 minutes at 120°C. The films were then soaked in deionized water overnight, and detached from the glass substrate, and can be handled by tweezers Figure 4.8C. We were able to generate arbitrary patterns in EPON 1002F photoresist, making the University of Washington "W" logo consisting of 8 μm holes (Figure 4.8D and Figure 4.8E).

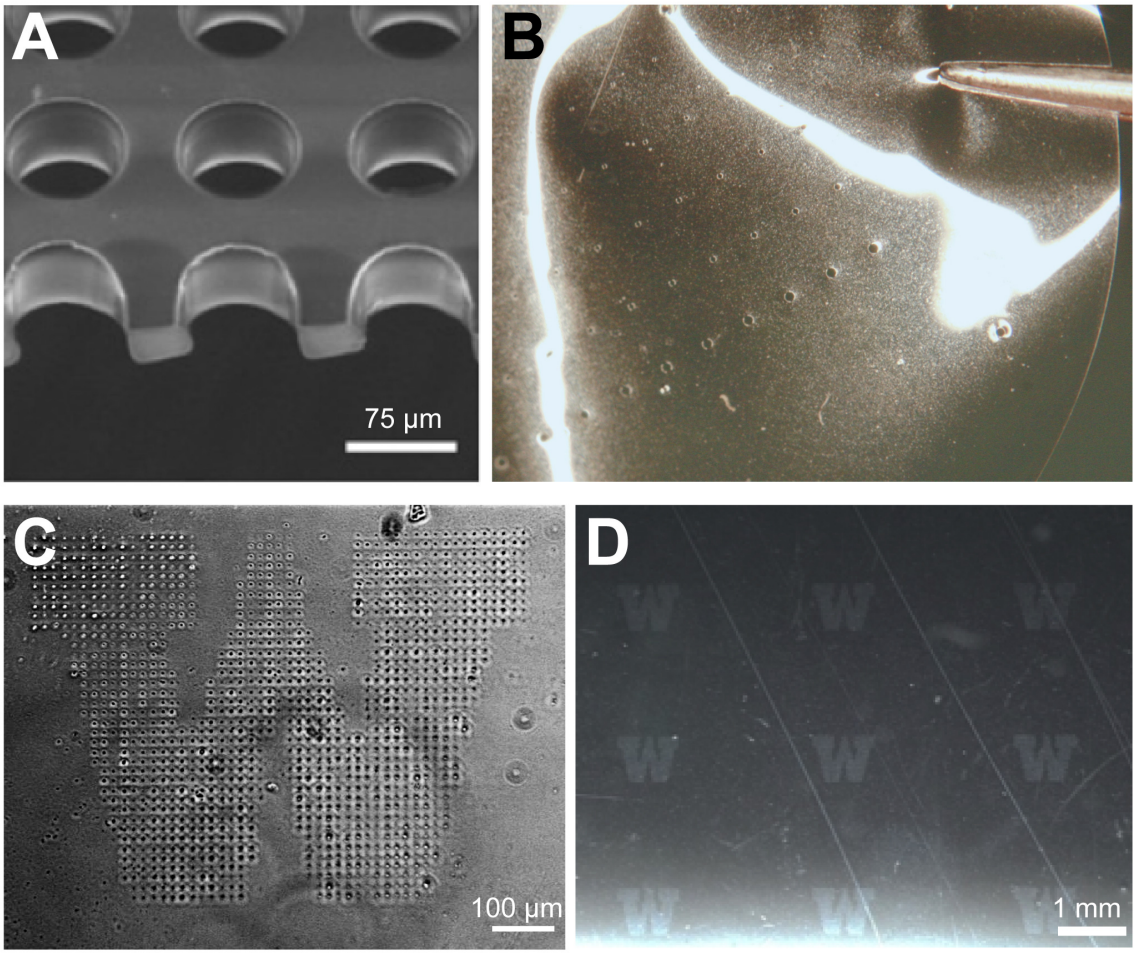

Figure 4.8: EPON 1002F photoresist.

(A) Representative SEM image of 75 µm diameter through-holes on a released EPON 1002F film. Adapted from [150]. (B) EPON 1002F film can be released from the substrate to be a freestanding membrane that can be integrated with other microfluidics materials such as PDMS and PET. Note the holes pattern (200 µm to 10 µm diameter holes). (C) A "W" University of Washington logo consisting of 8 µm through-holes in 1002F. (D) A 3 x 3 series of "W" patterns on the same 1002F film.

4.5.1.2 Integration of EPON 1002F films into PDMS devices

We designed a variation of the Transwell device in which cells are grown on a EPON 1002F film instead of a PET membrane. The customizability of the EPON film would negate the need for a PDMS masking layer. However, we still needed a method to

integrate EPON films into Transwell inserts via the PDMS flange. We found that plasma-treated EPON 1002F films could not be bonded to unmodified or oxidized PDMS. However, we considered that the film contained residual, unreacted epoxide groups, which could react with amine groups. PDMS was treated with 5% 3-Aminopropyl triethoxysilane (APTES) at 80°C, and brought into conformal contact with EPON 1002F film, where the materials formed a stable bond. This allowed the films to be integrated into Transwell inserts via the PDMS flange (Figure 4.9). The EPON 1002F-PDMS bond remained stable in cell culture media at 37°C for at least 10 days. Temporary bonding of 1002F to APTES-treated PET membranes was also achieved, but the bond failed after 24 hours in cell culture media at 37°C.

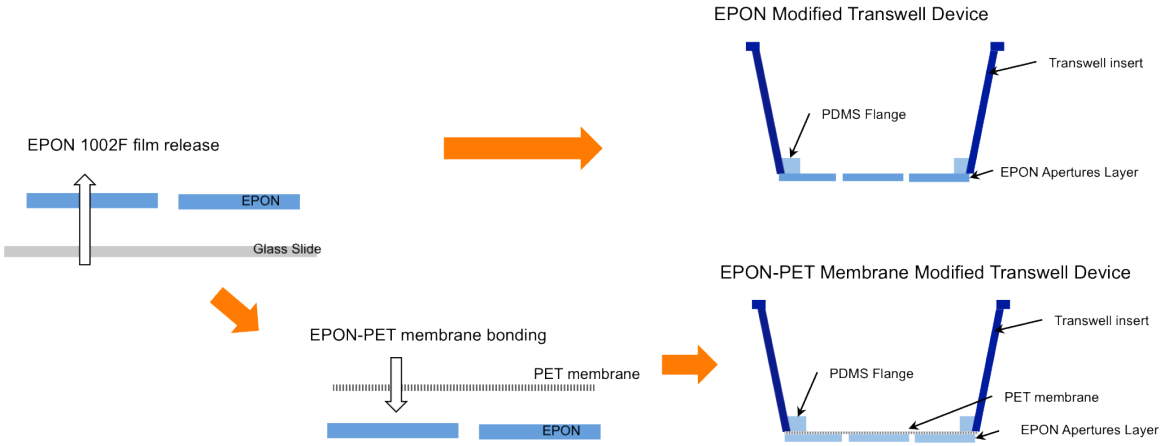

Figure 4.9: Fabrication of EPON-based Transwell devices.

Two strategies for integrating EPON into Transwell inserts: 1) stand-alone films of EPON on Transwell bottoms, 2) EPON bonding to PET membranes.

4.5.1.3 Biocompatibility of EPON 1002F films

For biocompatibility testing, EPON 1002F films were plasma oxidized (60 W, 670 mTorr, 60 seconds), coated with Matrigel, and seeded with C2C12 cells. A LIVE/DEAD kit (Invitrogen) was used to assay cell viability. Very few dead cells (less

than 1%) were found on the substrate after one day of culture. 1002F was also amenable to micropatterning using the fluorosilane etching method described earlier. The transparent thin films show excellent optical clarity for microscopy.

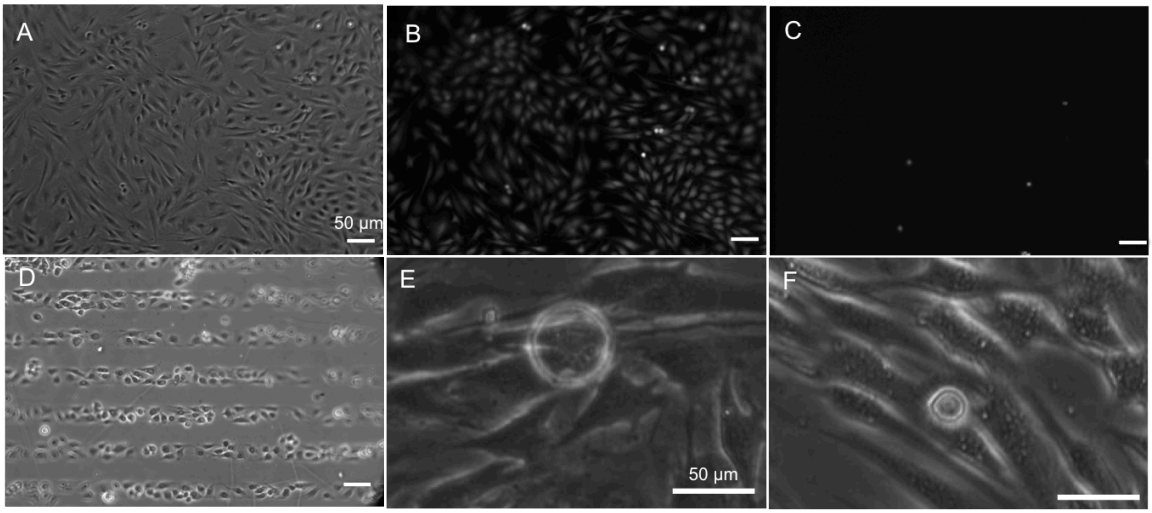

Figure 4.10: EPON 1002F film viability and imaging.

(A) C2C12 myoblasts adhere to Matrigel-coated EPON 1002F photoresist. (B) LIVE (calcein) stain of cells. (C) DEAD (ethidium homodimer) stain of cells. (D) EPON 1002F is amenable to the fluorosilane-based micropatterning method. (E) Cells straddle a 40 µm diameter aperture. (F) A single cell straddles a 20 µm diameter aperture.

4.5.1.4 EPON 1002F films for focal delivery of soluble factors

We applied the same focal calcein assay as described in Section 4.4.1, but saw homogeneous rather than focal calcein staining of cells. We attribute this to leakage of calcein, possibly due to defects and holes in the EPON 1002F films. Overall, we found a method of bonding EPON 1002F films to PDMS, but needed to optimize our fabrication method to make films without defects.

4.5.2 Basal-side channels design: an alternative design for multiplexed focal delivery

We modified the Transwell design to build a system capable of focal delivery of multiple stimuli. The design is again based on a porous membrane that separates the cell compartment above and the fluidic compartment below. The basal-side channels device, shown in Figure 4.11, consists of a porous PET membrane directly above a network of PDMS microchannels contained within a glass-bottom 55 mm petri dish. The microchannels deliver the soluble factor through the porous membrane and onto the basal side of cells on the membrane. The design is an open-chamber format within a petri dish, allowing standard cell culture protocols, straightforward cell seeding, and maintenance of steady gas/nutrient concentration, pH, and osmotic stability. The device is operated with syringe pumps connected via tubing to a PDMS inlet and outlet ports layer which accesses the microchannels. Although this is a flow-based design, the track-etched PET membrane shields cells from exposure to high shear stresses due to the high fluidic resistance of the 1 μm diameter pores relative to the microfluidic channels [66, 67].

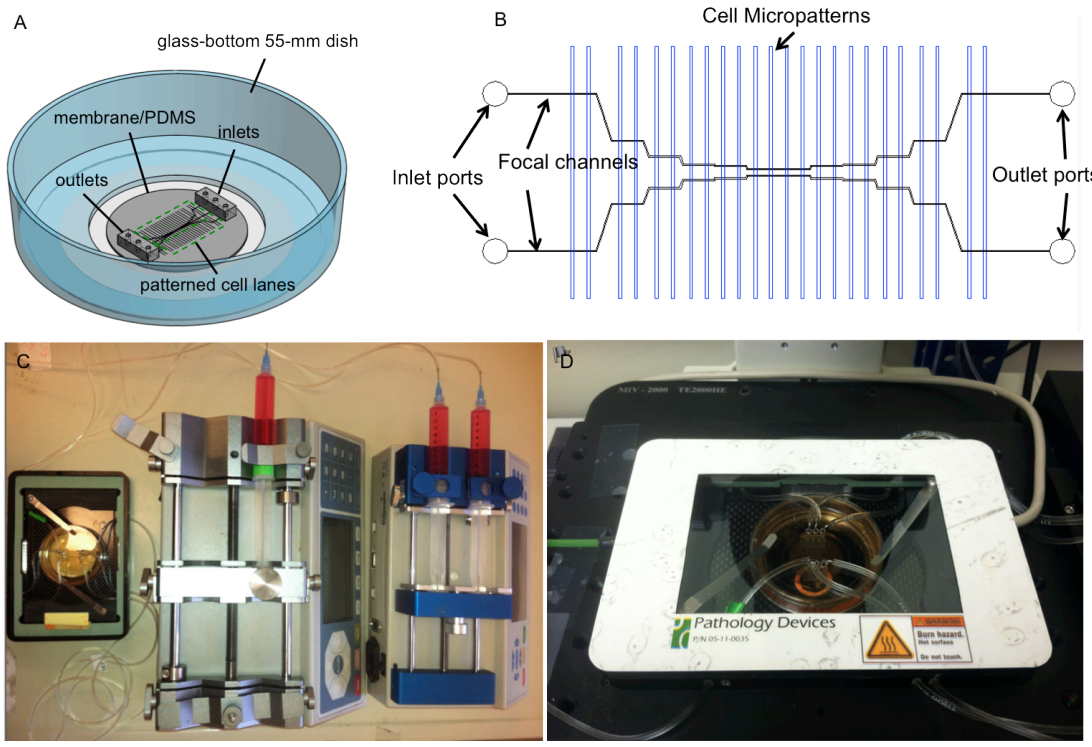

Figure 4.11: Flow-based basal-side channels focal stimulation device.

(A) An isometric schematic of the flow-based design. The device is embedded in a standard glass-bottom culture dish. (B) Top view of the device showing two independent microchannels (focal channels beneath a porous membrane flowing left to right) and orthogonal cell micropatterns (above the porous membrane). (C) The device can have multiple solution inputs connected at the inlet, delivered by one or more syringe pumps. The device is inside the petri dish on the microscope stage adaptor on the left. (D) The device within an on-stage incubator on a motorized microscope stage, where long-term (~24 hour) experiments can be programmed and automated.

4.5.2.1 Device fabrication and assembly

The device was fabricated using a combination of photolithography, soft lithography, and bonding techniques similar to those described for the Transwell device (Figure 4.12). Masters for microchannels (40 μm wide and 40 μm high), were fabricated in SU-8 using standard photolithography. PDMS replicas, which had the microchannel features were bonded to the glass bottom of a No.1 coverslip glass-bottom 55 mm petri

dish with the channels facing upwards. The thickness of the PDMS below the channels (between the channel floor and the glass) was 200 μm, defined by the spacer in the original master. The porous PET membrane was then bonded on top of the PDMS channels layer using the dipodal silane chemistry described in Section 4.3.2. PET membranes, cut out from Transwell inserts (1.0 μm pore diameter, 1.6 x 10^6 pores/cm^2, Corning), were modified by oxygen plasma (60W, 670 mtorr, 60 sec) and treated in bis[3-(trimethoxysilyl)propyl]amine solution for 20 min at 80°C then rinsed in IPA, dried, soaked in ethanol. The PDMS layer was modified by oxygen plasma (60W, 670 mTorr, 60 sec) and bonded to the ethanol-wetted membrane by conformal contact and heated to 70°C to complete bonding. The membrane regions connecting to the ports were punched out by tweezers. Subsequently, the inlet and outlet PDMS ports components (containing 1 mm diameter punched inlet and outlet holes) were aligned and bonded to the PET membranes using oxygen plasma treatment of both sides (60 W, 670 mTorr, 60 seconds).

For micropatterning, we used the fluorosilane-etching method described in **Chapter 3**. The PDMS micropatterning template channels defining the cell lanes can be easily aligned orthogonal to the microchannels. The same process of hydrophobic deposition of a fluorosilane, plasma etching, flow of dilute Matrigel, and adsorption of Pluronic F127 was used to define 40 μm wide cell lanes and 120 μm wide non-permissive regions.

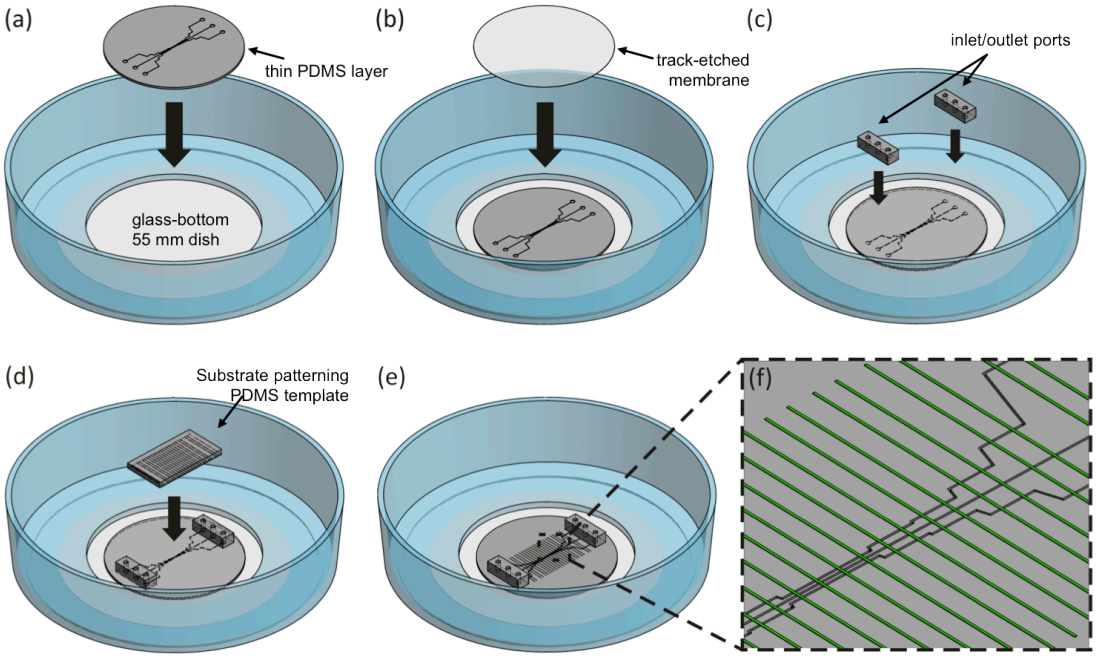

Figure 4.12: Device fabrication: basal-side channels device.

(A) A thin PDMS layer with channels is plasma bonded to the glass bottom dish, with the channels facing upwards. (B) A porous PET membrane is then bonded on top of the channels layer. (C) The membrane is punched at the inlets and outlets, and PDMS inlet and outlet ports (for tubing connections) are then aligned atop the membrane layer. (D) Micropatterning using the fluorosilane method: a patterning template with channels is aligned orthogonal to the fluidic channels. (E) and (F) The completed device with the fluidic microchannels underneath the porous membrane (black) and the orthogonal cell micropatterns on top (green). Figure credit: Christopher G. Sip.

4.5.2.2 Multiplexed delivery to micropatterned cells

In order to visualize two stimuli focally delivered to within close proximity of each other (within 200 μm), cytoplasmic fluorescent dyes of two colors CellTracker Green CMFDA and CellTracker Orange CMRA (Invitrogen) were applied at two inlet ports of the device. The CellTracker™ dyes are cell permeable molecules that undergo two intracellular reactions that: 1) renders it fluorescent by cleavage by nonspecific interacellular esterases, and 2) renders it cell impermeable by reaction with glutathione-S-

transferase. In Figure 4.13, we show focal delivery of CellTracker Green (GFP channel) and CellTracker Orange (Texas Red channel) onto micropatterned myoblasts for up to 2 hours. The two channels carrying dyes stained cells with distinct patterns with a separation distance of 200 μm and as close as 160 μm. In summary, we developed a method for multiplexed delivery of soluble factors using a basal-side channels alteration of the membrane-based focal delivery device described in the first part of this chapter.

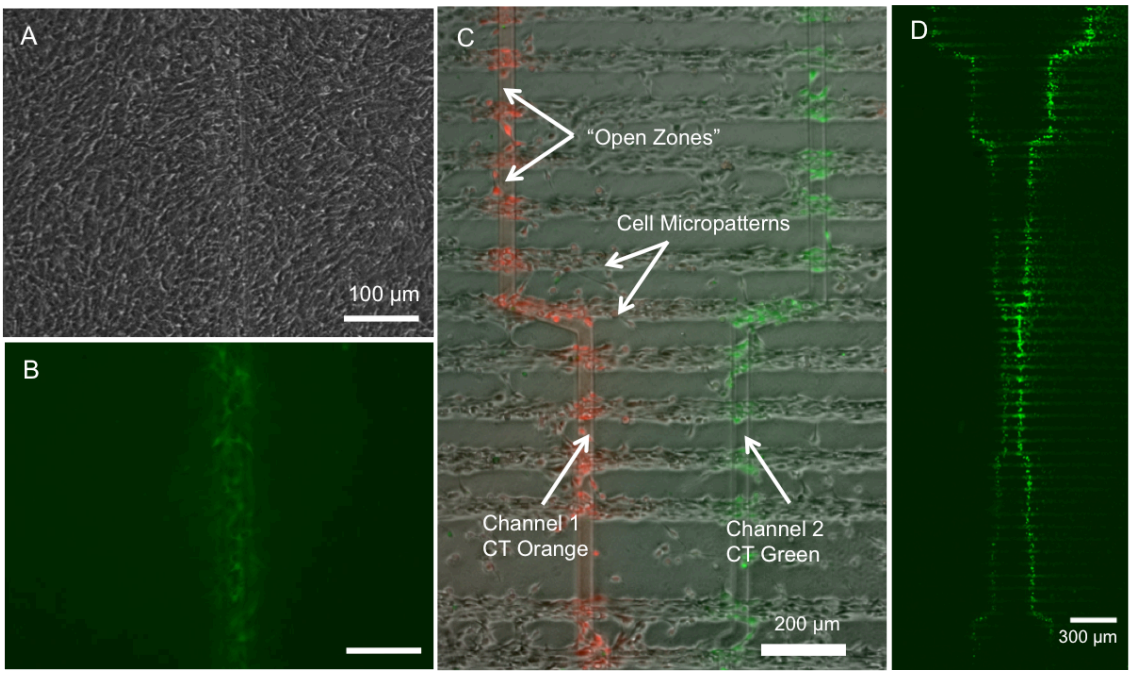

Figure 4.13: Focal delivery of multiple soluble factors using basal-side channels device.

(A) and (B) We first demonstrated that the channels could deliver factors (calcein AM) focally to a monolayer of C2C12 cells. (C) The left channel, delivering CellTracker Orange, and the right channel, delivering CellTracker Green focally stained orthogonally micropatterned C2C12 cells. The two channels carrying dyes stained cells with distinct patterns to within 160 μm (out of this field of view). (D) Delivery of a single dye, Calcein AM shows staining of micropatterned C2C12 cells follows the underlying channels pattern.

4.6 CONCLUSIONS

Porous membranes effectively allow the fluidic and substrate microenvironments to be compartmentalized, and enable basal-side focal delivery strategies. Combining the fluorosilane micropatterning method described in **Chapter 3**, and the membrane-based focal delivery method described in **Chapter 4**, we were able to construct well-defined, parallelized microenvironments. The system is contained within a user-friendly Transwell insert. Here, we showed spatial resolution as low as 20 μm, and sustainability of focal signal for up to 48 hours. We demonstrated proof-of-principle of regio-selective transfection of cell sheets, with broad potential applications. We also showed alternative modules of membrane-based delivery, including fabrication of user-defined membranes made of EPON 1002F photoresist, and delivery of multiple soluble factors through a flow-based basal-side channels device variant. Our next step was to adapt our Transwell system into a model for studying AChR clustering dynamics in cultured myotubes (**Chapter 5**). In our model, we will substitute the motor neuron with fluidic apertures that locally deliver neurochemicals to subcellular regions of cultured myotubes. Aperture sizes achievable using our fabrication technique were appropriate for targeting AChR pretzels, which are on the order of 25-50 μm.

CHAPTER 5: EFFECTS OF FOCAL AGRIN ON ACETYLCHOLINE RECEPTOR CLUSTERING DYNAMICS

5.1 SUMMARY

As a proof-of-concept, we adapted the modified Transwell insert device described in **Chapter 4** into an *in vitro* platform for high throughput studies of NMJ biology. In our model, apertures serve as *de facto* motor neurons that deliver neurochemicals of interest, e.g. agrin, to subcellular portions of myotubes. We successfully demonstrated focal delivery of agrin, which elicited a localized AChR clustering response. Moreover, we studied the metabolic stability of AChR "pretzel" clusters using live-cell timelapse microscopy on our device.

5.2 INTRODUCTION

The motor neuron regulates the neuromuscular junction's postsynaptic AChR density through a set of positive and negative factors, most notably agrin and acetylcholine. Historically, the "agrin hypothesis" stated that agrin was the master initiator of AChR clustering at developing NMJs. Indeed, agrin has been shown to directly induce formation of AChR microclusters at the site of focal application both *in vitro* [45, 46] and *in vivo* [14, 15, 43]. However, the agrin hypothesis was challenged by the discovery of prepatterned aneural AChRs in early development. A new theory stated that agrin may additionally act as an AChR stabilizer and anti-declustering factor [20]. The role of agrin as a metabolic stabilizer of AChR is more controversial, suggested by the following evidence: 1) agrin expression *in vivo* is limited to the basal lamina of the synaptic cleft [12, 152]; 2) *in vivo* experiments have shown that agrin-predating

protosynaptic clusters are eventually stabilized by the axon that "finds" it, suggesting that AChR cluster stabilization is neuron (agrin)-dependent [27]; 3) regenerating motor axons form synapses specifically at those sites where a synapse had previously existed, even if the muscle fiber was degenerated, suggesting the basal lamina, which includes agrin, has a stabilizing, "anchoring" role in the synapse's location [8]; 4) experiments with agrin knockout mice suggest agrin is continuously needed throughout adult life to maintain stable localized synaptic AChRs [26]; 5) neural agrin injections into rat muscles increased AChR half-life in a dose-dependent manner [28]; and most recently, 6) agrin plays a major role in the recycling of internalized AChRs back into the NMJ [153].

Although these *in vivo* results suggest that agrin is an AChR stabilizer, very few studies [29] have been able to directly prove this hypothesis in cell culture models, possibly due to the difficulty in *in vitro* experiments to apply agrin focally onto pre-existing AChR pretzels. Indeed, there is a discrepancy between the effects of bath versus focal applied agrin in cell culture studies: bath agrin caused faster depletion of AChRs in pre-existing laminin-induced AChR pretzels and formation of random AChR microclusters throughout the myotube surface [10], while focal agrin upon AChR pretzels caused *stabilization*, decreasing their rate of degradation relative to untreated pretzels on the same myotube, as well as localized microclustering [29]. Which is the "correct" physiological result? We sought to reconcile these disparate results by building an *in vitro* system that provides comparable conditions for bath and focal agrin application. We hypothesized that agrin is both a locally acting AChR cluster inducer *and* AChR pretzel stabilizer.

5.2.1 Hypotheses and objectives

We tested two hypotheses: that focal agrin delivery would 1) result in localized AChR microclustering, and 2) increase stability of pre-existing pretzels. In our model, we substituted the motor neuron with apertures that locally deliver neurochemicals to subcellular regions of cultured myotubes. Our goal was to study the dynamics and spatial patterns of AChR clustering upon focal application of agrin. Our strategy was to apply the neurochemicals, i.e. agrin, onto cultured myotubes from the basal side using the modified Transwell devices described in **Chapter 4**. These devices, which feature large arrays of apertures directed to subcellular regions of micropatterned myotubes, enabled precise, high-throughput readouts of AChR events, providing statistically rich data on how agrin works to shape the NMJ.

Applying soluble neurochemicals from the myotube's basal side via passive diffusion rather than flow may be a more physiological mimic of the *in vivo* NMJ, where neurotransmitters are released into the synaptic cleft and travel very short distances between cells (~ 20 nm) by diffusion to their target receptors. Agrin is presented as a substrate-bound molecule on the basal lamina *in vivo*. Since our experiments required temporal control of agrin application (ability to add or remove agrin signal), we used soluble C-terminal agrin, an established reagent for *in vitro* NMJ experiments. Another advantage of basal-side delivery is that AChR clusters are localized to the myotube ventral (basal) side, to areas of cell-substrate contact [154], which enabled our devices to directly stimulate the AChR pretzels from underneath, as opposed to apical side application. Therefore, we expected that basal side agrin delivery would result in the same or even a potentiated effect relative to apical side application.

5.3 MATERIALS AND METHODS

5.3.1 Device design, fabrication and operation

The modified Transwell device was fabricated similarly to the methods described in **Chapter 4**, utilizing a 0.4 μm microporous membrane (0.4 μm pore diameter, 2.0 x 10^6 pores/cm^2). The device was reconfigured to a 6 x 36 array (216 total) of 40 μm diameter apertures. This high throughput design was made in consideration of multiple constraints. To generate a large number of independent samples within each device, each field of view (FOV) would be centered on an aperture with overlying micropatterned myotubes aligned in the x-direction. A stitched image containing the length of myotubes could be easily tracked in timelapse microscopy. Since C2C12-derived myotubes in culture are ~ 500 μm to 2000 μm long, apertures were spaced apart by 2 mm such that a given myotube would receive either one or no focal stimulus. This configuration would avoid confounding effects from multiple competing agrin sources within the same myotube. To maximize the number of myotubes per experiment given the available cell culture surface area of the Transwell device, myotube microtracks were separated by 200 μm, a distance at which there would reliably be no bridging of cells between tracks. Moreover, to ensure that myotube microtracks would cover apertures to prevent stimulant leakage, 120 μm wide microtracks were registered overlying the 40 μm apertures. The size of aperture, 40 μm, was chosen because the targets of focal stimulation, AChR pretzels, are ~ 20 – 40 μm across *in vitro* [23]. Although, 120 μm wide myotube microtracks often resulted in multiple parallel myotubes within microtracks (Figure 5.1B), it was straightforward to analyze such myotubes.

For all focal stimulation experiments, 600 μL of stimulant (e.g. agrin) diluted in Fluorobrite™ DMEM differentiation medium was added to the basal (upper)

compartment, while 1.2 mL of differentiation medium was added to the apical (lower) compartment. Transwell devices were imaged using glass-bottom 6-well plates to minimize autofluorescence (#1 coverslip bottom, In Vitro Scientific, #P06-20-1N).

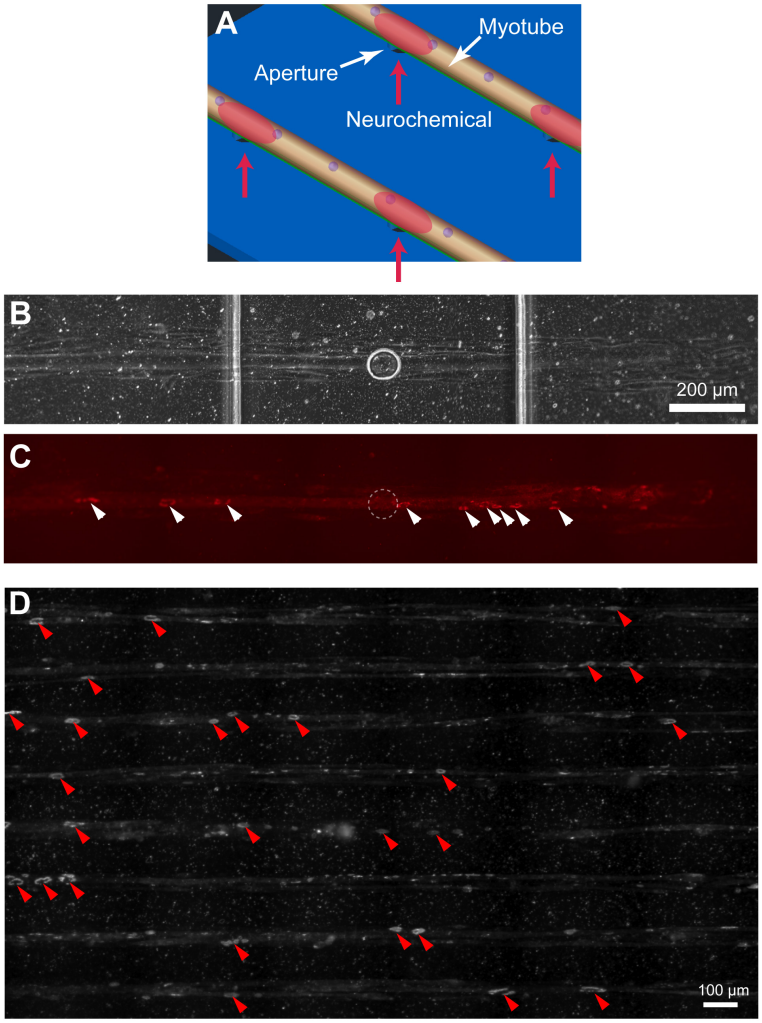

Figure 5.1: Schematic of focal neurochemical stimulation using modified Transwell apertures device.

(A) An isometric 3D rendering of two mature myotubes grown on Matrigel microtracks. Apertures direct neurochemical stimuli focally to the basal side of subcellular portions of the myotubes. (B) Phase contrast micrograph showing a standard field of view of experiments showing micropatterned myotubes overlying an aperture. Note that there are multiple myotubes in parallel, but their cell boundaries are distinct. (C) Fluorescence (Texas Red) micrograph showing bungarotoxin-labeled AChR clusters, with large distinct AChR pretzels shown by red arrowheads. (D) Large stitched fluorescent micrograph showing an array of micropatterned myotubes on a modified Transwell device expressing AChR pretzels shown by red arrowheads.

5.3.2 Cell culture

The myoblast cell line C2C12 derived from *Mus musculus* (ATCC #CRL-1772) was used to generate myotubes for our NMJ model. For expansion of myoblasts, cells were cultured on 100 mm petri dishes coated with 0.1% gelatin (Sigma-Aldrich #G1393) and grown with DMEM (Invitrogen, Gibco #11995) supplemented with 20% v/v fetal bovine serum, 1% v/v penicillin/streptomycin (Invitrogen, Gibco # 15140-122). Cells were passaged before reaching 70-80% confluence to prevent differentiation. When myoblasts were confluent, growth medium was switched to differentiation medium (DM): DMEM, supplemented with 2% v/v horse serum 1% v/v penicillin/streptomycin to induce differentiation into myotubes. DM was replenished every 2 days until Days 6-10, when myotubes were used for experiments.

5.3.3 Reagents

Recombinant rat agrin C-terminal fragment was purchased from R&D Systems, Minneapolis, MN, # 550-AG-100. For live cell fluorescence microscopy, myotubes were kept in Fluorobrite™ DMEM (Life Technologies, #A1896701) to minimize background fluorescence, supplemented with 2% v/v horse serum 1% v/v penicillin/streptomycin. Fluorescently-labeled α-bungarotoxin conjugates, coupled with Alexa Fluor 488, 594, and 647 (Life Technologies #B13422, B13423, and B35450), were used to label AChR clusters. Similar to experiments in **Chapter 4**, calcein and wheat germ agglutinin (WGA) were used at the end of experiments to ensure that apertures were functional and as a molecular tracer of agrin transport through apertures to sub-cellular regions of myotubes.

5.3.4 Imaging of AChR clusters

Microscope images were acquired using a Nikon Eclipse Ti model inverted microscope with a Nikon S Plan Fluor EL WD 20X / 0.45NA objective, fluorescence

filter turrets, automated translational stage, and z-positioner (Nikon Instruments, Melville, NY) with a 12-bit cooled CCD camera (ORCA-ER, Hamamatsu, Japan). Phase contrast and fluorescence images were stitched using the Nikon Elements software large image ND Acquisition feature. Using the Nikon Elements well-plate macro function, the regularly spaced apertures were assigned XYZ coordinates such that the same fields of view could be tracked in timelapse acquisitions. Due to slight unevenness of the membrane surface due to fabrication limitations, we used the Nikon Elements adaptive autofocusing method with a 50 μm coarse focusing step and 2 μm fine focusing step at every X-Y position to acquire in-focus images in every channel.

Each image tile was acquired at a resolution of 591 x 512 pixels at 2 x 2 binning (396.9 x 343.6 μm). Fluorescence images were acquired in 12-bit grayscale and stored as 16-bit ND2 and/or TIFF files. Apertures were spaced 1 mm apart so that a 5 x 1 stitched image produced a field of view covering 1984.6 x 343.6 μm, or roughly from halfway to the left neighboring aperture to halfway to the right neighboring aperture. This acquisition protocol allowed the entire field of view from closest (proximal) to farthest (distal) from the stimulation source to be imaged, leaving no part of the area of interest of the device unscanned.

5.3.5 Experimental design

To study AChR clustering dynamics in response to bath and focal agrin application, we followed an experimental scheme shown in Figure 5.2. At days 6 – 8 of culture, C2C12-derived myotubes were first incubated with BTX-Alexa Fluor 594 (1.5 mL in each compartment, 5 μg/mL, 1 h), and washed gently three times with differentiation media. The entire device was imaged in phase contrast and Texas Red (Alexa Fluor 594) fluorescence channels at an initial T0 timepoint. Agrin was then

applied on the basal side through apertures (555 nM) for focal experiments, and the apical side (100 nM) for positive control experiments for 1 h, and washed. The myotubes were incubated in a different color bungarotoxin, BTX-Alexa Fluor 647 (1.5 mL in each compartment, 5 μg/mL, 1 h) to label new AChR insertions since the agrin treatment, and washed. From 2 h to 8 h, in 2 h intervals, 4 additional images (T1, T2, T3, T4), of the same fields of view as T0, were taken in phase contrast, Texas Red, and Cy5 (Alexa Fluor 647) channels.

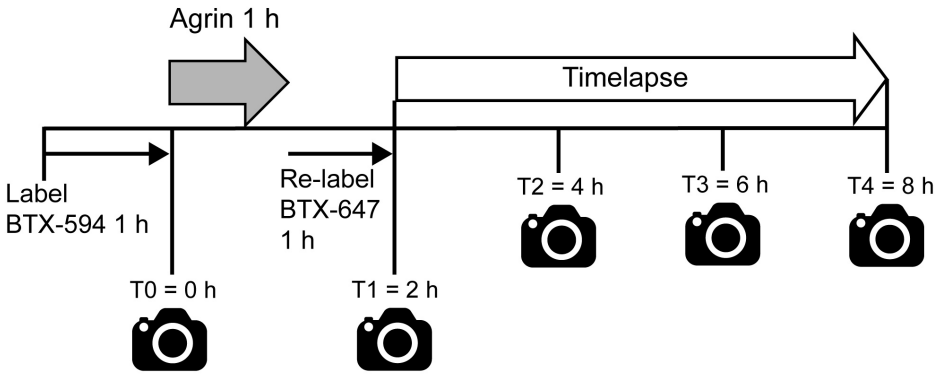

Figure 5.2: Experimental design.

5.3.6 Quantitative image analysis of AChR microclusters and AChR pretzel stability

Image analysis was performed using Fiji (ImageJ) software (NIH). The image processing workflow is shown in Figure 5.3. Because of the long duration of acquisitions due to autofocusing at every aperture position (i.e. ~ 2 hours per timepoint), depending on the experiment, a fraction of the 216 apertures were imaged. The initial fluorescence images in Texas Red and Cy5 were flatfield corrected to adjust for uneven illumination in the fields of view. A background image taken of a part of the device devoid of cells was subtracted from the image of interest to create a flatfield corrected image.

For AChR microclustering analysis, the T0 Texas Red (first label) image and the T1 Cy5 (second label) image were thresholded by intensity (a fixed intensity level determined by microcluster thresholding in a bath control experiment) to generate a binary black and white image. The particles were then defined as AChR microclusters if they were within the range 5 – 250 μm^2 in area. The microcluster centroid positions were recorded and a distance, R, to the nearest aperture center was calculated.

For analysis of AChR pretzel stability, corrected T1 – T4 Texas Red and Cy5 fluorescence images were manually segmented for AChR pretzels. AChR pretzels were identified by the user based on a size threshold (greater than 250 μm^2) and morphology (typically an open elliptical shape). AChR pretzel regions of interest (ROIs) were recorded for mean fluorescence intensity and centroid (XY) position, from which a distance R from the aperture was calculated. The intensities of AChR pretzels were assumed to decay exponentially. The AChR pretzel mean intensities were plotted versus time and fitted to an exponential function of the form: $I = I_0 \exp\left(-\frac{t}{\tau}\right)$, where I is the mean intensity at any given timepoint, I_0 is the initial mean intensity, t is the time (h), and τ is the time constant. A larger τ would imply a more stable AChR pretzel.

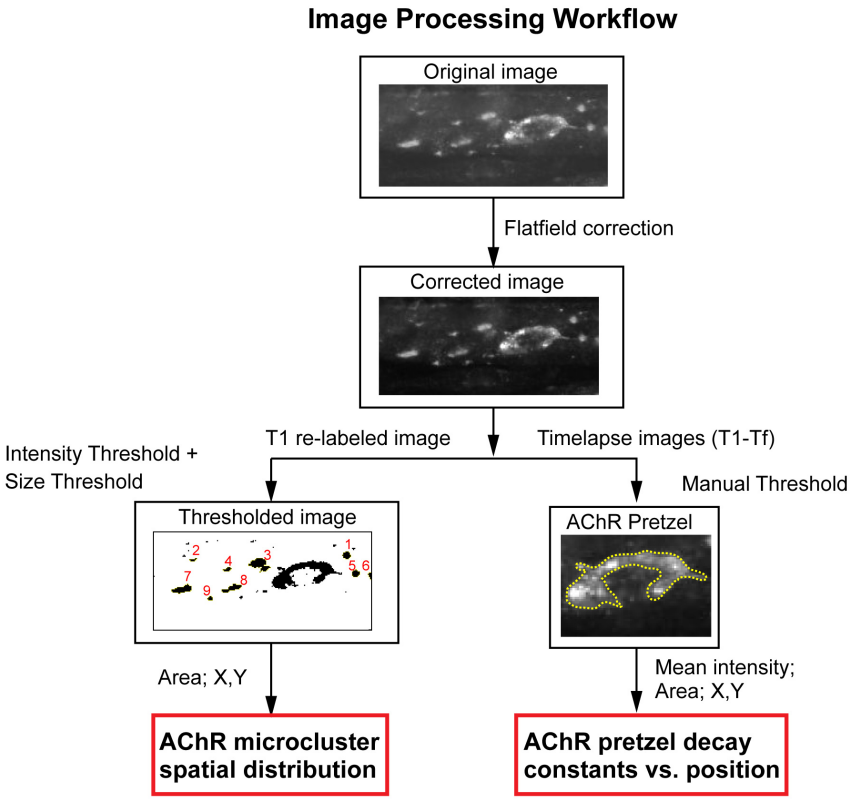

Figure 5.3: Image processing workflow.

5.4 RESULTS

5.4.1 Modified Transwell microfluidic platform suitable for AChR microscopy

Our foremost goal was to assess the feasibility of our modified Transwell platform for 1) viability of myotubes, and 2) feasibility for quantitative fluorescence imaging of AChR microclusters and pretzels. Myotubes exhibited high viability as indicated by spontaneous twitching. Micropatterned myotube microtracks were coated with Matrigel, a protein extract from Engelbreth-Holm-Swarm mouse sarcoma cells that resembles the extracellular matrix of muscle. Notably, Matrigel, which consists of ~ 60% laminin, has been shown to induce aneural AChR pretzels [29]. To the best of our

knowledge, few studies have performed live cell microscopy of AChRs on myotubes on Transwell porous membranes. Bungarotoxin-labeled AChRs showed a high signal-to-noise ratio when grown on 0.4 μm membranes. We noted that 0.4 μm microporous membranes gave much better optical clarity than 1.0 μm membranes, which showed considerable speckle noise due to the larger pore size. In micropatterned myotubes, the density of AChR pretzels was highly random. A cursory analysis of AChR pretzel density per unit length of myotube was on the order of 1 pretzel per 300 μm. Notably, lower passage C2C12 myoblasts, i.e. under passage 10, yielded myotubes with much more dense AChR pretzels, presumably due to the increasing number of differentiation defective myoblasts that accumulate in higher passage numbers.

5.4.2 Agrin transport through porous membranes induces AChR microclustering

In an initial set of control experiments, we aimed to show that myotubes would respond similarly when stimulated with agrin either from the apical side (bath positive control) or through a porous membrane from the basal side. Here, we prepared a batch of modified Transwell devices with large 11.6 mm x 11.6 mm holes in a PDMS stencil layer instead of apertures. The goal was to observe whether agrin would induce the same type of global AChR clustering when passed through the large holes and membrane onto the basal side of myotubes as observed from apical bath application. For validation, these devices were fabricated using the same assembly and bonding methods as aperture devices. Non-patterned myotubes were grown on Matrigel-coated modified Transwells, differentiated until day 8, and three conditions were tested: 1) negative control, with no agrin treatment, 2) positive control, with apical side agrin application, and 3) basal side agrin application through the large hole and porous membrane. Myotubes were initially labeled with BTX-594 for 1 h, imaged, treated with 100 nM agrin for 18 h, then re-

labeled with BTX-647, and re-imaged for newly formed AChR clusters. Microclusters per myotube were counted and a Student's t-test was performed between groups to determine statistical significance. Negative controls showed a slight, but not significant increase in AChR microclusters. Both apical and basal side application showed statistically significant ($p < 0.01$) global increases in AChR microclusters at 18 h compared to 0 h. There was no statistical difference between the mean AChR microcluster count of the apical and basal groups. Together, these results showed that similar AChR clustering responses occur from global agrin application from either the apical side or basal side through a porous membrane.

These experiments addressed the potential pitfall that soluble agrin would adsorb, specifically or nonspecifically, onto the PET membranes before reaching myotubes, sequestering its activity. The membrane pores are coated with Matrigel, consisting of 60% laminin. The specific binding mechanism of agrin to laminin occurs through the interaction between 130 amino acids on agrin's N-terminus and laminin-1 in Matrigel [155]. The active C-terminal agrin fragment, which does not contain the 130 amino acids on the N-terminus, used *in vitro* contains four EGF-like repeats and three-laminin-like G domains [156]. It is not known whether any of these motifs will bind to Matrigel specifically. Previous studies have not reported difficulty with agrin sequestration in the presence of laminin or Matrigel-coated cell cultures. However, our device operates in a different format in that agrin encounters the Matrigel-coated porous membrane from the basal side before reaching cells. More likely than specific binding, agrin may nonspecifically adsorb to the pores. Here, since there was no difference in AChR clustering response between apical and basal side application through the membrane, we can assume there was negligible agrin adsorption. However, as we will discuss in the next

section, a local AChR clustering response through 40 μm apertures required a much higher agrin dose (555 nM) than bath applications, suggesting possible agrin adsorption.

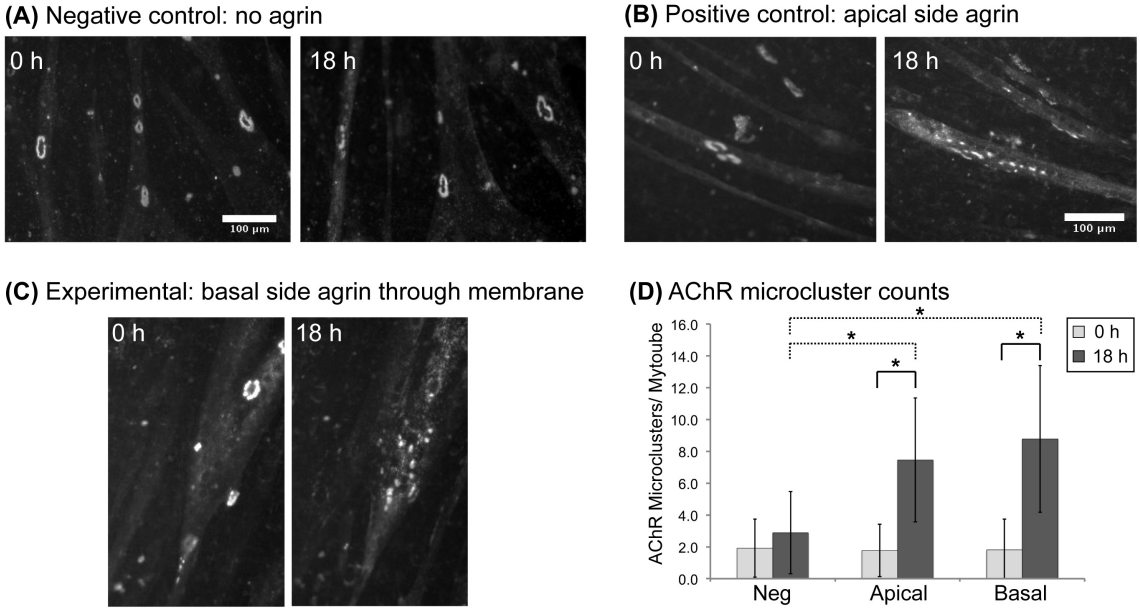

Figure 5.4: Control agrin application experiments through porous membranes

Myotubes cultured on a modified Transwell device with large 11.6 mm x 11.6 mm holes on a PDMS stencil. The same field of view was imaged at 0 h and after 18 h of agrin application and re-labeling with BTX-594. (A) A negative control condition with no application of agrin shows no significant increase of AChR microclusters after 18 h. (B) A positive control condition in which agrin was applied on the apical side of myotubes shows significant increase of microclusters (D) after 18 h. (C) An experimental condition in which agrin was applied onto the basal side of myotubes through apertures and porous membrane shows formation of new AChR microclusters throughout the myotube surface as well as the disintegration of an existing AChR pretzel after 18 h. (D) AChR microcluster counts per myotube before (0 h) and after agrin application (18 h). Error bars represent standard deviation, * indicates statistical significance $p < 0.01$ between groups.

5.4.3 Focal agrin induces localized formation of AChR microclusters

Here, we demonstrate an approach to test the hypothesis that focal delivery of agrin to subcellular sections of myotubes induces the recruitment and aggregation of

AChRs to those areas. Following the experimental design shown in Figure 5.2, we pre-labeled myotubes with BTX-594 to visualize the initial AChR clusters, applied agrin focally through apertures for 1 h, re-labeled with a second color, BTX-647 to visualize the newly formed AChR clusters. One hour was chosen as the duration of agrin application because we wanted to limit diffusive broadening of the focal signal (see **Chapter 4**) and was a duration shown to be sufficient for induction of both local and bath AChR microclusters [46, 157]. Figure 5.5 shows a representative example of localized AChR microcluster induction from agrin focal application. Figure 5.5 shows a standard acquisition, a 5 x 1 stitched image of micropatterned myotubes, which were locally exposed to agrin in the center of the image through 40 μm apertures. The T1 BTX-594 image (Texas Red channel in red) shows the first label, with AChR clusters homogeneously distributed throughout the myotubes (Figure 5.5A). In contrast, the T1 BTX-647 image (Cy5 channel in magenta) shows the second label, with AChR clusters preferentially distributed near the apertures (Figure 5.5A). To define microclusters, images were thresholded into binary images and filtered for particle sizes 5 – 250 μm^2 in area. We observed an overall increase in AChR microclusters from the first to the second label, and especially in regions near the apertures. In Figure 5.5B, we show representative regions "proximal" directly overlying the aperture, and "distal", 900 μm from the aperture. Comparing the two regions in the BTX-647 images, the proximal regions have a markedly higher total number of microclusters, as well as a higher increase in clusters when comparing the BTX-594 to the BTX-647. Furthermore, when we compare the proximal T0 BTX-594 and T1 BTX-647 images, we see an even more dramatic difference in AChR microcluster counts near the aperture. The proximal T0 BTX-594 image shows very few AChR microclusters before agrin application. We surmise that the difference between the T1 and the T0 BTX-594 images is due to the presence of trace

amounts of residual bungarotoxin remaining from the first labeling during the agrin application, which co-labeled the newly inserted microclusters along with BTX-647 [10]. The clustering trends are quantitatively represented in the spatial distribution histogram shown in Figure 5.5C, which shows the microcluster count in the x-direction, from 0 to 1980 μm in 180 μm wide bins. Prior to agrin application, we see an initial spatially homogeneous distribution of 32 total microclusters with BTX-594 (red bars). After agrin application, and re-labeling with BTX-647, we see an overall increase to 103 total microclusters, with a greater number of clusters concentrated near the aperture (magenta bars).

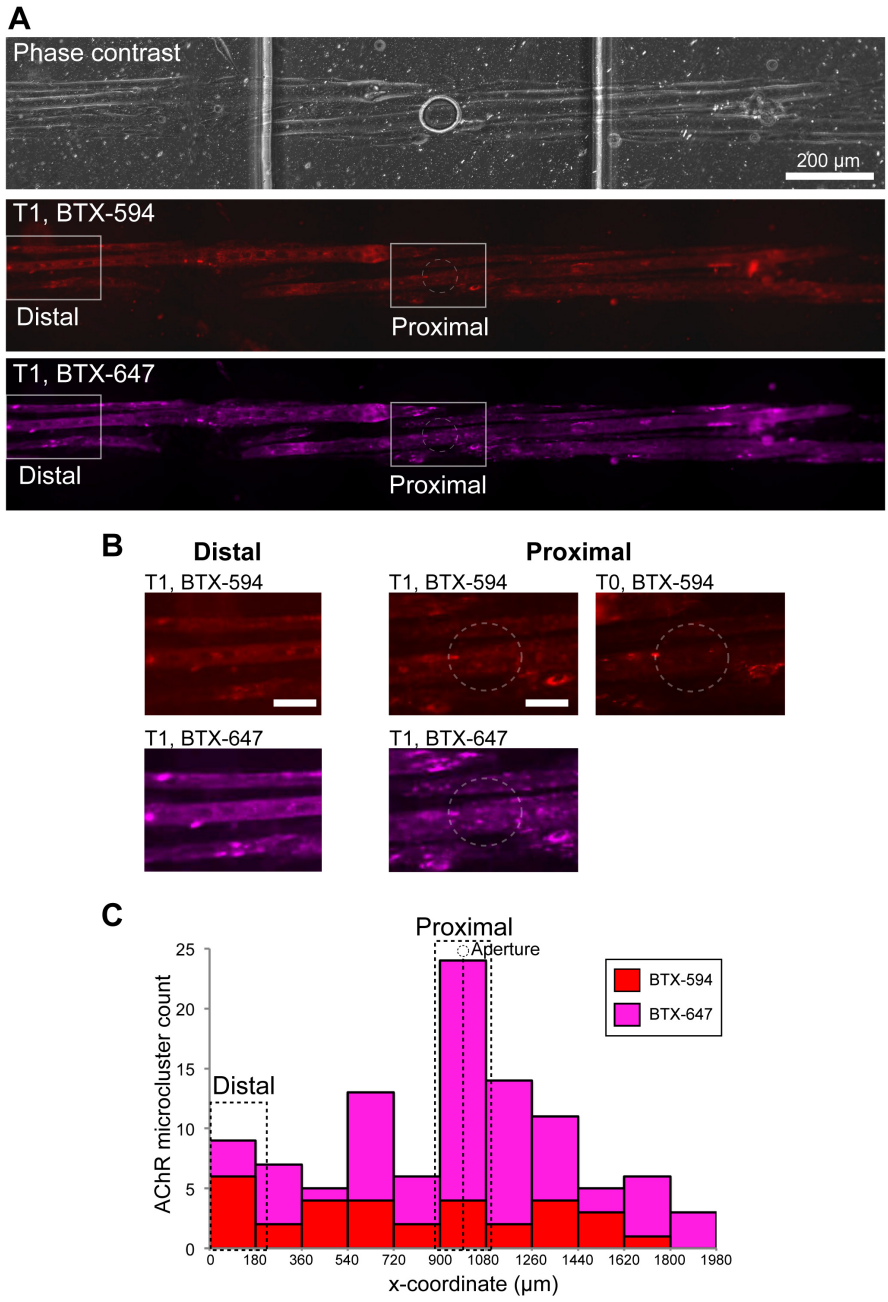

Figure 5.5: Localized formation of AChR microclusters in micropatterned myotubes.

Focal delivery of agrin through apertures resulted in localized formation of AChR microclusters. (A) A single field of view (phase contrast image) showing multiple parallel micropatterned myotubes on a modified Transwell device overlying a 40 µm aperture. The corresponding fluorescence image in Texas Red channel shows the first label of AChR clusters with BTX-594. Note the diffuse, random pattern of

AChR microclusters homogeneously distributed throughout the myotubes. The corresponding fluorescence image in Cy5 channel shows the second label of AChR with BTX-647. Note the aggregation of newly formed AChR microclusters in the middle of the image centered around the aperture (dotted circle). (B) High magnification views of (A) shows a higher number of new AChR microclusters centered around the aperture in the "proximal" region marked by the second label, BTX-647 (E) compared to the "distal" region. Scalebar = 50 μm. (C) Spatial distribution of the original (first label, BTX-594, red) and newly formed (second label, BTX-647, magenta) AChR microclusters shows a marked increase in newly formed clusters in the center around the aperture.

Our microfluidic platform allowed us to acquire large sample sizes per experiment. For example, in the microclustering experiment, 75 usable fields of view were acquired from a device with 216 apertures. Images were discarded based on the following criteria: 1) if any of the T0 and T1 images were out of focus, 2) if there was less than 50% cell coverage of the aperture, 3) if most of the micropattern consisted of unfused myoblasts instead of myotubes, or 4) if there was a large number of dead cells. Cumulatively from the 75 images, we observed localized AChR microclustering concentrated near the aperture center. Figure 5.6A shows the spatial distribution histogram of all AChR microclusters from the 75 fields of view plotted as a function of the image x-coordinate. There was an increase in the total number of microclusters from the first label (2152) to the second label (3980). Typically, the microclusters initially present would get re-labeled by the second label, such that the total BTX-647 microcluster count included both the newly inserted microclusters *and* the old microclusters. Therefore, the BTX-647 counts were almost always greater than the BTX-594 counts, and in the histograms, are shown as bars overlaid behind the BTX-594 bars. Figure 5.6B shows the increase of AChR microclusters, which was taken as the difference between BTX-647 and BTX-594 microcluster counts. Notably, the increase in AChR microclusters was greatest in the central 900 – 1080 μm bin overlapping with the aperture. Cumulatively, the percentage microclusters in the 900 – 1080 μm bin out of the

total microcluster count increased from 12.3 % in the BTX-594 image to 16.9 % in the BTX-594 image (9.1% represents a perfectly homogenous distribution).

When the two populations of microclusters were plotted as a cumulative distribution function of radial distance from aperture (Figure 5.6**C**), we observed a leftward shift in the distribution from BTX-594 to BTX-647, towards the aperture center. The median, mean position R and standard error of the mean shifted from 468 μm and 477 $\pm$ 6 μm in the BTX-594 group to 409 μm and 434 $\pm$ 5 μm in the BTX-647 group. For comparison, a perfectly homogeneous microcluser distribution would have a median and mean radial distance of 495 μm. To determine statistical significance for differences in the mean position R of old (BTX-594) versus new (BTX-647) AChR microclusters, a Kolmogorov-Smirnov two sample test was performed with the null hypothesis that the two populations of microclusters had the same distributions. The two populations were determined to be statistically significantly different ($p < 0.001$).

We demonstrated reproducibility of the microfluidic platform to induce local AChR microclustering non-patterned myotubes over 40 μm apertures (Figure 5.7). We again observed localized AChR microclustering centered around apertures (Figure 5.7A), and much less obvious clustering in "distal" regions, e.g. 230 μm away from aperture center (Figure 5.7B).

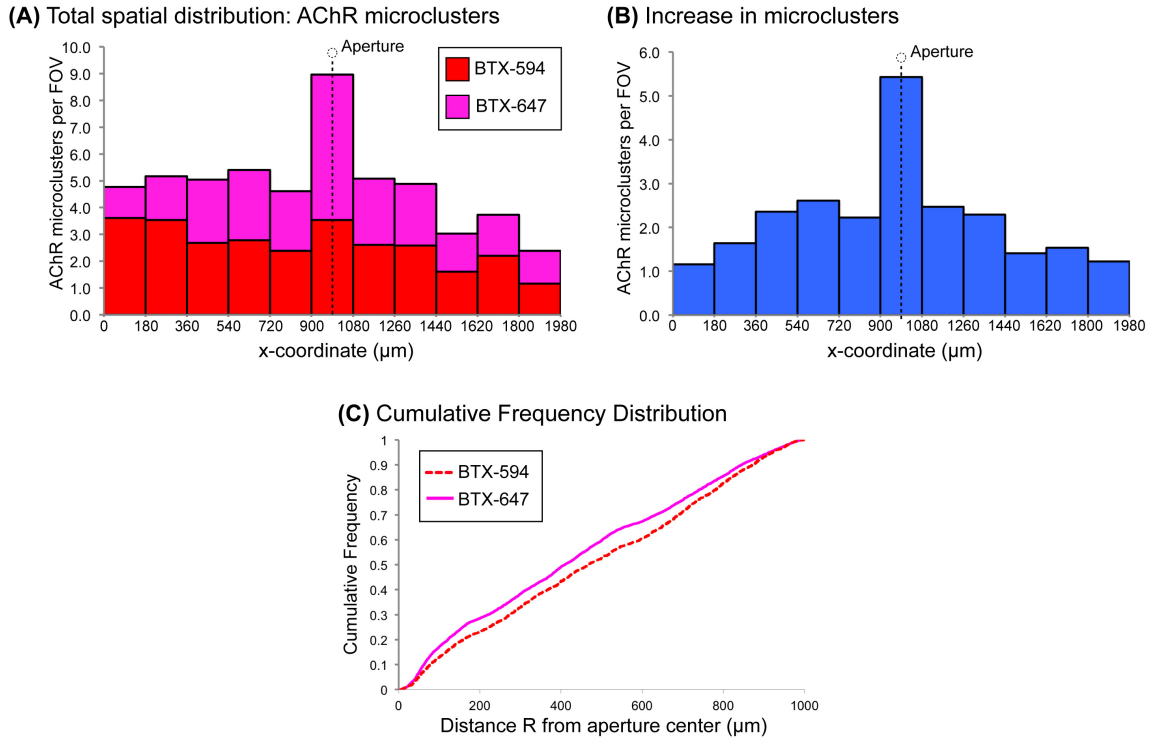

Figure 5.6: Cumulative AChR spatial distribution in micropatterned myotubes.

(A) Cumulative spatial distribution of original (first label, BTX-594) and newly formed (second label, BTX-647) AChR microclusters is plotted as a histogram with 100 µm bins. The AChR cluster count per field of view is plotted against the radial distance from the aperture center. Note the marked increase in newly formed microclusters centered near the aperture on the left of the histogram due to focal agrin application. (B) The data plotted as a cumulative frequency distribution. Note the leftward shift of the dotted line (BTX-594) compared to the solid line (BTX-647), indicating a shift of the overall distribution of AChR microclusters to closer to the aperture after agrin application. The distributions were determined to be statistically different ($p<0.001$) using a Kolmogorov-Smirnov two sample test.

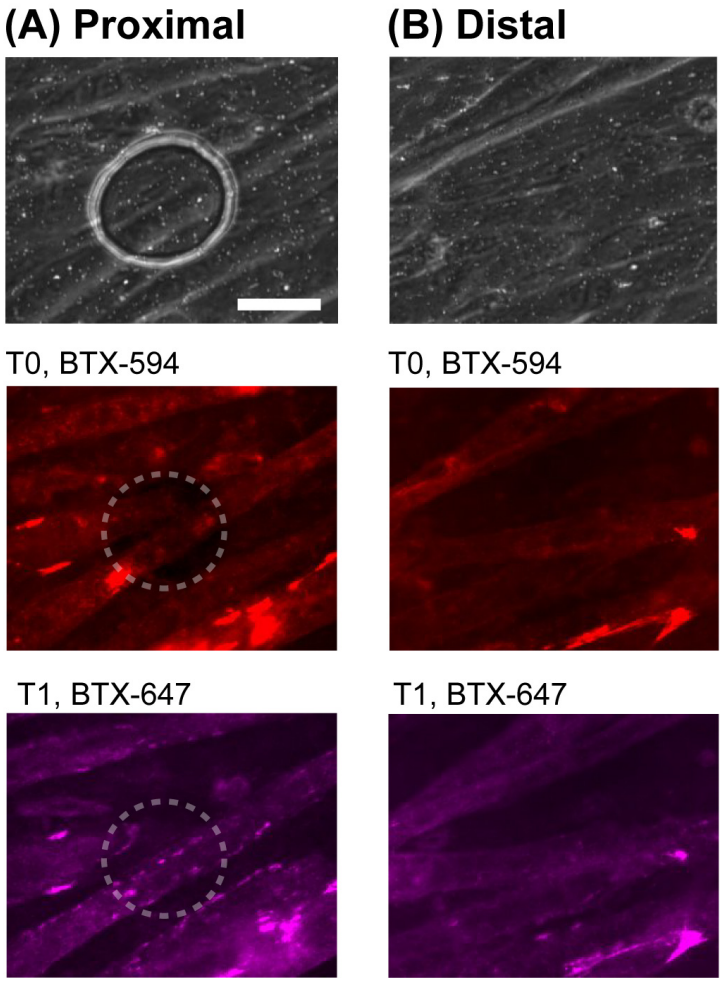

Figure 5.7: Localized formation of AChR microclusters in non-patterned myotubes.

(A) Representative high magnification view of myotubes overlying a 40 μm aperture. Note that in the T0 BTX-594 image, there are nearly no AChR microclusters overlying the aperture, while in the T1 BTX-647 image after agrin focal application, there are newly formed microclusters over and adjacent to the aperture. (B) Representative high magnification view of myotubes "distal" or centered 230 μm away from the aperture center. Note that there is a negligible change in the number of microclusters between the T0 BTX-594 and T1 BTX-647 images. Scalebar = 50 μm.

5.4.4 AChR pretzel stability is independent of local agrin concentration

To measure the stability of pre-existing AChR pretzels, we observed their rate of fluorescence decay in response to agrin stimulation using timelapse microscopy.

Traditionally, in both *in vivo* and *in vitro* experiments, AChR cluster stability was measured using radio-labeled (I^{125}-BTX) bungarotoxin, estimating the half-life of AChRs from the amount of radioactivity released into the media as a fraction of the amount of initial radioactivity [158]. However, these assays can only provide an estimate of total receptor half-lives pooled from the entire cell culture dish, but cannot spatially distinguish individual AChR stabilities. We used an assay to estimate acetylcholine receptor half-life based on the decay of fluorescence intensity of bungarotoxin-labeled receptors [10, 159]. Fluorescently-labeled AChR pretzels on micropatterned myotubes were identified by size and morphology, manually segmented, and their intensities were plotted versus time. The data was fitted to an equation of the exponential form $I = I_0 \exp\left(-\frac{t}{\tau}\right)$, where we derived the time constant, τ. The half-life $t_{1/2}$ of the AChR pretzel can be calculated from the time constant, τ by the equation $t_{1/2} = \tau \ln(2)$. We inferred AChR pretzel stability from the magnitude of τ, estimating that pretzels with longer time constants were more stable. For 61 AChR pretzels, the average and standard deviation of the R-squared correlation coefficient of the exponential curve fit was 0.969 ± 0.042 and 0.968 ± 0.028, respectively for BTX-594 and BTX-647. The correlation showed a high level of goodness of fit, assuring us that our method for extracting pretzel lifetimes from exponential decay timelapse data was sound.

We tested the hypothesis that agrin, which is delivered in higher doses closer to the apertures, would slow the decay of AChR pretzels. Figure 5.8A shows representative images of pretzel stability analysis. In the BTX-594 (red)-labeled image, we identified three AChR pretzels, numbered 1, 2 and 3, on two parallel myotubes near an aperture. Note that AChR pretzel 2 is directly overlapping with the aperture. In the BTX-647 (magenta)-labeled image at 2 h (after 1 h focal agrin application), note the appearance of

AChR microclusters, marked by white arrowheads, surrounding the larger pretzels. Moreover, the 2 hour BTX-647 image indicates that receptors were preferentially removed from the center of the pretzel and new receptors were added on the periphery. Figure 5.8B shows timelapse fluorescence micrographs of the three pretzels and their decay from 2 to 8 hours, along with fitted exponential decay curves. Although not obvious from observation, pretzel 2 showed the fastest rate of decay (τ = 1.92 h), while pretzel 1 (τ = 3.53 h) and pretzel 3 (τ = 2.65 h) showed slower decay. We note that random regions on myotube surfaces without visible AChR clusters were also measured for fluorescence decay. These regions also showed decay, but to a considerably lesser degree, i.e. 20% of the AChR pretzel decay, which assured us that AChR pretzel decay was legitimately due to receptor trafficking rather than artifact-related fluorescence signal loss, e.g. due to photobleaching.

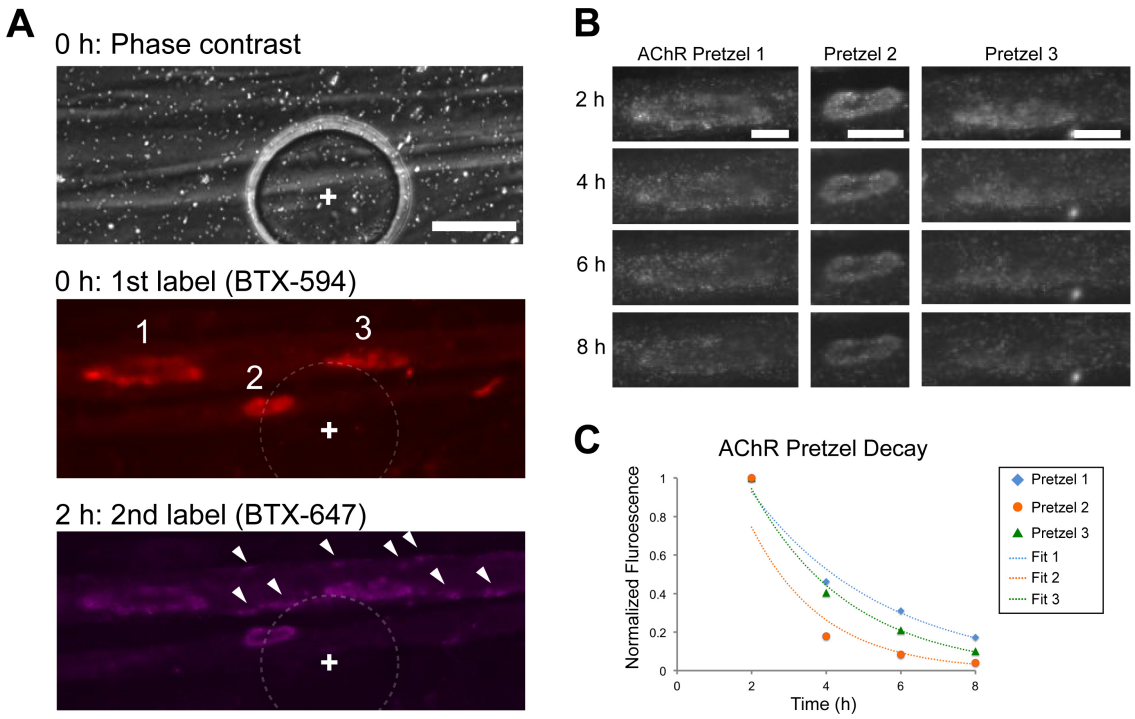

Figure 5.8: AChR pretzel timelapse microscopy and quantitative analysis.

(A) Myotubes overlying an aperture. 0 h, BTX-594-labeled (red) image shows three AChR pretzels present at the start. 2 h, after 1 h of agrin treatment, BTX-594-labeled (magenta) image shows the same three AChR pretzels, but also newly inserted AChR microclusters (white arrowheads). The dotted circle and cross represent the aperture edge and center, respectively. Scalebar = 50 μm. (B) Timelapse fluorescence micrographs of the three AChR pretzels shown in (A). Scalebar = 20 μm. (C) The mean intensities (normalized its own T1 intensity) of the AChR pretzels plotted versus time (hours).

We obtained the time constants, τ, for the decays of BTX-594 and BTX-647-labels for AChRs for n = 61 pretzels from 28 fields of view from a single experiment. For the whole dataset, the average time constants, τ, were 4.40 + 1.32 h and 6.25 + 1.88 h for BTX-594 and BTX-647 decays, respectively. This translated to half-lives of 1.32 + 0.51 h and 1.88 + 0.44 h for BTX-594 and BTX-647 decays. Figure 5.9 shows the scatterplots of R versus τ for decays of both colors. Because we expected a monotonic but not necessarily linear relationship, we calculated the Spearman rank correlation coefficients,

ϱ, between R and τ-BTX-594 and τ-BTX-647 time constants. The τ-BTX-594 showed a negligible positive correlation ($\varrho = 0.13$) with distance from aperture, while τ-BTX-647 showed a moderate positive correlation ($\varrho = 0.47$).

In further analysis, the time constant data was separated into arbitrary bins by pretzel position: a proximal group ($R < 250$ μm) in the closest quartile and a distal group ($R > 750$ μm) in the farthest quartile. For BTX-647, we showed that the distal time constants (6.85 ± 1.31 h, $n = 16$) were statistically significantly greater than proximal (5.50 ± 0.91 h, $n = 15$) (Student's t-test, $p < 0.01$). This trend was not seen with BTX-594 time constants, as proximal (3.84 ± 1.21 h) were not significantly different ($p > 0.05$) than distal (4.35 ± 1.38 h) time constants, similar to the Spearman rank correlation result. Finally, we identified FOVs containing two or more AChR pretzels, assigned one of the pretzels as proximal ($R < 500$ μm) and the other as distal ($R > 500$ μm), and performed a paired t-test of their time constants. Here, the rationale was that analysis of AChR pretzels within the same FOV, receiving agrin stimulus from the same source would be robust against variability between apertures. With a small sample size, ($n = 6$), again we saw a statistically significant difference between proximal and distal τ-BTX-647 ($p < 0.01$) but not for τ-BTX-594 ($p > 0.05$). Together, these results, surprisingly, suggested that AChR pretzels nearer to the apertures receiving higher agrin local doses, became relatively *less* stable in response to agrin compared to their counterparts farther from the apertures that received less agrin.

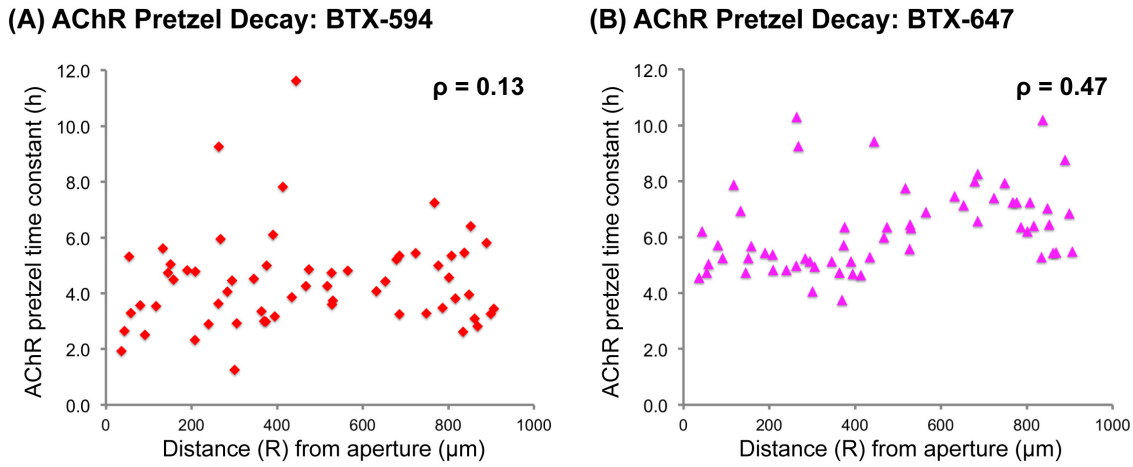

Figure 5.9: Scatterplots of AChR pretzel stability (time constants) versus distance from aperture.

(A) Time constants of decay of BTX-594-labeled receptors and (B) of BTX-647-labeled receptors.

5.5 Discussion

In our microfluidic platform, we studied acetylcholine receptor dynamics in response to focal application of agrin. AChR aggregations were classified as either "microclusters" or "pretzels," based on their size and morphology. Consistent with *in vivo* [160] and *in vitro* studies [10], we found AChR clusters to be highly dynamic structures, with a high turnover rate from receptor degradation, insertion, and possibly re-insertion. Using two colors of fluorescently-conjugated bungarotoxin, we were able to distinguish between "old" pre-existing and "new" inserted AChR clusters in response to agrin. When agrin was focally applied onto micropatterned myotubes, the exposed portions of the myotubes showed significant localized increase in new AChR "microclustering" around apertures. Although there was a global increase in total AChR microcluster number, larger net increase occurred centered around the apertures.

We attribute the slight global increase in AChR microclustering to diffusive broadening of the focal agrin signal. Since molecular transport in the system is purely

based on passive diffusion through a porous membrane, there was likely an evolving gradient of agrin emanating from the aperture point sources (see **Chapter 4**, Figure 4.4). Therefore, even the distant regions from apertures likely encountered a low dose of agrin. The extent of broadening and the slope of the concentration gradient depended on the agrin dose and duration of application. To achieve AChR focal microclustering, a relatively high agrin dose (555 nM) and short duration of stimulation (1 h) was required, compared to bath application [10, 157] and previous focal stimulation devices [45, 46]. Moreover, we found that 1000 nM basal side agrin application for 1 h induced homogeneous AChR microclusters throughout myotube surfaces, while 100 nM for 18 h showed no increase in AChR microclusters (data not shown). Agrin transport was likely to be limited by the small available open membrane regions for diffusive flux defined by the apertures. Therefore, due to transport limitations, there was a high critical agrin concentration necessary for an observable AChR clustering response. Ngo et al. reported that 10 nM agrin in bath application induced a maximal amount of AChR microclustering [157]. Empirically, we found that this Transwell platform required a 55 x greater concentration to induce local AChR microclustering. In addition to dose and duration of stimulation, agrin transport was likely affected by factors such as: 1) nonspecific agrin adsorption to the membrane, 2) the prevention of agrin leakage into the apical side bath by cell coverage over apertures, and 3) available receptors, Lrp4, for agrin binding. Factor 1 was addressed in control experiments described in Section 5.4.2. Factors 2 and 3 were difficult to control and were accepted as sources of error. Notably, apertures with insufficient cell coverage were discarded in the analysis.

We further used our microfluidic platform to investigate AChR pretzel stability in response to focal application of agrin. Consistent with previous reports [10, 23], we found

numerous large laminin-induced AChR "pretzels" on the Matrigel microtracks in the absence of agrin. We tested the hypothesis that agrin is a locally-acting stabilizer of these pre-existing AChR pretzels. We characterized the stability of pre-existing AChR pretzels by measuring their fluorescence intensity over 8 hours after focal agrin treatment. From the fluorescence decay, we inferred the rate of receptor removal from the pretzels. Contrary to our original hypothesis, proximity to the aperture, i.e. higher local agrin doses, showed a weak to moderate correlation with *lower* AChR pretzel half-life. The BTX-594 decay time constants showed a weak correlation with pretzel distance from aperture. BTX-594 was used to label receptors prior to agrin treatment, and so was an indicator of the original laminin-induced AChRs. Surprisingly, the BTX-647 decay times constant showed a moderate correlation with pretzel distance from aperture. BTX-647 was used to label receptors after agrin treatment, which consisted of new receptors that were inserted into the plasma membrane by either agrin induction, insertion due to natural turnover, or lateral diffusion. The proximal regions, closer to source of agrin, which showed lower pretzel half-lives, also showed more new AChR microclusters. These results suggest that agrin may accelerate AChR degradation in pretzels, while forming new AChR microclusters, possibly from the redistribution of the degraded AChRs from the pretzels.

Our original hypothesis that agrin was a locally-acting stabilizer of AChR pretzels was mainly derived from a finding by Tourovskaia et al. where focal agrin application reduced AChR loss in agrin-exposed pretzels [29]. In contrast, Bruneau et al. [10] showed that receptor removal at pre-existing laminin-induced AChR pretzels was unaffected by bath application of agrin. Moreover, Bruneau et al. found that agrin

treatment *decreased* the accumulation of new receptors into pre-existing AChR pretzels, and increased insertion of receptors into new microclusters [10].

One possible explanation for the discrepancy between our pretzel stability results and Tourovskaia's results may be molecular transport differences in the microfluidic platforms. Tourovskaia's system was a laminar flow-based device that generated sharp stepwise focal streams, allowing the AChR pretzel data to be "binarized" as either agrin-exposed or agrin-deprived. In contrast, our Transwell platform, which was based on passive diffusion from point sources (apertures), likely generated more gradual evolving gradients of agrin around apertures. Instead of assigning pretzels as strictly agrin-exposed or agrin-deprived, pretzels were exposed to a continuum of agrin concentrations, as reflected in the gradient of AChR microclustering increase centered on the apertures (Figure 5.6 A, B). When we binned our pretzel decay time constant data into groups at the proximal and distal extremes, we saw that pretzels receiving more agrin at the proximal end had significantly *lower* half-lives, opposite to Touvoskaia's finding. Therefore, it is possible that to alter AChR pretzel stability, we need to impose a sharper localized gradient of agrin. To affect stability, it is possible that a neighboring pretzel needs to be *deprived* of agrin as much as a given pretzel needs to *receive* agrin.

Bruneau et al. explicitly found that the pro-clustering C-terminal agrin fragment used in our studies has no effect on AChR metabolic stability in a C2C12 culture system. While the C-terminal region of agrin is known to be responsible for receptor aggregation, it is possible for other regions of agrin to be responsible for AChR metabolic stability. Our results in bath (apical side) and focal agrin application largely corroborated with Bruneau et al.'s results: 1) agrin induced the insertion of new receptors in numerous AChR microclusters homogeneously throughout the myotube (locally in the case of focal

application), 2) agrin had little to no effect on the rate of removal of AChR receptors from pre-existing pretzels, 3) agrin decreased the rate of AChR receptor insertion into pre-existing pretzels.

During the preparation of this paper, a study by Brenner et al. was published that showed that exogenous agrin played a major role in the metabolic stability of AChRs *in vivo*, by inducing the recycling of AChRs at ectopic postsynaptic clusters [153]. However, this finding could not be recapitulated in cultured C2C12 myotubes even with full-length agrin expressed by co-cultured COS-1 cells. Together, the findings from Bruneau and Brenner suggest that AChR metabolic stability in C2C12 cell culture models may require yet unknown exogenous factors other than agrin. Another possibility is that C2C12 cell culture models may not be predictive of *in vivo* AChR metabolic stability.

5.6 CONCLUSIONS

We developed a novel, user-friendly platform for large-scale studies of AChR clustering events in the context of NMJ synaptogenesis. Our Transwell microfluidic platform attempts to mimic early stage neuromuscular synaptogenesis by substituting the motor neuron with apertures that focally deliver the synaptogenic protein, agrin, to subcellular regions of cultured myotubes. The system has all of the advantages of being cell-benign and user-friendly as described in **Chapter 4**. First, we demonstrated high myotube viability and feasibility for long-term live cell imaging of bungarotoxin-labeled AChR clusters. The micropatterned myotubes can be organized in large organized arrays, providing a platform for automated large-scale microscopy acquisitions, straightforward high throughput quantitative analysis. We showed that the system is capable of inducing localized myotube responses, as we observed that 1 hour-long focal agrin application led

to localized formation of AChR microclusters in C2C12 myotubes. We further investigated the metabolic stability of laminin-induced AChR "pretzel" clusters in response to focal application of agrin. Surprisingly, we found that focal agrin has little to no effect on the rate of AChR loss, but may decelerate the rate of receptor insertion in myotubes. These results corroborate with bath agrin studies but refute focal agrin studies. Further investigation with different agrin doses and application durations may elucidate these disparities.

5.7 FINAL CONCLUSIONS AND FUTURE DIRECTIONS

We have presented a suite of microfluidic tools for focal delivery of soluble chemicals to micropatterned muscle cells. We were mainly motivated by the goal to build an *in vitro* model of the neuromuscular junction, in which a microfluidic device would replace the motor neuron, focally delivering neuronal factors to subcellular regions of cultured myotubes. In our efforts, we built two distinct microfluidic systems: 1) a flow-focusing system that utilizes hydrodynamic focusing in an open architecture, and 2) a modification of the standard Transwell that utilizes area-limited diffusion through a microporous membrane. We review the key features, advantages and disadvantages of the two systems in Table 5.1.

In our opinion, the flow-focusing device is better suited for applications where steep, almost stepwise, gradients (i.e. < 100 μm wide) of focal stimulation are desired. Such high-resolution steep gradients could be used to address single cells or parts of single cells. We have already demonstrated the utility of the device in generating gradients within single myofibers. For example, one can envision experiments testing the chemotactic effects of steep growth factor gradients on satellite cell migration on the surface of intact myofibers. One drawback of the device is that it is relatively low-throughput, with 32 or 64 focal stimulation units in the current form. Future designs will need to more efficiently use space within the device in maximizing the number of units. Furthermore, although the system is user-friendly, requiring only two syringe pumps, a vacuum source, and some tubing, device setup, especially coupling with a microscope stage, is still somewhat labor intensive.

In contrast to the flow-focusing platform, our opinion is that the modified Transwell platform is better suited for localized chemistry applications where spatial

resolution and sharpness of focal application are not as important, and diffusion from a point source is acceptable. Transport is likely species-specific, dependent upon molecular weight and binding kinetics, and must be determined empirically. The system is suitable for focally delivering differentiation factors to large cell culture surface areas, e.g. cell sheets for tissue engineering applications, and stem cell colonies for developmental biology studies. We have already demonstrated localized transfection of cell sheets with liposome-based approaches. The Transwell format is readily accessible for non-specialized scientists and provides a high-throughput platform.

In future experiments, we propose to study the effects of flow-focused delivery of agrin on AChR pretzel stability. It would be interesting to see if focal agrin has a local stabilizing or destabilizing effect. Notably, it will answer the question: does a sharper focal stimulation profile, i.e. steeper gradient, affect AChR pretzel stability differently? In another future direction, we propose to focally apply other neuronal factors in addition to agrin (e.g. acetylcholine, a negative factor) involved in NMJ synaptogenesis. Here, we propose to characterize the individual and combined effects of focal and bath application of agrin and acetylcholine on AChR clustering. One hypothesis is that acetycholine is a global (non-focal) AChR cluster dispersing factor but that its effect is overridden by the stabilizing action of local agrin; the localization of the agrin signal is the ultimate determinant of where the AChR pretzel will remain [25]. However, this hypothesis is predicated upon agrin being an AChR cluster-stabilizing factor.

In summary, we have built, characterized, and applied two microfluidic platforms for the focal stimulation of muscle cells. These systems were coupled with micropatterned techniques specific for the devices. We demonstrated that the Transwell

apertures system could be used in large-scale studies of AChR clustering dynamics in the context of neuromuscular junction synaptogenesis.

Table 5.1: Comparison of microfluidic platforms in this dissertation

	Flow-focusing focal stimulation devices (Chapter 2)	**Membrane-based focal stimulation devices (Chapters 3, 4, and 5)**
Focusing mechanism	Hydrodynamic focusing (laminar flow)	Area-selective diffusion through microporous membranes to cell basal side (passive diffusion)
Focusing spatial resolution	Streamwidth (FWHM): 36 – 187 μm	Cell staining (WGA) width (FWHM): 34 μm; minimum resolution: 20 μm
Focusing sustainability	20% increase in streamwidth in 10 h Sharper profile	104% increase in cell staining (WGA) in 48 h Evolving gradient: sharp to more gradual profile
Simulation of local concentrations	Yes	Unknown
Dynamic control of focusing	Yes	No
Cell micropatterning	Site-specific epoxy-silane trench surface modification (topographical and chemical micropattern)	Fluorosilane-based micropatterning (chemical micropattern)
Cell imaging	Optically clear PDMS and glass bottom Trench topographies: difficult to visualize cell boundaries	Optically clear porous membranes $\geq$ 1 μm pores: speckle noise Membrane unevenness
Open chamber	Yes	Yes
Shear stress onto cells	Low	None
Throughput	32, 64 jet units	144, 216, 504 aperture units
User-friendliness	Two syringe pumps, vacuum, three tubing lines	Standard 6-well plate (Transwell)
NMJ focal experiments	Difficulty in imaging AChR clusters due to trench topography	Focal agrin induced local AChR microclusters Focal agrin had no effect on AChR pretzel stability
Other applications	Primary myofiber trapping and focal stimulation	Regio-selective transfection of CHO cell sheets

REFERENCES

[1] C. L. Waites, A. M. Craig, and C. C. Garner, "Mechanisms of vertebrate synaptogenesis," *Annu. Rev. Neurosci.,* vol. 28, pp. 251-274, 2005.

[2] S. Herculano-Houzel, "The human brain in numbers: a linearly scaled-up primate brain," *Frontiers in Human Neuroscience,* vol. 3, 2009.

[3] J. E. Melom and J. T. Littleton, "Synapse development in health and disease," *Current Opinion in Genetics and Development,* vol. 21, pp. 256-261, Jul 01 2011.

[4] S. J. Burden, "SnapShot: Neuromuscular Junction," *Cell,* vol. 144, pp. 826-826.e1, Apr 04 2011.

[5] H. Wu, W. C. Xiong, and L. Mei, "To build a synapse: signaling pathways in neuromuscular junction assembly," *Development,* vol. 137, pp. 1017-1033, Apr 09 2010.

[6] S. J. Burden, "The formation of neuromuscular synapses," *Genes and Development,* vol. 12, pp. 133-148, Feb 15 1998.

[7] J. R. Sanes and J. W. Lichtman, "Induction, assembly, maturation and maintenance of a postsynaptic apparatus.," *Nature reviews. Neuroscience,* vol. 2, pp. 791-805, Nov 2001.

[8] J. R. Sanes and J. W. Lichtman, "Development of the vertebrate neuromuscular junction," *Annu. Rev. Neurosci.,* vol. 22, pp. 389-442, Apr 01 1999.

[9] M. A. Bowe and J. R. Fallon, "The role of agrin in synapse formation," *Annu. Rev. Neurosci.,* vol. 18, pp. 443-462, 1995.

[10] E. G. Bruneau, P. C. Macpherson, D. Goldman, R. I. Hume, and M. Akaaboune, "The effect of agrin and laminin on acetylcholine receptor dynamics in vitro," *Developmental Biology,* vol. 288, pp. 248-258, Dec 2005.

[11] F. Ono, "An Emerging Picture of Synapse Formation: A Balance of Two Opposing Pathways," *Science Signaling,* vol. 1, pp. pe3-pe3, Feb 08 2008.

[12] J. R. Sanes, "The Basement Membrane/Basal Lamina of Skeletal Muscle," *Journal of Biological Chemistry,* vol. 278, pp. 12601-12604, Feb 29 2003.

[13] B. G. Wallace, "The Mechanism of Agrin-Induced Acetylcholine Receptor Aggregation," *Philosophical Transactions of the Royal Society B: Biological Sciences,* vol. 331, pp. 273-280, Apr 29 1991.

[14] I. Cohen, M. Rimer, T. Lømo, and U. J. McMahan, "Agrin-induced postsynaptic-like apparatus in skeletal muscle fibers in vivo.," *Molecular and cellular neurosciences,* vol. 9, pp. 237-253, 1997.

[15] T. Meier, D. M. Hauser, M. Chiquet, L. Landmann, M. A. Ruegg, and H. R. Brenner, "Neural agrin induces ectopic postsynaptic specializations in innervated muscle fibers.," *The Journal of neuroscience,* vol. 17, pp. 6534-6544, Sep 01 1997.

[16] W. Lin, R. W. Burgess, B. Dominguez, S. L. Pfaff, J. R. Sanes, and K. F. Lee, "Distinct roles of nerve and muscle in postsynaptic differentiation of the neuromuscular synapse.," *Nature,* vol. 410, pp. 1057-1064, May 26 2001.

[17] T. M. DeChiara, D. C. Bowen, D. M. Valenzuela, M. V. Simmons, W. T. Poueymirou, S. Thomas, *et al.*, "The receptor tyrosine kinase MuSK is required for neuromuscular junction formation in vivo.," *CELL,* vol. 85, pp. 501-512, Jun 17 1996.

[18] M. Gautam, P. G. Noakes, J. Mudd, M. Nichol, G. C. Chu, J. R. Sanes, *et al.*, "Failure of postsynaptic specialization to develop at neuromuscular junctions of rapsyn-deficient mice.," *Nature,* vol. 377, pp. 232-236, Sep 21 1995.

[19] Z. Dai, X. Luo, H. Xie, and H. B. Peng, "The actin-driven movement and formation of acetylcholine receptor clusters.," *The Journal of Cell Biology,* vol. 150, pp. 1321-1334, Sep 18 2000.

[20] T. T. Kummer, T. Misgeld, and J. R. Sanes, "Assembly of the postsynaptic membrane at the neuromuscular junction: paradigm lost," *Current Opinion in Neurobiology,* vol. 16, pp. 74-82, Mar 2006.

[21] X. Yang, S. Arber, C. William, L. Li, Y. Tanabe, T. M. Jessell, *et al.*, "Patterning of muscle acetylcholine receptor gene expression in the absence of motor innervation.," *Neuron,* vol. 30, pp. 399-410, Jun 2001.

[22] V. Witzemann, "Development of the neuromuscular junction," *Cell and Tissue Research,* vol. 326, pp. 263-271, Jul 04 2006.

[23] T. T. Kummer, "Nerve-independent formation of a topologically complex postsynaptic apparatus," *The Journal of Cell Biology,* vol. 164, pp. 1077-1087, Apr 29 2004.

[24] W. Lin, B. Dominguez, J. Yang, P. Aryal, E. P. Brandon, F. H. Gage, *et al.*, "Neurotransmitter Acetylcholine Negatively Regulates Neuromuscular Synapse Formation by a Cdk5-Dependent Mechanism," *Neuron,* vol. 46, pp. 569-579, Jun 2005.

[25] T. Misgeld, T. T. Kummer, J. W. Lichtman, and J. R. Sanes, "Agrin promotes synaptic differentiation by counteracting an inhibitory effect of neurotransmitter.," *Proceedings of the National Academy of Sciences of the United States of America,* vol. 102, pp. 11088-11093, Aug 02 2005.

[26] M. A. Samuel, G. Valdez, J. C. Tapia, J. W. Lichtman, and J. R. Sanes, "Agrin and Synaptic Laminin Are Required to Maintain Adult Neuromuscular Junctions," *PLoS ONE,* vol. 7, p. e46663, Oct 03 2012.

[27] H. Flanagan-Steet, "Neuromuscular synapses can form in vivo by incorporation of initially aneural postsynaptic specializations," *Development,* vol. 132, pp. 4471-4481, Oct 15 2005.

[28] G. Bezakova, I. Rabben, I. Sefland, G. Fumagalli, and T. Lømo, "Neural agrin controls acetylcholine receptor stability in skeletal muscle fibers.," *Proceedings of the National Academy of Sciences of the United States of America,* vol. 98, pp. 9924-9929, Aug 14 2001.

[29] A. Tourovskaia, N. Li, and A. Folch, "Localized Acetylcholine Receptor Clustering Dynamics in Response to Microfluidic Focal Stimulation with Agrin," *Biophysical Journal,* vol. 95, pp. 3009-3016, Sep 2008.

[30] J. W. Lichtman and J. R. Sanes, "Watching the neuromuscular junction.," *Journal of neurocytology,* vol. 32, pp. 767-775, Jul 2003.

[31] M. K. Walsh and J. W. Lichtman, "In vivo time-lapse imaging of synaptic takeover associated with naturally occurring synapse elimination.," *Neuron,* vol. 37, pp. 67-73, Feb 09 2003.

[32] M. Das, J. W. Rumsey, N. Bhargava, M. Stancescu, and J. J. Hickman, "A defined long-term in vitro tissue engineered model of neuromuscular junctions," *Biomaterials,* vol. 31, pp. 4880-4888, Jul 2010.

[33] M. Das, J. W. Rumsey, C. A. Gregory, N. Bhargava, J. F. Kang, P. Molnar*, et al.*, "Embryonic motoneuron-skeletal muscle co-culture in a defined system," *Neuroscience,* vol. 146, pp. 481-488, Jun 2007.

[34] X. Guo, M. Das, J. Rumsey, M. Gonzalez, M. Stancescu, and J. Hickman, "Neuromuscular Junction Formation Between Human Stem-Cell-Derived Motoneurons and Rat Skeletal Muscle in a Defined System," *Tissue Engineering Part C: Methods,* vol. 16, pp. 1347-1355, Dec 2010.

[35] X. Guo, M. Gonzalez, M. Stancescu, H. H. Vandenburgh, and J. J. Hickman, "Neuromuscular junction formation between human stem cell-derived motoneurons and human skeletal muscle in a defined system," *Biomaterials,* vol. 32, pp. 9602-9611, Dec 01 2011.

[36] M. Das, K. Wilson, P. Molnar, and J. J. Hickman, "Differentiation of skeletal muscle and integration of myotubes with silicon microstructures using serum-free medium and a synthetic silane substrate," *Nature Protocols,* vol. 2, pp. 1795-1801, Jul 2007.

[37] K. A. Southam, A. E. King, C. A. Blizzard, G. H. McCormack, and T. C. Dickson, "Microfluidic primary culture model of the lower motor neuron–

neuromuscular junction circuit," *Journal of Neuroscience Methods,* vol. 218, pp. 164-169, Sep 2013.

[38] L. P. Baker, Q. Chen, and H. B. Peng, "Induction of acetylcholine receptor clustering by native polystyrene beads. Implication of an endogenous muscle-derived signalling system," *Journal of Cell Science,* vol. 102, pp. 543-555, 1992.

[39] T. Cornish, "Microcontact Printing: A Versatile Technique for the Study of Synaptogenic Molecules," *Molecular and Cellular Neuroscience,* vol. 20, pp. 140-153, Jun 2002.

[40] A. M. Taylor and N. L. Jeon, "Micro-scale and microfluidic devices for neurobiology," *Current Opinion in Neurobiology,* vol. 20, pp. 640-647, Oct 01 2010.

[41] C. A. Croushore and J. V. Sweedler, "Microfluidic systems for studying neurotransmitters and neurotransmission," *Lab on a Chip,* vol. 13, p. 1666, 2013.

[42] R. J. Balice-Gordon and J. W. Lichtman, "Long-term synapse loss induced by focal blockade of postsynaptic receptors.," *Nature,* vol. 372, pp. 519-524, Dec 08 1994.

[43] G. Jones, T. Meier, M. Lichtsteiner, V. Witzemann, B. Sakmann, and H. R. Brenner, "Induction by agrin of ectopic and functional postsynaptic-like membrane in innervated muscle.," *Proceedings of the National Academy of Sciences of the United States of America,* vol. 94, pp. 2654-2659, Apr 18 1997.

[44] L. P. Baker and H. B. Peng, "Induction of acetylcholine receptor cluster formation by local application of growth factors in cultured Xenopus muscle cells.," *Neuroscience letters,* vol. 185, pp. 135-138, Mar 09 1995.

[45] T. F. Kosar, A. Tourovskaia, X. Figueroa-Masot, M. E. Adams, and A. Folch, "A nanofabricated planar aperture as a mimic of the nerve muscle contact during synaptogenesis," *Lab on a Chip,* vol. 6, p. 632, 2006.

[46] A. Tourovskaia, T. F. Kosar, and A. Folch, "Local Induction of Acetylcholine Receptor Clustering in Myotube Cultures Using Microfluidic Application of Agrin," *Biophysical Journal,* vol. 90, pp. 2192-2198, Apr 15 2006.

[47] M. L. Yarmush and K. R. King, "Living-Cell Microarrays," *Annual Review of Biomedical Engineering,* vol. 11, pp. 235-257, Aug 2009.

[48] E. W. K. Young and D. J. Beebe, "Fundamentals of microfluidic cell culture in controlled microenvironments," *Chemical Society Reviews,* vol. 39, p. 1036, 2010.

[49] A. Folch and M. Toner, "Microengineering of cellular interactions.," *Annual Review of Biomedical Engineering,* vol. 2, pp. 227-256, 2000.

[50] C. S. Chen, "Geometric Control of Cell Life and Death," *Science,* vol. 276, pp. 1425-1428, Jun 30 1997.

[51] A. L. Paguirigan and D. J. Beebe, "Microfluidics meet cell biology: bridging the gap by validation and application of microscale techniques for cell biological assays," *BioEssays,* vol. 30, pp. 811-821, Sep 2008.

[52] K. E. Healy, "Patterning: Cells nourished by nanodrops," *Nature Materials,* vol. 8, pp. 700-702, Sep 01 2009.

[53] H. Tavana, B. Mosadegh, and S. Takayama, "Polymeric Aqueous Biphasic Systems for Non-Contact Cell Printing on Cells: Engineering Heterocellular Embryonic Stem Cell Niches," *Advanced Materials,* vol. 22, pp. 2628-2631, Jun 06 2010.

[54] G. V. Kaigala, R. D. Lovchik, and E. Delamarche, "Microfluidics in the "Open Space" for Performing Localized Chemistry on Biological Interfaces," *Angewandte Chemie International Edition,* vol. 51, pp. 11224-11240, Oct 30 2012.

[55] P. S. Dittrich and A. Manz, "Lab-on-a-chip: microfluidics in drug discovery," *Nature Reviews Drug Discovery,* vol. 5, pp. 210-218, Apr 2006.

[56] A. Scott, K. Weir, C. Easton, W. Huynh, W. J. Moody, and A. Folch, "A microfluidic microelectrode array for simultaneous electrophysiology, chemical stimulation, and imaging of brain slices," *Lab on a Chip,* vol. 13, p. 527, 2013.

[57] N. Klauke, G. Smith, and J. M. Cooper, "Local Regional Stimulation of Single Isolated Ventricular Myocytes Using Microfluidics," *Analytical Chemistry,* vol. 81, pp. 6390-6398, Aug 2009.

[58] D. J. Beebe, G. A. Mensing, and G. M. Walker, "Physics and Applications of Microfluidics in Biology," *Annual Review of Biomedical Engineering,* vol. 4, pp. 261-286, Aug 2002.

[59] T. M. Squires and S. R. Quake, "Microfluidics: Fluid physics at the nanoliter scale," *Reviews of modern physics,* vol. 77, p. 977, 2005.

[60] S. Takayama, E. Ostuni, P. LeDuc, K. Naruse, D. E. Ingber, and G. M. Whitesides, "Selective Chemical Treatment of Cellular Microdomains Using Multiple Laminar Streams," *Chemistry and Biology,* vol. 10, pp. 123-130, Mar 2003.

[61] S. Takayama, E. Ostuni, P. LeDuc, K. Naruse, D. E. Ingber, and G. M. Whitesides, "Subcellular positioning of small molecules.," *Nature,* vol. 411, p. 1016, Jul 28 2001.

[62] J. P. Golden, G. A. Justin, M. Nasir, and F. S. Ligler, "Hydrodynamic focusing—a versatile tool," *Analytical and Bioanalytical Chemistry,* vol. 402, pp. 325-335, Sep 29 2011.

[63] A. Tourovskaia, X. Figueroa-Masot, and A. Folch, "Differentiation-on-a-chip: A microfluidic platform for long-term cell culture studies," *Lab on a Chip,* vol. 5, p. 14, 2005.

[64] A. Tourovskaia, X. Figueroa-Masot, and A. Folch, "Long-term microfluidic cultures of myotube microarrays for high-throughput focal stimulation," *Nature Protocols,* vol. 1, pp. 1092-1104, Aug 2006.

[65] C. Kim, K. Kreppenhofer, J. Kashef, D. Gradl, D. Herrmann, M. Schneider, *et al.*, "Diffusion- and convection-based activation of Wnt/β-catenin signaling in a gradient generating microfluidic chip," *Lab on a Chip,* vol. 12, p. 5186, 2012.

[66] T. Kim, M. Pinelis, and M. M. Maharbiz, "Generating steep, shear-free gradients of small molecules for cell culture," *Biomedical Microdevices,* vol. 11, pp. 65-73, Aug 08 2008.

[67] J. J. VanDersarl, A. M. Xu, and N. A. Melosh, "Rapid spatial and temporal controlled signal delivery over large cell culture areas," *Lab on a Chip,* vol. 11, p. 3057, 2011.

[68] C. G. Sip, N. Bhattacharjee, and A. Folch, "Microfluidic transwell inserts for generation of tissue culture-friendly gradients in well plates," *Lab on a Chip,* 2013.

[69] D. Huh, B. D. Matthews, A. Mammoto, M. Montoya-Zavala, H. Y. Hsin, and D. E. Ingber, "Reconstituting Organ-Level Lung Functions on a Chip," *Science,* vol. 328, pp. 1662-1668, Jul 24 2010.

[70] J. W. Song, S. P. Cavnar, A. C. Walker, K. E. Luker, M. Gupta, Y.-C. Tung, *et al.*, "Microfluidic Endothelium for Studying the Intravascular Adhesion of Metastatic Breast Cancer Cells," *PLoS ONE,* vol. 4, p. e5756, Jul 01 2009.

[71] J. Kawada, H. Kimura, H. Akutsu, Y. Sakai, and T. Fujii, "Spatiotemporally controlled delivery of soluble factors for stem cell differentiation," *Lab on a Chip,* vol. 12, p. 4508, 2012.

[72] K.-J. Jang and K.-Y. Suh, "A multi-layer microfluidic device for efficient culture and analysis of renal tubular cells," *Lab on a Chip,* vol. 10, p. 36, 2010.

[73] Y.-s. Torisawa, B.-h. Chueh, D. Huh, P. Ramamurthy, T. M. Roth, K. F. Barald, *et al.*, "Efficient formation of uniform-sized embryoid bodies using a compartmentalized microchannel device," *Lab on a Chip,* vol. 7, p. 770, 2007.

[74] N. Bhattacharjee, N. Li, T. M. Keenan, and A. Folch, "A neuron-benign microfluidic gradient generator for studying the response of mammalian neurons towards axon guidance factors," *Integrative Biology,* vol. 2, p. 669, 2010.

[75] G. M. Walker, H. C. Zeringue, and D. J. Beebe, "Microenvironment design considerations for cellular scale studies," *Lab on a Chip,* vol. 4, p. 91, 2004.

[76] X. Su, A. B. Theberge, C. T. January, and D. J. Beebe, "Effect of Microculture on Cell Metabolism and Biochemistry: Do Cells Get Stressed in Microchannels?," *Analytical Chemistry,* vol. 85, pp. 1562-1570, Mar 05 2013.

[77] A. L. Paguirigan and D. J. Beebe, "From the cellular perspective: exploring differences in the cellular baseline in macroscale and microfluidic cultures," *Integrative Biology,* vol. 1, p. 182, 2009.

[78] I. Meyvantsson and D. J. Beebe, "Cell Culture Models in Microfluidic Systems," *Annual Review of Analytical Chemistry,* vol. 1, pp. 423-449, Jul 2008.

[79] H. Yin, X. Zhang, N. Pattrick, N. Klauke, H. C. Cordingley, S. J. Haswell, *et al*., "Influence of Hydrodynamic Conditions on Quantitative Cellular Assays in Microfluidic Systems," *Analytical Chemistry,* vol. 79, pp. 7139-7144, Sep 2007.

[80] J. S. Garanich, "Shear stress inhibits smooth muscle cell migration via nitric oxide-mediated downregulation of matrix metalloproteinase-2 activity," *AJP: Heart and Circulatory Physiology,* vol. 288, pp. H2244-H2252, Feb 14 2005.

[81] C. Joanne Wang, X. Li, B. Lin, S. Shim, G.-l. Ming, and A. Levchenko, "A microfluidics-based turning assay reveals complex growth cone responses to integrated gradients of substrate-bound ECM molecules and diffusible guidance cues," *Lab on a Chip,* vol. 8, p. 227, 2008.

[82] R. D. Lovchik, F. Bianco, N. Tonna, A. Ruiz, M. Matteoli, and E. Delamarche, "Overflow Microfluidic Networks for Open and Closed Cell Cultures on Chip," *Analytical Chemistry,* vol. 82, pp. 3936-3942, Jun 2010.

[83] D. Jowhar, G. Wright, P. C. Samson, J. P. Wikswo, and C. Janetopoulos, "Open access microfluidic device for the study of cell migration during chemotaxis," *Integrative Biology,* vol. 2, p. 648, 2010.

[84] T. M. Keenan, C.-H. Hsu, and A. Folch, "Microfluidic “jets” for generating steady-state gradients of soluble molecules on open surfaces," *Applied Physics Letters,* vol. 89, p. 114103, 2006.

[85] D. Juncker, H. Schmid, and E. Delamarche, "Multipurpose microfluidic probe," *Nature Materials,* vol. 4, pp. 622-628, Jul 24 2005.

[86] M. A. Qasaimeh, S. G. Ricoult, and D. Juncker, "Microfluidic probes for use in life sciences and medicine," *Lab on a Chip,* vol. 13, p. 40, 2012.

[87] G. V. Kaigala, R. D. Lovchik, U. Drechsler, and E. Delamarche, "A Vertical Microfluidic Probe," *Langmuir,* vol. 27, pp. 5686-5693, Jun 03 2011.

[88] D. M. Cate, C. G. Sip, and A. Folch, "A microfluidic platform for generation of sharp gradients in open-access culture," *Biomicrofluidics,* vol. 4, p. 044105, 2010.

[89] K. Takoh, A. Takahashi, T. Matsue, and M. Nishizawa, "A porous membrane-based microelectroanalytical technique for evaluating locally stimulated culture cells," *Analytica Chimica Acta,* vol. 522, pp. 45-49, Sep 2004.

[90] K. Takoh, T. Ishibashi, T. Matsue, and M. Nishizawa, "Localized chemical stimulation of cellular micropatterns using a porous membrane-based culture substrate," *Sensors and Actuators: B. Chemical,* vol. 108, pp. 683-687, Jul 2005.

[91] Y.-s. Torisawa, B. Mosadegh, S. P. Cavnar, M. Ho, and S. Takayama, "Transwells with Microstamped Membranes Produce Micropatterned Two-Dimensional and Three-Dimensional Co-Cultures," *Tissue Engineering Part C: Methods,* vol. 17, pp. 61-67, Feb 2011.

[92] F. Evenou, J.-M. Di Meglio, B. Ladoux, and P. Hersen, "Micro-patterned porous substrates for cell-based assays," *Lab on a Chip,* vol. 12, p. 1717, 2012.

[93] S. Cosson, S. Allazetta, and M. P. Lutolf, "Patterning of cell-instructive hydrogels by hydrodynamic flow focusing," *Lab on a Chip,* vol. 13, p. 2099, 2013.

[94] B. Regenberg, U. Kr hne, M. Beyer, L. H. Pedersen, M. Sim n, O. R. T. Thomas, *et al*., "Use of laminar flow patterning for miniaturised biochemical assays," *Lab on a Chip,* vol. 4, p. 654, 2004.

[95] M. Chabert and J.-L. Viovy, "Microfluidic high-throughput encapsulation and hydrodynamic self-sorting of single cells.," *Proceedings of the National Academy of Sciences,* vol. 105, pp. 3191-3196, Apr 04 2008.

[96] J. B. Knight, A. Vishwanath, J. P. Brody, and R. H. Austin, "Hydrodynamic focusing on a silicon chip: mixing nanoliters in microseconds," *Physical Review Letters,* vol. 80, p. 3863, 1998.

[97] F. Wang, H. Wang, J. Wang, H.-Y. Wang, P. L. Rummel, S. V. Garimella, *et al*., "Microfluidic delivery of small molecules into mammalian cells based on hydrodynamic focusing," *Biotechnology and Bioengineering,* vol. 100, pp. 150-158, 2008.

[98] Y. Liu, W. B. Butler, and D. Pappas, "Spatially selective reagent delivery into cancer cells using a two-layer microfluidic culture system," *Analytica Chimica Acta,* vol. 743, pp. 125-130, Sep 19 2012.

[99] S. Chen and L. P. Lee, "Non-invasive microfluidic gap junction assay," *Integrative Biology,* vol. 2, p. 130, 2010.

[100] A. Manbachi, S. Shrivastava, M. Cioffi, B. G. Chung, M. Moretti, U. Demirci, *et al*., "Microcirculation within grooved substrates regulates cell positioning and cell docking inside microfluidic channels," *Lab on a Chip,* vol. 8, p. 747, 2008.

[101] C.-H. Hsu, C. Chen, and A. Folch, "Microcanals for micropipette access to single cells in microfluidic environments," *Lab on a Chip,* vol. 4, p. 420, 2004.

[102] J. L. Tan, W. Liu, C. M. Nelson, S. Raghavan, and C. S. Chen, "Simple approach to micropattern cells on common culture substrates by tuning substrate wettability.," *Tissue Engineering,* vol. 10, pp. 865-872, Jun 2004.

[103] M. R. Nejadnik, A. L. J. Olsson, P. K. Sharma, H. C. van der Mei, W. Norde, and H. J. Busscher, "Adsorption of Pluronic F-127 on Surfaces with Different Hydrophobicities Probed by Quartz Crystal Microbalance with Dissipation," *Langmuir,* vol. 25, pp. 6245-6249, Jul 02 2009.

[104] G. Shefer and Z. Yablonka-Reuveni, "Isolation and culture of skeletal muscle myofibers as a means to analyze satellite cells," *Methods Mol Biol.,* vol. 290, pp. 281-304, 2005.

[105] T. Stiles, R. Fallon, T. Vestad, J. Oakey, D. W. M. Marr, J. Squier, *et al.*, "Hydrodynamic focusing for vacuum-pumped microfluidics," *Microfluidics and Nanofluidics,* vol. 1, pp. 280-283, Apr 31 2005.

[106] G. M. Walker, J. Sai, A. Richmond, M. Stremler, C. Y. Chung, and J. P. Wikswo, "Effects of flow and diffusion on chemotaxis studies in a microfabricated gradient generator," *Lab on a Chip,* vol. 5, p. 611, 2005.

[107] J. Zhou, A. V. Ellis, and N. H. Voelcker, "Recent developments in PDMS surface modification for microfluidic devices," *Electrophoresis,* vol. 31, pp. 2-16, Feb 2010.

[108] Y. Nam, D. W. Branch, and B. C. Wheeler, "Epoxy-silane linking of biomolecules is simple and effective for patterning neuronal cultures," *Biosensors and Bioelectronics,* vol. 22, pp. 589-597, Dec 2006.

[109] M. J. Moorcroft, "In situ oligonucleotide synthesis on poly(dimethylsiloxane): a flexible substrate for microarray fabrication," *Nucleic Acids Research,* vol. 33, pp. e75-e75, May 28 2005.

[110] E. Tenstad, A. Tourovskaia, A. Folch, O. Myklebost, and E. Rian, "Extensive adipogenic and osteogenic differentiation of patterned human mesenchymal stem cells in a microfluidic device," *Lab on a Chip,* vol. 10, p. 1401, 2010.

[111] K. Webb, V. Hlady, and P. A. Tresco, "Relative importance of surface wettability and charged functional groups on NIH 3T3 fibroblast attachment, spreading, and cytoskeletal organization.," *Journal of Biomedical Materials Research Part A,* vol. 41, pp. 422-430, Sep 05 1998.

[112] P. M. Gilbert, S. Corbel, R. Doyonnas, K. Havenstrite, K. E. G. Magnusson, and H. M. Blau, "A single cell bioengineering approach to elucidate mechanisms of adult stem cell self-renewal," *Integrative Biology,* vol. 4, p. 360, 2012.

[113] J. Dhawan and T. A. Rando, "Stem cells in postnatal myogenesis: molecular mechanisms of satellite cell quiescence, activation and replenishment," *Trends in Cell Biology,* vol. 15, pp. 666-673, Dec 2005.

[114] T. J. Hawke and D. J. Garry, "Myogenic satellite cells: physiology to molecular biology.," *Journal of applied physiology (Bethesda, Md. : 1985),* vol. 91, pp. 534-551, Aug 2001.

[115] A. L. Siegel, K. Atchison, K. E. Fisher, G. E. Davis, and D. D. W. Cornelison, "3D Timelapse Analysis of Muscle Satellite Cell Motility," *Stem Cells,* vol. 27, pp. 2527-2538, Oct 2009.

[116] N. F. Huang, S. Patel, R. G. Thakar, J. Wu, B. S. Hsiao, B. Chu, *et al.*, "Myotube Assembly on Nanofibrous and Micropatterned Polymers," *Nano Letters,* vol. 6, pp. 537-542, Apr 2006.

[117] P. Bajaj, B. Reddy, L. Millet, C. Wei, P. Zorlutuna, G. Bao, *et al.*, "Patterning the differentiation of C2C12 skeletal myoblasts," *Integrative Biology,* vol. 3, p. 897, 2011.

[118] M. T. Lam, Y.-C. Huang, R. K. Birla, and S. Takayama, "Microfeature guided skeletal muscle tissue engineering for highly organized 3-dimensional free-standing constructs," *Biomaterials,* vol. 30, pp. 1150-1155, Mar 01 2009.

[119] D. Falconnet, G. Csucs, H. Michelle Grandin, and M. Textor, "Surface engineering approaches to micropattern surfaces for cell-based assays," *Biomaterials,* vol. 27, pp. 3044-3063, Jul 2006.

[120] A. Tourovskaia, T. Barber, B. T. Wickes, D. Hirdes, B. Grin, D. G. Castner, *et al.*, "Micropatterns of Chemisorbed Cell Adhesion-Repellent Films Using Oxygen Plasma Etching and Elastomeric Masks," *Langmuir,* vol. 19, pp. 4754-4764, Jun 2003.

[121] J. P. Bearinger, D. G. Castner, S. L. Golledge, A. Rezania, S. Hubchak, and K. E. Healy, "P(AAm- co-EG) Interpenetrating Polymer Networks Grafted to Oxide Surfaces: Surface Characterization, Protein Adsorption, and Cell Detachment Studies," *Langmuir,* vol. 13, pp. 5175-5183, Sep 1997.

[122] L. H. Ting, S. Feghhi, S. J. Han, M. L. Rodriguez, and N. J. Sniadecki, "Effect of Silanization Film Thickness in Soft Lithography of Nanoscale Features," *Journal of Nanotechnology in Engineering and Medicine,* vol. 2, p. 041006, 2011.

[123] S. S. Shah, M. C. Howland, L.-J. Chen, J. Silangcruz, S. V. Verkhoturov, E. A. Schweikert, *et al.*, "Micropatterning of Proteins and Mammalian Cells on Indium Tin Oxide," *ACS Applied Materials and Interfaces,* vol. 1, pp. 2592-2601, Nov 25 2009.

[124] L. Wang, B. Sun, K. S. Ziemer, G. A. Barabino, and R. L. Carrier, "Chemical and physical modifications to poly(dimethylsiloxane) surfaces affect adhesion of Caco-2 cells," *Journal of Biomedical Materials Research Part A,* vol. 93, pp. 1260-1271. Jun 15, 2009.

[125] D. Liazoghli, A. D. Roth, P. Thostrup, and D. R. Colman, "Substrate Micropatterning as a New in Vitro Cell Culture System to Study Myelination," *ACS Chemical Neuroscience,* vol. 3, pp. 90-95, Mar 15 2012.

[126] N. T. Kohen, L. E. Little, and K. E. Healy, "Characterization of Matrigel interfaces during defined human embryonic stem cell culture," *Biointerphases,* vol. 4, p. 69, 2009.

[127] V. A. Liu, W. E. Jastromb, and S. N. Bhatia, "Engineering protein and cell adhesivity using PEO-terminated triblock polymers," *Journal of Biomedical Materials Research Part A,* vol. 60, pp. 126-134, Feb 28 2002.

[128] J. O. Foley, E. Fu, L. J. Gamble, and P. Yager, "Microcontact printed antibodies on gold surfaces: Function, uniformity, and silicone contamination," *Langmuir,* vol. 24, pp. 3628-3635, Apr 1 2008.

[129] X. Dong, A. Proctor, and D. M. Hercules, "Characterization of poly(dimethylsiloxane)s by time-of-flight secondary ion mass spectrometry," *Macromolecules,* vol. 30, pp. 63-70, Jan 13 1997.

[130] N. T. Samuel, "Analysis of Poly(amino acids) by Static Time-of-Flight Secondary Ion Mass Spectrometry (TOF-SIMS)," *Surface Science Spectra,* vol. 8, p. 163, Jul 2001.

[131] J. B. Lhoest, M. S. Wagner, C. D. Tidwell, and D. G. Castner, "Characterization of adsorbed protein films by time of flight secondary ion mass spectrometry.," *Journal of Biomedical Materials Research Part A,* vol. 57, pp. 432-440, Dec 01 2001.

[132] D. S. Mantus, B. D. Ratner, B. A. Carlson, and J. F. Moulder, "Static Secondary-Ion Mass-Spectrometry of Adsorbed Proteins," *Analytical Chemistry,* vol. 65, pp. 1431-1438, May 15 1993.

[133] V. N. Luk, G. C. H. Mo, and A. R. Wheeler, "Pluronic additives: A solution to sticky problems in digital microfluidics," *Langmuir,* vol. 24, pp. 6382-6389, Jun 17 2008.

[134] O. E. Cassidy, G. Rowley, I. W. Fletcher, S. F. Davies, and D. Briggs, "Surface modification and electrostatic charge of polystyrene particles," *International Journal of Pharmaceutics,* vol. 182, pp. 199-211, May 25 1999.

[135] T. Ishizaki, N. Saito, and O. Takai, "Correlation of Cell Adhesive Behaviors on Superhydrophobic, Superhydrophilic, and Micropatterned Superhydrophobic/Superhydrophilic Surfaces to Their Surface Chemistry," *Langmuir,* vol. 26, pp. 8147-8154, Jul 2010.

[136] M. L. Godek, G. S. Malkov, and E. R. Fisher, "Macrophage Serum-Based Adhesion to Plasma-Processed Surface Chemistry is Distinct from That Exhibited by Fibroblasts," *Plasma Processes Polym.,* 2006.

[137] M. Rosso, V. van Steijn, L. C. P. M. de Smet, E. J. R. Sudhölter, C. R. Kleijn, and M. T. Kreutzer, "Reaction-diffusion analysis for one-step plasma etching and bonding of microfluidic devices," *Applied Physics Letters,* vol. 98, p. 174102, 2011.

[138] S. W. Rhee, A. M. Taylor, C. H. Tu, D. H. Cribbs, C. W. Cotman, and N. L. Jeon, "Patterned cell culture inside microfluidic devices," *Lab on a Chip,* vol. 5, p. 102, 2005.

[139] S. H. Tan, N.-T. Nguyen, Y. C. Chua, and T. G. Kang, "Oxygen plasma treatment for reducing hydrophobicity of a sealed polydimethylsiloxane microchannel," *Biomicrofluidics,* vol. 4, p. 032204, 2010.

[140] R. Booth and H. Kim, "Characterization of a microfluidic in vitro model of the blood-brain barrier (μBBB)," *Lab on a Chip,* vol. 12, p. 1784, 2012.

[141] B. Prabhakarpandian, M.-C. Shen, J. B. Nichols, I. R. Mills, M. Sidoryk-Wegrzynowicz, M. Aschner, *et al.*, "SyM-BBB: a microfluidic blood brain barrier model," *Lab on a Chip,* vol. 13, p. 1093, 2013.

[142] T. M. Keenan and A. Folch, "Biomolecular gradients in cell culture systems," *Lab on a Chip,* vol. 8, p. 34, 2007.

[143] I. A. Khalil, "Uptake Pathways and Subsequent Intracellular Trafficking in Nonviral Gene Delivery," *Pharmacological Reviews,* vol. 58, pp. 32-45, Apr 01 2006.

[144] B. S. Aytar, J. P. E. Muller, Y. Kondo, N. L. Abbott, and D. M. Lynn, "Spatial Control of Cell Transfection Using Soluble or Solid-Phase Redox Agents and a Redox-Active Ferrocenyl Lipid," *ACS Applied Materials and Interfaces,* vol. 5, pp. 8283-8288, Sep 11 2013.

[145] J. Ziauddin and D. M. Sabatini, "Microarrays of cells expressing defined cDNAs.," *Nature,* vol. 411, pp. 107-110, Jun 03 2001.

[146] R. Z. Wu, S. N. Bailey, and D. M. Sabatini, "Cell-biological applications of transfected-cell microarrays.," *Trends in Cell Biology,* vol. 12, pp. 485-488, Oct 2002.

[147] T. Houchin-Ray, K. J. Whittlesey, and L. D. Shea, "Spatially patterned gene delivery for localized neuron survival and neurite extension," *Molecular Therapy,* vol. 15, pp. 705-712, 2007.

[148] H. Tavana, A. Jovic, B. Mosadegh, Q. Y. Lee, X. Liu, K. E. Luker, *et al.*, "Nanolitre liquid patterning in aqueous environments for spatially defined reagent delivery to mammalian cells," *Nature Materials,* vol. 8, pp. 736-741, Aug 16 2009.

[149] J. H. Pai, Y. Wang, G. T. a. A. Salazar, C. E. Sims, M. Bachman, G. P. Li, *et al.*, "Photoresist with low fluorescence for bioanalytical applications.," *Analytical Chemistry,* vol. 79, pp. 8774-8780, Nov 15 2007.

[150] D. M. Ornoff, Y. Wang, and N. L. Allbritton, "Characterization of freestanding photoresist films for biological and MEMS applications," *Journal of Micromechanics and Microengineering,* vol. 23, p. 025009, Dec 21 2012.

[151] A. L. McPherson and G. M. Walker, "A photo-defined membrane for precisely patterned cellular and microparticle arrays," *AIP Advances,* vol. 2, p. 012153, 2012.

[152] N. E. Reist, C. Magill, and U. J. McMahan, "Agrin-like molecules at synaptic sites in normal, denervated, and damaged skeletal muscles.," *The Journal of Cell Biology,* vol. 105, pp. 2457-2469, Dec 1987.

[153] H. R. Brenner and M. Akaaboune, "Recycling of acetylcholine Receptors at ectopic postsynaptic Clusters induced by exogenous agrin in living rats," *Developmental Biology,* pp. 1-24, Aug 01 2014.

[154] R. J. Bloch and B. Geiger, "The localization of acetylcholine receptor clusters in areas of cell-substrate contact in cultures of rat myotubes.," *Cell,* vol. 21, pp. 25-35, Aug 1980.

[155] A. J. Denzer, D. M. Hauser, M. Gesemann, and M. A. Ruegg, "Synaptic differentiation: the role of agrin in the formation and maintenance of the neuromuscular junction.," *Cell and Tissue Research,* vol. 290, pp. 357-365, Nov 1997.

[156] N. Singhal and P. T. Martin, "Role of extracellular matrix proteins and their receptors in the development of the vertebrate neuromuscular junction," *Developmental Neurobiology,* vol. 71, pp. 982-1005, Oct 11 2011.

[157] S. T. Ngo, C. Balke, W. D. Phillips, and P. G. Noakes, "Neuregulin potentiates agrin-induced acetylcholine receptor clustering in myotubes.," *Neuroreport,* vol. 15, pp. 2501-2505, Nov 15 2004.

[158] J. B. Miller, "Regulation of acetylcholine receptors in the mouse muscle cell line, C2.," *Experimental Cell Research,* vol. 154, pp. 256-269, Sep 1984.

[159] J. C. Trinidad, "Neuregulin Inhibits Acetylcholine Receptor Aggregation in Myotubes," *Journal of Biological Chemistry,* vol. 279, pp. 31622-31628, Jun 08 2004.

[160] E. Bruneau and M. Akaaboune, "The Dynamics of the Rapsyn Scaffolding Protein at Individual Acetylcholine Receptor Clusters," *Journal of Biological Chemistry,* vol. 282, pp. 9932-9940, Feb 21 2007.

VITA

Jonathan (Weijia) Cheng was born in Nanjing, China in 1983. He graduated from the University of California, Berkeley with a B.S. degree in Bioengineering and the University of California, Irvine with an M.S. degree in Biomedical Engineering. He later worked as a research associate at the University of California, San Francisco under the guidance of Dr. Sharmila Majumdar and Dr. Xiaojuan Li. He pursued his Ph.D. degree in the Department of Bioengineering at the University of Washington under the guidance of Dr. Albert Folch and completed his doctoral dissertation in 2014.